An image reconstruction algorithm for a dual modality tomographic system.

NORDIN, Md. Jan.

Available from Sheffield Hallam University Research Archive (SHURA) at:

http://shura.shu.ac.uk/20268/

This document is the author deposited version. You are advised to consult the publisher's version if you wish to cite from it.

Published version

NORDIN, Md. Jan. (1995). An image reconstruction algorithm for a dual modality tomographic system. Doctoral, Sheffield Hallam University (United Kingdom)..

Copyright and re-use policy

See http://shura.shu.ac.uk/information.html

Sheffield Hallam University Research Archive
http://shura.shu.ac.uk

SHEFFIELD HALLAM UNIVERSITY LIBRARY
CITY CAMPUS POND STREET
SHEFFIELD 31 1WB

101 441 986 7

&Wo<ai-

Sheffield Hallam University

REFERENCE ONLY

ProQuest Number: 10700913

All rights reserved

INFORMATION TO ALL USERS
The quality of this reproduction is dependent upon the quality of the copy submitted.

In the unlikely event that the author did not send a complete manuscript
and there are missing pages, these will be noted. Also, if material had to be removed,
a note will indicate the deletion.

uest

ProQuest 10700913

Published by ProQuest LLC(2017). Copyright of the Dissertation is held by the Author.

All rights reserved.
This work is protected against unauthorized copying under Title 17, United States Code
Microform Edition © ProQuest LLC.

ProQuest LLC.
789 East Eisenhower Parkway
P.O. Box 1346
Ann Arbor, MI 48106- 1346

An Image Reconstruction Algorithm for a Dual Modality Tomographic System

by

Md Jan Nordin

BSc MSc

A thesis submitted to
Sheffield Hallam University
for the degree of Doctor of Philosophy
in the School of Engineering Information Technology

June 1995

Acknowledgements

I would like to record my sincere thanks to my main supervisor, Professor Bob Green, for his intelligent supervision, helpful suggestions and constructive criticisms of my work. I am extremely grateful for his outstanding support and encouragement throughout the course of this research.

I would also like to express my sincere thanks to my co-supervisors, Dr Ivan Basarab and Dr Fraser Dickin (Process Tomography Unit, UMIST) for their help and advice.

For my colleagues in Room 2302 School of Engineering Information Technology, Tony, Ruzairi, Fuad, Neil, Marshall and Joe, thank you for your valuable discussions and suggestions.

The financial assistance from the Malaysian Government and Universiti Kebangsaan Malaysia is highly appreciated without which this research could not have been possible.

Dedication

This work is dedicated to my wife Mazlinah for being very patient, understanding and for organising everything in an excellent manner for the whole family especially looking after our beloved children, Nurulhusna, Nahdiya and Mardhiyah during those difficult years.

Abstract

This thesis describes an investigation into the use of dual modality tomography to measure component concentrations within a cross-section. The benefits and limitations of using dual modality compared with single modality are investigated and discussed. A number of methods are available to provide imaging systems for process tomography applications and seven imaging techniques are reviewed. Two modalities of tomography were chosen for investigation (*i.e.* Electrical Impedance Tomography (EIT) and optical tomography) and the proposed dual modality system is presented. Image reconstruction algorithms for EIT (based on modified Newton-Raphson method), optical tomography (based on back-projection method) and with both modalities combined together to produce a single tomographic imaging system are described, enabling comparisons to be made between the individual and combined modalities.

To analyse the performance of the image reconstruction algorithms used in the EIT, optical tomography and dual modality investigations, a sequence of reconstructions using a series of phantoms is performed on a simulated vessel. Results from two distinct cases are presented, a) simulation of a vertical pipe in which the cross-section is filled with liquid or liquid and objects being imaged and b) simulation of a horizontal pipe where the conveying liquid level may vary from pipe full down to 14% of liquid. A computer simulation of an EIT imaging system based on a 16 electrode sensor array is used. The quantitative images obtained from simulated reconstruction are compared in term of percentage area with the actual cross-section of the model. It is shown from the results that useful reconstructions may be obtained with widely differing levels of liquid, despite the limitations in accuracy of the reconstructions.

The test results obtained using the phantoms with optical tomography, based on two projections each of sixteen views, show that the images produced agree closely on a quantitative basis with the physical models. The accuracy of the optical reconstructions, neglecting the effects of aliasing due to only two projections, is much higher than for the EIT reconstructions. Neglecting aliasing, the measured accuracies range from 0.1% to 0.8% for the pipe filled with water. For the sewer condition, *i.e.* the pipe not filled with water, the major phase is measured with an accuracy of 1% to 3.4%. For the single optical modality the minor components are measured with accuracies 6.6% to 19%. The test results obtained using the phantoms show that the images produced by combining both EIT and optical tomography method agree quantitatively with the physical models. The EIT eliminates most of the aliasing and the results now show that the optical part of the system provides accuracies for the minor components in the range 1% to 5%. It is concluded that the dual modality system shows a measurable increase in accuracy compared with the single modality systems. The dual modality system should be investigated further using laboratory flow rigs in order to check accuracies and determine practical limitations. Finally, suggestions for future work on improving the accuracy, speed and resolution of the dual modality imaging system is presented.

Contents

1. Introduction

This chapter introduces the idea of using tomographic imaging for monitoring individual components of multi-component flows. The aim of the project was to measure the volume flow rates of major components of sewage. Single modality tomography systems have proved effective in the monitoring of dual component flows such as liquid/gas, liquid/solid etc., but are inadequate when more components are present. Therefore, in this work two modalities of tomography were chosen for investigation (*i.e.* Electrical Impedance Tomography (EIT) and optical tomography). The work reported in this thesis concentrates on the investigation of image reconstruction for EIT, optical and with both modalities combined together to produce a single tomographic imaging system for sewers.

1.1 An overview of process tomography

The need for tomographic imaging in the process industry is analogous in many respects to the medical need for clinical diagnostic purposes (Dickin *et al.*, 1992a). The general principle underlying process tomography is to attach a number of non-intrusive sensors (transducers) in a plane or a number of planes of the vessel to be studied. Unlike medical tomography, which has been successful by the development of computer assisted tomography (CAT) (Herman, 1980), the development of tomographic instruments for process applications are still undergoing development (Isaksen, 1994). The main reason for this is the difficulty in designing an instrument which is robust and operable in aggressive and fast moving environments such as multicomponent flows which are common in process applications.

In the same way that CAT devices have revolutionised much of diagnostic medicine, process tomography aims to improve the operation and design of processes handling multicomponent flows by enabling boundaries between different components in a process to be imaged (Dickin *et al.*, 1992a) and, if necessary, in real-time (Cook and Dickin, 1993). The resultant tomographic images should therefore yield a representation of the internal structure of the process vessel in two-dimensions (Dickin *et al.*, 1992a). These images can be used for example in identification of individual components in multicomponent flows. With this form of information more readily available, process 'diagnosis' becomes more accurate and consequently more precise guidance can be given for monitoring and control purposes (Dickin *et al.*, 1992b).

Potential applications of process tomography to industrial-based equipment are limited. However, of particular interest in environmental monitoring is the investigation of volume flow rates of the major components of sewage - this being the application described in this project. The use of conventional measuring instruments, such as those based on optical techniques as a means of acquiring measurement information, is severely limited in most practical conditions since, some of the components inside the sewers exhibits a high degree of opacity. On the other hand, the use of electrical-based tomography does not suffer this limitation since it depends on the electrical properties of the multicomponent flows. However, if these techniques (*i.e.* EIT and optical measurements) combine together and form a dual modality tomographic imaging system, there is a possibility more information can be acquired than with a single modality system.

The main components of sewage are cellulose material (papers, rags, etc.), rubbers, plastics, solids and conveying liquid (mainly water based). Each has varying physical properties making them difficult to detect using a single measurement technique. For instance, if the flow is dominated by non-conducting materials (*i.e.* clear plastic and rubber) as in a sewer, this dual modality system can identify them. Clear plastic is a non-conducting material and translucent white rubber is a non-conducting material and opaque. If only EIT is used, the materials will be identified as non-conducting material without further classification.

1.2 The aims and objectives of the thesis

The main aim of the work reported in this thesis is to investigate the feasibility of applying a dual modality (resistive electrical impedance tomography and optical tomography) system to map multicomponent flow for the measurement of volume flows in sewers. This leads to a challenging image reconstruction problem, that is to combine data from both techniques to produce single dual modality tomographic images. This requires superimposing the two images obtained from the two types of sensors. The sensing principles are difficult; EIT is a soft field method, while optical sensors are line sensors and also they detect different materials (some materials may be transparent to one type of sensor). The aims can be stated in more detail as follows:

1. To study the fundamental principles of electrical impedance tomography and optical tomography and to investigate the feasibility of using them for process-based application.
2. To study the performance and limitations of existing medical-based image reconstruction methods, to implement and, if necessary, to modify and further develop these methods for use on multi-component flows.
3. To visualise multi-component flow mixtures by mapping the cross-section inside the pipe.
4. To study the reconstructed images for a range of materials within a liquid conveyor in terms of image 'quality' and range of materials detected.
5. To establish the accuracy and limitations of the dual modality system by testing it with simulated data using numerical approaches.
6. To propose suggestions for future work on the project.

1.3 Organisation of the thesis

Chapter 1 of this Thesis presents a brief introductory description on the topic of process tomography. The aims and research objectives are described, followed by a brief description of the Thesis structure.

Chapter 2 reviews the imaging techniques. A number of methods are available to provide imaging systems for process tomography applications, of which some are discussed in this chapter.

Dual modality imaging system for sewers is described in Chapter 3. This chapter introduces the idea of using tomographic imaging for the monitoring of volume flows of the various components in sewers.

The principles of image reconstruction method are introduced and reviewed in Chapter 4. This chapter consists of three major parts. In the first the image reconstruction method for an electrical impedance tomography system is described. In the second the image reconstruction method for the optical imaging system is described. The final part describes how both techniques can be combined to produce a single dual modality tomographic image.

Chapter 5 presents results from numerical simulated data for EIT. This chapter analyses the results obtained from the EIT image reconstruction method and compares them using quantitative measure.

Chapter 6 presents results from numerical simulated data for optical tomography. This chapter analyses the results obtained from the optical image reconstruction method and compares them using quantitative measure.

Chapter 7 presents results from numerical simulated data for dual modality. This chapter analyses the results obtained from combining both EIT and optical tomography system for the monitoring of concentration profiles of the various components in sewers. The results are compared and analysed using a quantitative measure.

Chapter 8 provides a discussion and conclusion and suggestions for future work. This includes extending the existing work and some new approaches.

2. Imaging Techniques

A number of methods are available to provide imaging systems for process tomography applications, of which some are discussed in this chapter.

2.1 Positron Emission Tomography (PET)

Positron emission tomography is based upon the distribution of activity of positron emitters. Radioactive carriers or emitters are injected into the process to be studied. A function of position and time in relation to the emitters is obtained from external coincidence measurements. The fundamental measurement is the coincidence detection of two almost anti-parallel photons, which are emitted as a result of the annihilation of a positron with an electron. Imaging systems involve either circular geometry, with rings of sensors around the flow to be imaged, or position sensitive detectors, such as gamma cameras or multiwire proportion chambers (Parker *et al.*, 1992).

Applications in medicine include studies of blood flow and oxygen distributions. The technique was pioneered after being used by high energy physicists in particle physics experiments, and is now being applied to areas such as the study of the mechanisms involved in mixing processes. The characteristic of this method of imaging is that it pinpoints the positions of individual particles in the medium, and not bulk masses as in X-ray tomography. Contemporary work on positron-based imaging is carried out at Birmingham University (Parker *et al.*, 1992).

2.2 X-ray

X-ray transmission computed tomography is one of the main imaging techniques used in diagnostic medicine. It was through its success at solving medical imaging problems that it was chosen to be applied in other areas such as engineering.

Two kinds of X-ray imaging are X-ray transmission radiography and X-ray transmission tomography (Simon, 1975). For X-ray transmission radiography, the image is static. It is the shadow of the object formed by a transmitted X-ray impinging on a detector such as photographic film. This is not a desirable method where flow imaging is concerned, as it provides no method of providing a continuous image of the flow.

In X-ray transmission tomography, the concern is with the provision of images of sections or thin slices through an object at different depths. This is achieved by the carefully calculated and controlled relative motion of the X-ray source and the detector during the exposure. This technique has become known as computerised tomography, (*i.e.* a CT scan). The equipment needed for this is large and bulky, and a high element of danger is involved due to the presence of ionising radiation (Simon, 1975) — so this is not the best suited tomographic tool for flow imaging in an industrial setting.

2.3 Nuclear Magnetic Resonance (NMR)

Nuclear magnetic resonance imaging is also used in medicine, and the theory behind its operation is very complex (Pykett, 1982). Many atomic nuclei exhibit the property 'spin', and as a consequence posses a magnetic moment aligned along the axis of the spin. The spin is quantised, and is characterised by the quantum number I, which may be either integer or half integer. The nuclei most commonly used in NMR are those with $I = 1/2$, e.g. hydrogen (Cady, 1990).

When a nucleus with spin is placed in a magnetic field, it will attempt to line up with the field. With a quantum number $I = 1/2$, the nucleus can take up one of two stable states - namely parallel to the field, or the opposite direction. These correspond to high and low energy states, but there will be a bias to the lower energy state, as given by Bolzmanns equation:

$$\frac{N_{down}}{N_{up}} = \exp(hf / kT)$$

Where N_{down}, N_{up} are the number of nuclei with spin up and spin down. k is Bolzmanns constant, h is Planck's constant and T is the absolute temperature.

In this aligned state, the sample will achieve a net magnetisation, which is the quantity observed in NMR, and is proportional to the applied field - so a higher applied field gives a greater sensivity. The applied magnetic field is provided by an RF magnetic field pulse generator, and the received signal is a weak, free induction signal emanating from the subject. The actual image obtained is of proton density within the subject. This is a very expensive way of imaging which would not be viable for imaging flows at present. Extensive work on Magnetic Resonance Imaging (MRI) using modified nuclear magnetic resonance (NMR) systems is being performed at Cambridge University and in the USA (Dickin *et al.*, 1992b).

2.4 Ultrasound

The primary use for ultrasound imaging is in diagnostic medicine. Its distinguishing feature is its ability to provide accurate cross-sectional views of soft tissue (Crecraft, 1983). Ultrasound waves are acoustic waves of the order of 1 to 10 MHz in frequency. Medical imaging using ultrasound waves has been well researched and documented (Wells, 1977).

The equipment in ultrasound measurements include an ultrasonic generator, a transducer to transmit and receive ultrasonic waves, and some kind of computerised image processing system. A technique known as Doppler ultrasound (Kremkau, 1990) is used to image a moving interface. An interface is the boundary region between two different objects, or types of tissue. The ultrasonic signal is strongly reflected wherever there is an interface between one tissue and another - allowing a degree of localisation and discrimination which is not possible with X-ray images. When the ultrasonic waves strike the moving interface, the frequency of the reflected waves is altered in proportion to the velocity of the moving interface. This technique can be used to visualise flow in blood vessels throughout the body (Jaffe, 1984). However, there is some danger present when using ultrasound. Ultrasound exposure of a bone/tissue interface can result in sudden and sometimes pronounced periosteal pain arising from a build-up of heat at the interface (WHO, 1982; Lehmann *et al.*, 1967).

Ultrasound is now being applied to flow imaging in pipes, and research is being undertaken to develop a tomographic system for flow imaging with ultrasound. Work on ultrasound sensing has been carried out to measure bubble velocities in two phase flow (Xu *et al.*, 1988). The ultrasonic transducer is excited using extremely short duration voltage pulses which causes a pulse of energy to propagate through the flow medium. The propagated pulses are attenuated by a magnitude dependent on the properties of the materials contained within the flow. The signal received at the detector is a train of amplitude modulated pulses which can be processed and low pass filtered to produce an analogue wave form. Investigations by Pinkard (1990) for the Water Research Council suggested that the use of ultrasonics to detect solids within sewage flows was impractical due to the lack of contrast between the attenuation properties of the conveying liquid and solid material such as faeces. In addition, it has been shown (Beyer and Letcher, 1969; Muir and Carstensen, 1980; Carstensen *et al.*, 1981) that the frequencies and intensities used in pulsed diagnostic ultrasonics can potentially create significant distortion of sound waves in water.

2.5 Capacitive impedance tomography

Electrical capacitance tomography is based on the principle that the movement of materials through the sensing volume will alter the permittivity and hence the measured capacitance of the volume. A number of electrodes are mounted circumferentially around a pipe, and the capacitance between all combinations of electrode pairs measured. The dielectric distribution within the pipe is usually reconstructed using the Linear Back Projection (LBP) method (Xie *et al.*, 1992). At present, a capacitive tomography system for imaging pipelines containing insulating mixtures (such as solids/gas and liquid/gas) is already delivering images of powder/air and kerosene/nitrogen flows (Dickin *et al.*, 1992b). It uses a charge-transfer capacitance transducer working at 15 volts with a noise level as low as 0.08 *fF* r.m.s and a 6" pipeline twelve-electrode system (Huang *et al.*, 1992; Xie *et al.*, 1992). It enables void fraction and the flow regime to be determined and is the first key stage in developing a non-invasive two-component mass flow meter.

However, according to (Isaksen and Nordtvedt, 1992) accurate quantitative information from such a system is difficult to obtain due to the following problems:

a) No simple relation between the measured capacitance and the dielectric distribution exists.

b) The electric field between the source and detector electrodes determine the sensitive region, which does not posses a sharp boundary.

c) The sensitivity for the measured quantities is not constant within the sensitivity region.

However, this system is not considered suitable for this project, because it does not work reliably when the major conveying liquid is conducting..

2.6 Electrical Impedance Tomography (EIT)

Electrical Impedance Tomography (EIT) is concerned with obtaining images of 'bodies' by non intrusive means. Electrodes are placed around the subject and signals are fed onto-into the body, the remaining electrodes are used to take voltage readings. These readings are fed into a computer which processes the information into the form of a conductivity/resistivity map. The conductivity/resistivity map is displayed on the computer screen. The map is colour coded to highlight areas of equal conductivity/resistivity. It is used, for example, in medicine to take cross sectional studies of arms, legs, breasts and the torso (Bhat, 1990). This will be discussed in more detail in Section 3.2.

2.7 Optical Tomography

Optical sensing systems have been investigated at Bolton Institute of Higher Education by (Saeed *et al.*, 1988; Dugdale *et al.*, 1992; Dugdale, 1994) for the identification of two component flows. The optical system is designed using a pair of optical transducers. The transducer pair consists of an infra-red light emitting diode (LED) and a sensing photo diode. Pulses of near infra-red light are generated by the emitter and optically configured to form a collimated beam through the fluid in the pipe. The voltage generated by the sensor is related to the amount of attenuation in the path of the beam, caused by the flow regime. The analogue signals from an array of multiplexed transducers, covering a cross-section of the pipe, are converted into digital form and passed into an image reconstruction system. Data acquired in this way can form the basis for a number of reconstruction algorithms enabling an image of the cross-section of the flow regime to be created. The main constituents of sewage have variable abilities to absorb/transmit light (infra-red) (Pinkard, 1990). This enables an optical system based on attenuation of infra-red transmission to be used.

2.8 Discussion

From the outline on the methods described above it was decided to investigate a dual modality system based upon Electrical Impedance Tomography and Optical Transmission Tomography. The hardware for the proposed system is described in the next chapter.

3. Dual Modality Imaging System (DMIS) for Sewers

In this chapter an outline of the proposed dual modality system is presented. The chapter consists of three sections. The first and second sections deal with the EIT imaging system and the optical imaging system respectively. The last section is a description of how both technologies are combined to investigate dual modality tomography.

3.1 Introduction

Electrical Impedance Tomography (EIT) is a method for revealing the internal structure of a conducting object or a living body without destruction by reconstructing an image that represents the space distributed property of the materials it contains. The main application of image reconstruction is in medicine, with computerised tomography, which allows one to analyse the structure of human organs, detect tumours, and aid medical diagnosis (Jossinet *et al.*, 1988; Eyuboglu and Brown, 1988; McArdle *et al.*, 1988). Applications of EIT in the process industry are new although these applications are growing very quickly as industry appreciates their use (Xie *et al.*, 1994; McKee *et al.*, 1994).

Image reconstruction can help to visualise multi-phase flow distributions and the distribution of the components in a variety of systems, for example, oil pipelines and sewers. This flow information is not only important under steady operation but also under transient and fault conditions.

The main constituents of sewage have variable resistivities, densities and abilities to absorb/transmit light (infra-red) (Pinkard, 1990). Because of the different characteristics of the main constituents of sewage, a combination of two or more detection methods will need to be used. For this project, based on a literature search on the most applicable work, data from two detection methods is investigated. This results in dual modality tomographic imaging, which in this case is based upon electrical impedance tomography (Webster, 1990; Gisser *et al.*, 1987; Samakato *et al.*, 1987; Yorkey, 1986 and Abdullah, 1993) and infra-red matrix imaging (Saeed *et al.*, 1988; Dugdale *et al.*, 1992 and Dugdale, 1994).

The three major solid components of sewage to be detected are rubber, effluent solids and cellulose products. Rubber should be detectable by impedance methods while solids should be visible to an infra-red matrix system. The main problem comes with any cellulose products where a low resistivity is expected, due to the absorption of fluids, and its translucency under these conditions is unknown.

3.2 Electrical Impedance Tomography System

The objective of electrical impedance tomography is to produce an image which correctly represents the impedance characteristics of a region of interest. In doing so it is important to have some idea of the system's ability .to provide a quantitative representation of those impedance characteristics.

The strategy used in the present work for measuring the voltages at the periphery of the pipe is called the neighbouring method. A pair of adjacent electrodes is selected and a current is applied between them. The potential gradients established between the rest of the pairs of adjacent electrodes are measured. This sequence is repeated until all the adjacent pairs have been selected for current injection and the corresponding boundary voltage gradients have been measured. For a system with N electrodes, using the 4 electrode measurement method, a total of $N\times(N\text{-}3)/2$ independent measurements are made. Applying this technique in a system with 16 electrodes gives a total of 104 independent measurements.

The finished system should be able, to distinguish a solid from a liquid from a gas, as sewerage pipe flows will almost always contain multicomponent flows. The images to be produced do not have to be as high in resolution as normally needed for medical imaging, only the order of the size and distribution of each component of the flow, in a cross-section, are required.

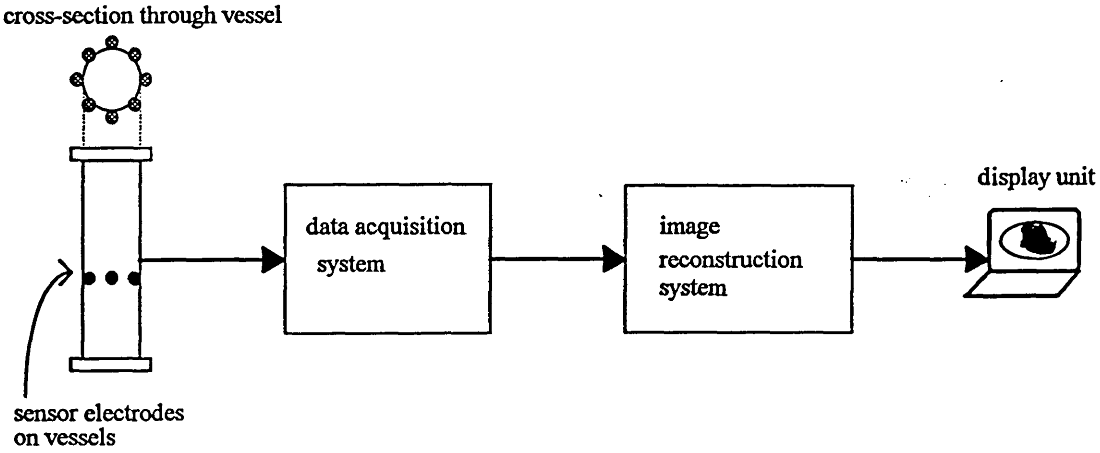

Figure 3.1 A typical EIT system

A typical EIT system is shown in Figure 3.1. It consists of three subsystems described in the following subsections:

a) sensor subsystem

b) data acquisition system (DAS)

c) image reconstruction and display

3.2.1 Sensor subsystem

As with all measurement systems the sensors are one of the most critical parts of the system which have a profound effect on the accuracy and reliability of the complete system. Errors in voltage measurements on the electrodes are translated into large errors in the calculated resistivity distribution. Practical considerations place a number of constraints on the sensors. Ideally it should be compact, non-intrusive, require minimum maintenance or calibration, and in many cases be intrinsically safe. The electrodes are usually mounted on the surface around the object. The number of electrodes used depends on the complexity and resolution of the images required. The number of electrodes used at present is typically 16, 32 or 64.

3.2.2 Data acquisition system (DAS)

Due to the constraints imposed by the strict safety requirements of clinical instruments the majority of biomedical DAS's are restricted in the range of measurements they can make. DAS for the process industry do not have this restriction (except in safety critical situations) and can therefore have a much wider dynamic measurement range. Currents injected into the object are provided by voltage controlled current generators. Many current injection methods have been proposed by EIT investigators (Webster, 1990) such as: adjacent, opposite, multireference, multisink and optimal. The injection method has a significant effect on the quality of the images produced (Webster, 1990). For accurate voltage measurements the injected currents amplitude must be maintained constant throughout the measurement period. This requires current and voltage generators with very good stability and low harmonic distortion (Wang *et al.*, 1992).

The overall accuracy of the system is governed by the resolution of the analogue to digital converter (ADC). For EIT, this requires at least a 12-bit ADC (resolution approximately 0.025%). The signal input to the ADC is conditioned by the programmable gain amplifier (PGA), phase sensitive demodulator and low pass filter. These circuits ensure that the signal input into the ADC is optimised in amplitude, phase and signal to noise ratio. A typical components of EIT data acquisition system is shown in Figure 3.2. A detailed description on designing an accurate EIT DAS is documented in (Wang *et al.*, 1992).

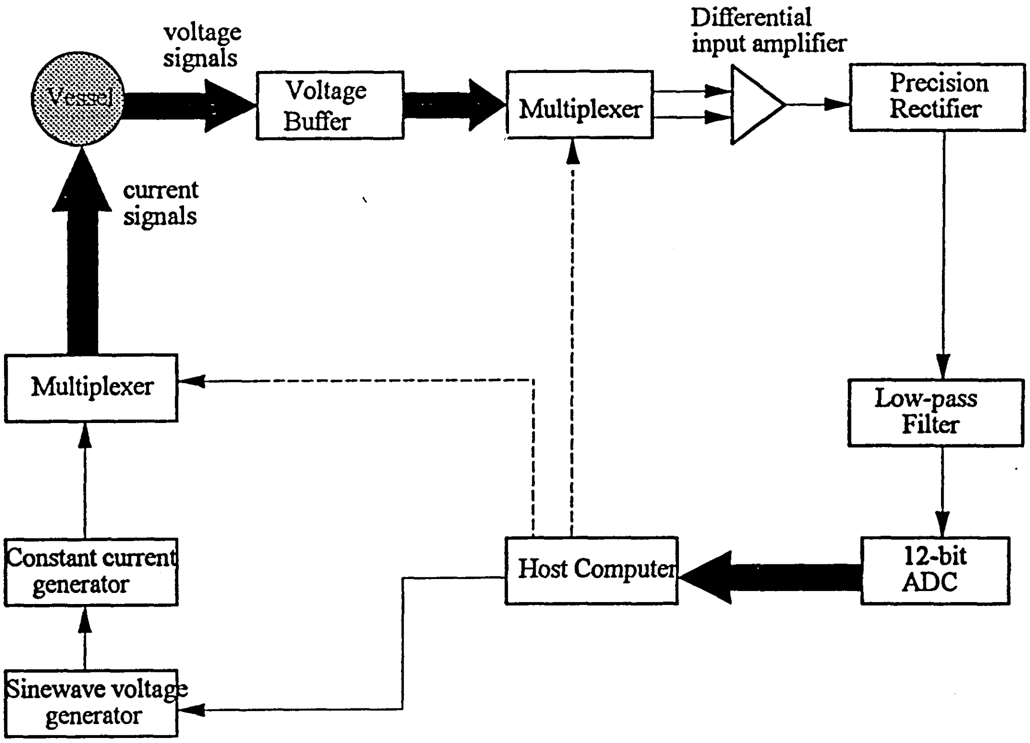

Figure 3.2 Components of typical EIT data acquisition system

3.2.3 Image reconstruction and display

Voltages measured by the data acquisition system (DAS) are passed to the image reconstruction algorithm. This algorithm uses the voltages taken from a number of independent measurements to map the resistivity distribution of the object's cross-section. For N electrodes (for the four-electrode measurement method) there are N(N-3)/2 independent measurements (Seagar, *et al.*, 1987).

The image reconstruction algorithm can be separated into two distinct stages, known in EIT as the 'forward problem' and the 'inverse problem'. The forward problem determines the boundary and internal voltage distribution within an object given the resistivity distribution and current boundary conditions. It is followed by the inverse problem which determines the resistivity distribution given only the boundary current conditions. In essence, a reconstruction algorithm first makes an initial guess of the resistivity distribution. It then uses the forward problem solver to calculate the boundary voltages. These voltages are compared with the DAS measured voltages. Errors formed by the calculated and measured voltages are used to update the resistivity distribution. This process is repeated until the error between the forward problem solver and the measured values reach a predefined level. Generally, the inverse problem requires the solution of the forward problem.

From the point of view of the reconstruction of resistivity distribution images and neglecting problems associated with data collection accuracy is dependent on several factors including:

a) accuracy of the forward problem solver
b) accuracy of DAS
c) effectiveness of the reconstruction algorithm

A special problem that the image reconstruction must take into consideration for this project is the depth of the conveying liquid, which will vary. All existing tomographic imaging systems have *a priori* knowledge of the process boundary.

Different algorithms for reconstruction have been proposed by many researchers. Each method has its merits and limitations. Yorkey *et al.*, (1990) provides a good reference on the effectiveness of various reconstruction algorithms used in EIT. The main methods currently being used are:

- fast filtered back projection method (Barber and Seagar, 1987) and (Seagar *et al*, 1987).
- iterative equipotential lines method (Yorkey *et al*, 1987).
- perturbation method (Kim *et al*, 1987) and (Yorkey *et al*, 1987).
- double constraint method (Wexler *et al*, 1985)
- modified Newton-Raphson method (Yorkey *et al*, 1987).

3.3 Optical Imaging System

Optical Tomography involves projecting a pencil of light through some medium from one boundary point and detecting the level of light received at another boundary point. This single pencil of light is called a view. The principle is straight forward, as light travels through space it suffers attenuation for a variety of reasons, such as scattering and absorption. Different materials cause different levels of optical attenuation and this fact forms the basis of optical tomography. Several pencils of light are used in parallel to produce one projection. This procedure provides information from which a profile of the flow can be gained. In practise several projections are required to minimise aliasing which occurs when two particles intercept the same view. This process is described by Saeed *et al.*, 1988, where two component flows are monitored.

The schematic diagram of an optical tomography system is shown in Figure 3.3. The system uses bright LEDs type (Siemans SFH484-2) as the light sources because of their low cost, small half angle and a peak wavelength which may be matched to a standard photo-diode detector. The optical receivers are photo-diodes which produce a current signal related to incident light intensity. This current is converted to a voltage, amplified, conditioned and converted to an eight bit digital voltage using a MAX155 data acquisition circuit. Each MAX155 interfaces eight channels and these voltages are fed into the computer. A transmitter and detector pair is enabled using multiplexers under the control of the host PC. The I/O board is positioned in a spare expansion slot of an IBM compatible personal computer and mapped into two vacant memory locations allowing access by the system software.

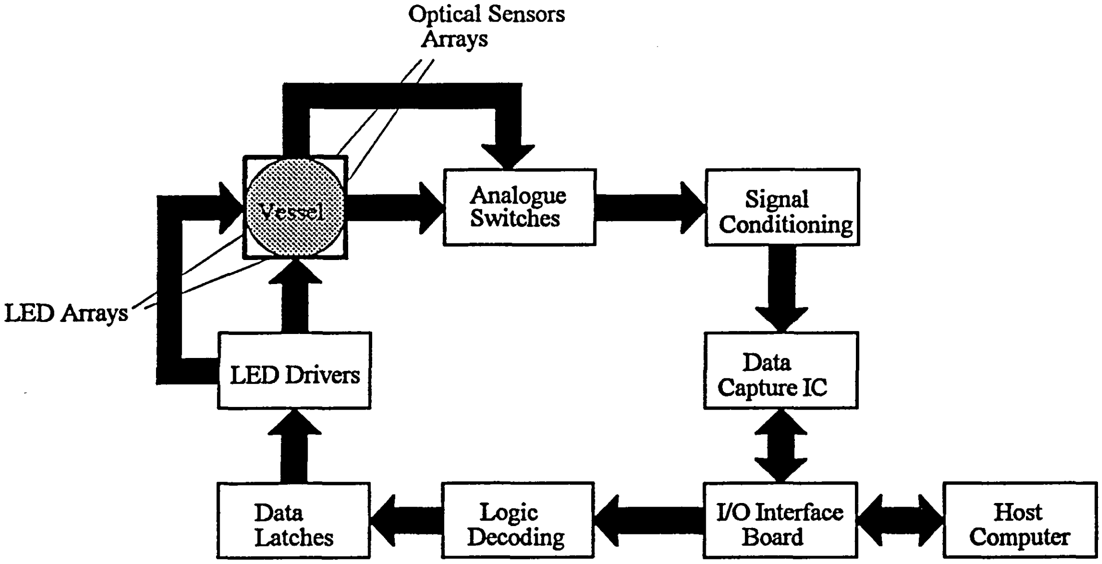

Figure 3.3 Schematic diagram of an optical tomography system

3.4 The Data Collection System

The basic system shown in Figure 3.4 below uses two different arrays of transducers. The transducers, one optical the other EIT, are being investigated to determine if they are capable of identifying the main constituents of the sewers. Both EIT and optical sensors are mounted on the same section of the pipe. The EIT system uses 16 electrodes and is capable of injecting a constant current via any two electrodes and measuring the resultant voltage differentials produced at any other two electrodes. The optical hardware is designed around two projections of 16 transducer pairs as this allows basic image reconstruction to be applied to the acquired data.

Both sets of transducers have to be positioned close together to reduce the possibility of an offset when both sets of data are combined in the final stage of image reconstruction. Initial results for this system can be found in Daniels *et. al.*, 1993a and Daniels, *et. al.*, 1993b.

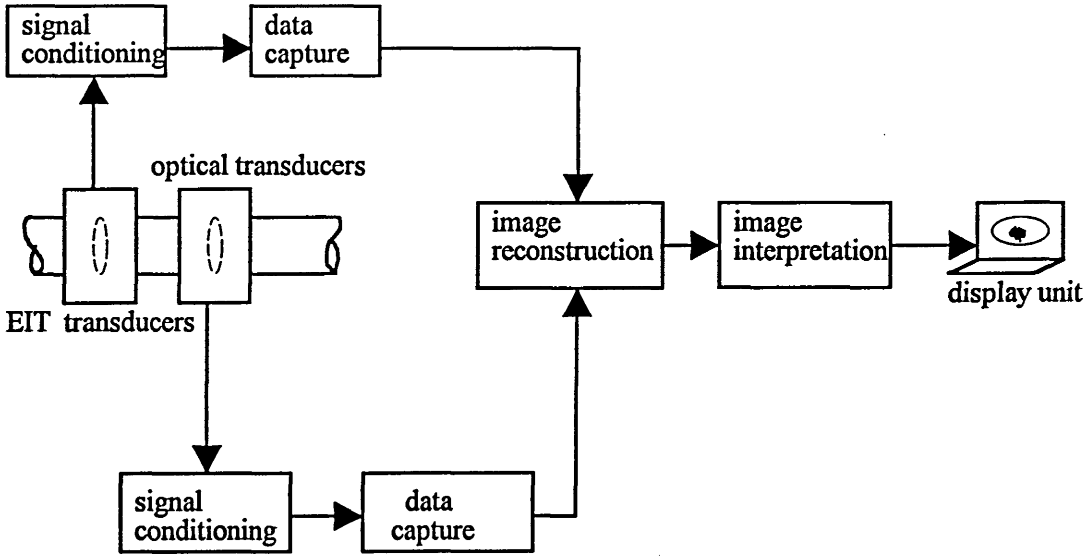

Figure 3.4 The proposed dual modality imaging system for sewers

The software implementation of this dual modality imaging system uses a 32x32 array to store the values of both EIT and optical measurements for each pixel location as shown in Figure 3.5. Reconstruction of EIT images (resistivity values) are mapped onto a 32 x 32 array as colour values. Similarly, optical images (light intensity) are also stored onto a 32 x 32 array as pattern values. Both techniques display an image based on 32 x 32 array and consequently this is the maximum resolution with this system. The 104 triangular areas shown in Figure 4.2 need to be mapped onto a rectangular array of pixels and this has to be done with care to allow both to be superimposed for the final dual modality reconstruction.

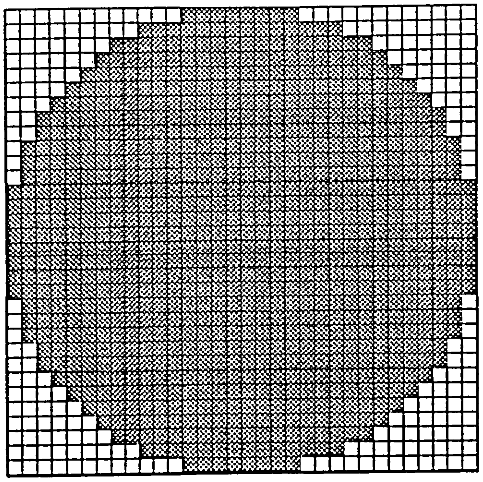

Figure 3.5   32 x 32 array used in dual modality software implementation

4. Image Reconstruction Method

In this chapter theory relating to the reconstruction of tomographic images is presented. The chapter is divided into three sections. The first and second sections deal with image reconstruction methods for EIT systems and image reconstruction methods for optical imaging systems respectively. The final section is a description of how tomographic images from both techniques can be manipulated to produce single tomographic images of volume concentrations of multicomponents in a test section.

4.1 Image reconstruction method for EIT system

The task of image reconstruction in electrical impedance tomography can be divided into two distinct parts (Section 3.2.3):
(a) the forward problem
(b) the inverse problem.

4.1.1 The forward problem

A voltage distribution is developed on the surface of an object when a current distribution is applied to the body of the object. The relationship between these voltage and current distributions is controlled by the distribution of conductivity/resistivity within the region and the shape of the surface. The forward problem involves the determination of the voltage distribution within the object and on the surface of the object given the conductivity/resistivity distribution within the object and a known current flows through the object. This is the initial stage in the image reconstruction process for EIT system.

For a simple two-dimensional model such as the cross-section of a circular process vessel, the solution to the forward problem can be analysed using an analytical solver even though numerical techniques such as the finite element method (FEM) are preferred (Webster, 1990). The preference for the latter is due, in part, to the fact that the FEM is more flexible in handling problems involving a vessel with a complicated geometrical shape and accommodating inhomogeneous material distributions within it. The conductivity/resistivity distribution within the region is partitioned into discrete elements each with assumed constant conductivity/resistivity. By exploiting continuity of voltage and current flow at the boundaries of the elements the problem is reduced to the solution of a generally large series of linear equations. Murai and Kagawa (1985) model the finite element method as a discrete resistance network, equivalent to assuming that within an element the voltage is a linear function of position. Dines and Lytle (1981) also use a simulated resistance network, though not one equivalent to a finite element model, and solved the forward problem by a systematic application of the Kirchhoff currents laws to the nodes of the network.

4.1.1.1 Mathematical preliminaries

The theoretical problem of reconstructing an electrical conductivity distribution from a set of measured boundary voltages as a result of applying current on the boundary is governed by a number of physical laws of electromagnetism. In essence, passing a current between a pair of electrodes attached to the conductive media generates a corresponding potential distribution within it which is mathematically expressible in the form of a partial differential equation. For simplicity, it is assumed that the media is isotropic with no free charge and that reactance effects can be neglected. The validity of these assumptions were investigated by Brown *et al*, (1983). Under such conditions, the equation relating the distribution of electric potential inside the object through which a steady state alternating current is flowing can be derived from a combination of Maxwell's electrostatic equations given by

$$\nabla \bullet (\sigma \nabla \phi) = 0 \qquad \text{in } \Gamma \tag{4.1}$$

where σ is the conductivity of the medium and ϕ is the electrical flux. The object, which in this case is a process vessel, is represented by the symbol Γ and Π is given to represent its boundary. Also, collectively referred to as the Laplace equation, the differential vector operator ∇ in equation (4.1) specifies the space differentiation with reference, in this situation, to three-dimensional Cartesian co-ordinates (x,y,z):

$$\nabla = \left\{ \frac{\delta}{\delta x}, \frac{\delta}{\delta y}, \frac{\delta}{\delta z} \right\} \tag{4.2}$$

Like any other boundary value problem, the partial differential equation shown in equation (4.1) can subsequently be solved by applying the appropriate boundary conditions. In EIT, alternating current is applied through one pair of electrodes and the resulting voltages measured through a different pair of electrodes attached to the object's boundary (this is referred to as the adjacent measurement technique). Hence, the equivalent boundary conditions associated with applying currents are of the Neumann type given by:

$$\sigma \frac{\partial \phi}{\partial \nu}\bigg|_{\Pi} + j = 0 \tag{4.3}$$

on the negative driving electrode and ,

$$\sigma \frac{\partial \phi}{\partial \nu}\bigg|_{\Pi} - j = 0 \tag{4.4}$$

on the positive driving electrode, where ν is the outward unit normal and j is the applied current density. The resulting voltage on the boundary is given by:

$$\phi|_{\Pi} = v \tag{4.5}$$

In practice the voltages are not completely determined until a reference condition is specified. One convenient way of achieving this is:

$$\sum_{i=1}^{N} v_i = 0 \tag{4.6}$$

In this manner, equation (4.1) together with the conditions in equations (4.3), (4.4) and (4.6) can be solved to yield a unique set of solutions (Cheney and Isaacson, 1991). Hence the forward problem can be diagramatically stated as:

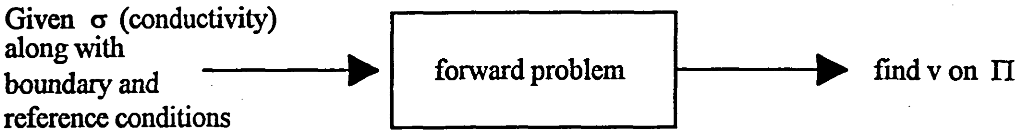

Figure 4.1 The forward problem in EIT

In the following sub-sections, mathematical procedures based on the finite element method are outlined for general two and three-dimensional cases even though, for simplicity, a two-dimensional case was implemented and used throughout this study.

4.1.1.2 Finite element modelling (FEM) of a typical process vessel

Modelling the electromagnetic field resulting from the passage of electric current inside the process vessel is a mathematical procedure involved with determining the solution to Maxwell's equation given in equation (4.1). One such solution can be obtained by a direct integration method provided that the medium is in a completely homogeneous state. However, in many cases the process medium exhibits complex impedance inhomogeneity and under this condition direct integration is not possible. Instead, a piece-wise approximation can be employed which is based on the finite element method. This forms part of the motivation for using the FEM throughout this research for modelling and theoretical studies.

Application of the FEM to the solution of a physical problem is based on the minimisation of energy. Employing variational calculus, the solution to equation (4.1) and its associated boundary conditions is identical to finding a function ϕ which minimises the functional χ:

$$\chi = \frac{1}{2}\iiint_{\Gamma} \left\{ \sigma\left(\frac{\partial\phi}{\partial x}\right)^2 + \sigma\left(\frac{\partial\phi}{\partial y}\right)^2 + \sigma\left(\frac{\partial\phi}{\partial z}\right)^2 \right\} dxdydz + \iiint_{\Pi} j\phi dxdydz \qquad (4.8)$$

From equation (4.8) integration is carried out over the whole domain Γ and ϕ must be a continuous function possessing the piece-wise continuous first derivatives of the domain Γ (Zienkiewicz and Cheung, 1965). In order to implement equation (4.8) the domain is divided into *m* individual finite elements forming a mesh. For a cylindrical shaped domain the most popular (and most straightforward to implement) types of elements considered are triangular and quadrilateral shaped elements. The former is used to discretize the whole domain in this project. An example of the FEM mesh used in this study is shown in Figure 4.2

The FEM solution of a typical process model mentioned in the above paragraph requires several approximations, each of which are highlighted in the following discussion. The first approximation requires that the solution ϕ be described in a functional form, element by element. Secondly, for a given element such as the triangular element considered in this section, the spatial variation of $\phi^{(e)}$ is assumed to be linear. Thus, if the field variables $\phi_1, \phi_2, \cdots, \phi_s$ within each element are represented by functional $\Lambda_1(x,y,z)\,\phi_1$, $\Lambda_2(x,y,z)\,\phi_2, \cdots, \Lambda_s(x,y,z)\,\phi_s$ respectively, then $\phi^{(e)}$ can be treated as a linear combination of the above functions *i.e.*

$$\phi^{(e)}(x,y,z) = \Lambda_1(x,y,z)\,\phi_1 + \Lambda_2(x,y,z)\,\phi_2 + \cdots + \Lambda_s(x,y,z)\,\phi_s \tag{4.9}$$

or,

$$\phi^{e} = \sum_{k=1}^{s} \Lambda_k(x,y,z)\,\phi_k \tag{4.10}$$

In this case the field variables ϕ_k represent the model potential of each element and s its node number. Equation (4.10) can be written in matrix form to yield:

$$\phi^{e} = [\Lambda]\{\phi\} \tag{4.11}$$

The piece-wise continuous functions Λ are called the shape functions and these functions are not applied globally to the entire region being analysed but rather to many small regions or elements (Stasa, 1985). By substituting equation (4.11) into (4.8), the discretized functional $\chi^{(e)}$ can be obtained for one element. Thus, minimising the functional defined by equation (4.8) is equivalent to:

$$\frac{\partial \chi^{(e)}}{\partial \phi_i} = \begin{Bmatrix} \dfrac{\partial \chi^{(e)}}{\partial \phi_1} \\ \dfrac{\partial \chi^{(e)}}{\partial \phi_2} \\ \vdots \\ \dfrac{\partial \chi^{(e)}}{\partial \phi_s} \end{Bmatrix} = 0 \tag{4.12}$$

From equation (4.12) for the i^{th} node:

$$\begin{aligned}\frac{\partial \chi^{(e)}}{\partial \phi_i} = \iiint_{\Gamma} \left\{ \sigma \frac{\partial \phi}{\partial x} \frac{\partial}{\partial \phi_i}\left(\frac{\partial \phi}{\partial x}\right) + \sigma \frac{\partial \phi}{\partial y} \frac{\partial}{\partial \phi_i}\left(\frac{\partial \phi}{\partial y}\right) + \sigma \frac{\partial \phi}{\partial z} \frac{\partial}{\partial \phi_i}\left(\frac{\partial \phi}{\partial z}\right) \right\} dxdydz \\ + \iiint_{\Pi} j \frac{\partial \phi}{\partial \phi_i} dxdydz \quad = \quad 0\end{aligned} \tag{4.13}$$

Substituting equation (4.11) into equation (4.13) gives:

$$\begin{aligned}\frac{\partial \chi^{(e)}}{\partial \phi_i} = \iiint_{\Gamma} \sigma \left[\frac{\partial \Lambda_1}{\partial x}, \frac{\partial \Lambda_2}{\partial x}, \ldots, \frac{\partial \Lambda_s}{\partial x} \right] \left\{ \phi^{(e)} \right\} \left(\frac{\partial \Lambda_i}{\partial x} \right) dxdydz \\ + \iiint_{\Gamma} \sigma \left[\frac{\partial \Lambda_1}{\partial y}, \frac{\partial \Lambda_2}{\partial y}, \ldots, \frac{\partial \Lambda_s}{\partial y} \right] \left\{ \phi^{(e)} \right\} \left(\frac{\partial \Lambda_i}{\partial y} \right) dxdydz \\ + \iiint_{\Gamma} \sigma \left[\frac{\partial \Lambda_1}{\partial z}, \frac{\partial \Lambda_2}{\partial z}, \ldots, \frac{\partial \Lambda_s}{\partial z} \right] \left\{ \phi^{(e)} \right\} \left(\frac{\partial \Lambda_i}{\partial z} \right) dxdydz \\ + \iiint_{\Pi} j(\Lambda_i) dxdydz \quad = \quad 0\end{aligned} \tag{4.14}$$

For the entire element, equation (4.13) can be written in matrix form:

$$Y\phi = c \tag{4.15}$$

where Y is a square matrix whose coefficients are determined from the geometrical co-ordinates of element vertices and from the element conductivities; ϕ is the column vector corresponding to the number of unknown values and, in this case, the nodal potential; c represents the boundary currents, and,

$$y_{ij} = \iiint\limits_{\Gamma} \left\{ \sigma \frac{\partial \Lambda_i}{\partial x} \frac{\partial \Lambda_j}{\partial x} + \sigma \frac{\partial \Lambda_i}{\partial y} \frac{\partial \Lambda_j}{\partial y} + \sigma \frac{\partial \Lambda_i}{\partial z} \frac{\partial \Lambda_j}{\partial z} \right\} dxdydz \tag{4.16}$$

$$c_i = \; - \iiint\limits_{\Pi} j \, \Lambda_i \, dxdydz \tag{4.17}$$

Assuming that the interpolation functions Λ_i for modelling the behaviour of ϕ satisfy the compatibility and completeness requirements, the final equation for minimising the functional χ can be derived by assembling and summing the contributions to a typical differential *i. e.*

$$\chi = \sum_{e=1}^{m} \chi^{(e)} \phi^{(e)} \tag{4.18}$$

where *m* is the total number of elements chosen in the domain, and the superscript *(e)* denotes an element. Furthermore, for a particular node *i*, only the values of ϕ at those nodes connected to it will appear and their coefficients will involve only the contributions from elements adjacent to the this node. This arrangement produces a typical 'narrow-band' set of simultaneous equations (Abdullah *et al.*, 1992) which can be written same as equation (4.15), where Y is a square matrix whose coefficients are determined from the geometrical co-ordinates of element vertices and from the element conductivities; ϕ is the column vector corresponding to the number of unknown values and, in this case, the nodal potential; *c* represents the boundary currents. Hence, the general field problem given in equation (4.1) has been transformed into a set of algebraic equations which can be solved by a variety of techniques such as the Cholesky factorisation method described in more detail latter.

In this study, only a two-dimensional FEM solution is implemented even though its extension to three-dimensional problems would be relatively straightforward (see Suggestion for future work, Section 8.3). Hence, the representative field equation in the two-dimensional case can be simplified to give:

$$\frac{\partial}{\partial x}\left(\sigma\frac{\partial\phi}{\partial x}\right)+\frac{\partial}{\partial y}\left(\sigma\frac{\partial\phi}{\partial y}\right)=0 \tag{4.19}$$

The equivalent function to be minimised reduces to:

$$\chi=\frac{1}{2}\iint\limits_{\Gamma}\left\{\sigma\left(\frac{\partial\phi}{\partial x}\right)^{2}+\sigma\left(\frac{\partial\phi}{\partial y}\right)^{2}\right\}dxdy+\iint\limits_{\Gamma}j\phi dxdy \tag{4.20}$$

The design of the mesh texture to implement equation (4.1) warrants further explanation. It is often desirable to predict nodal potentials to the highest possible precision. This can be achieved using the smallest size elements possible particularly in the most sensitive part of the vessel. In EIT, the most sensitive part is the region in vicinity of the vessel's boundary. Hence, it is worthwhile placing as many finite elements as possible at the vessel's boundary region. However, the total number of elements forming the mesh is limited by the number of independent measurements available from the data collection system. For instance, if the number of elements is larger than the total number of independent measurements, the inverse problem will be under-determined. This effect is quite undesirable in many quantitative reconstruction algorithms such as the MNR algorithm since, for the under-determined system, there are more unknowns than equations and consequently, there is either no solution or an infinite number of solutions (Yorkey, 1986). Thus, to implement the MNR the chosen number of elements in the mesh must satisfy the condition specified below (Yorkey, 1986):

$$\text{Number of elements in the mesh} \leq M=\frac{N(N-1)}{2} \tag{4.21}$$

where N is the number of electrodes. However, at present, the adjacent measurement method is employed which further reduces M and hence the number of elements in the mesh to (Yorkey, 1986):

$$\text{Number of elements in the mesh} \leq M = \frac{N(N-3)}{2} \tag{4.22}$$

For a 16-electrode system *i.e.* $N = 16$, the number of independent measurements is 104. Thus, to ensure that the reconstruction problem is always determined (*i.e.* the number of unknowns must at least be equal to the number of equations), the number of elements chosen was exactly 104. The arrangement of the 104 elements inside the mesh is shown in Figure 4.2, where there are 69 nodes which are numbered.

In this study, the mesh as shown in Figure 4.2 is chosen because of the nature of flow is horizontal pipe lines where the level of flowing liquid inside the pipe may vary in depth as shown in Figure 4.3. This changing boundary condition must be considered in the modelling. This is achieved by using the mesh shown in Figure 4.2 which has a series of horizontal boundaries rather than the usual mesh which is symmetrical about the central axis.

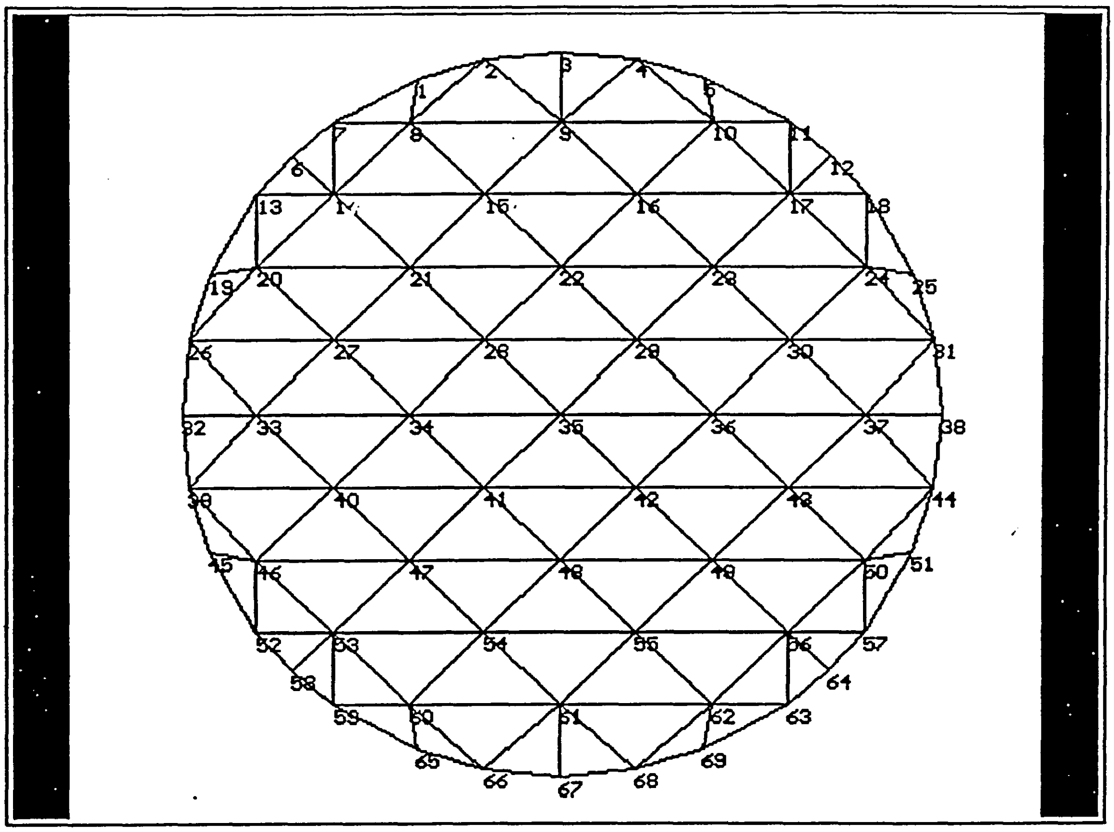

Figure 4.2 The finite element mesh

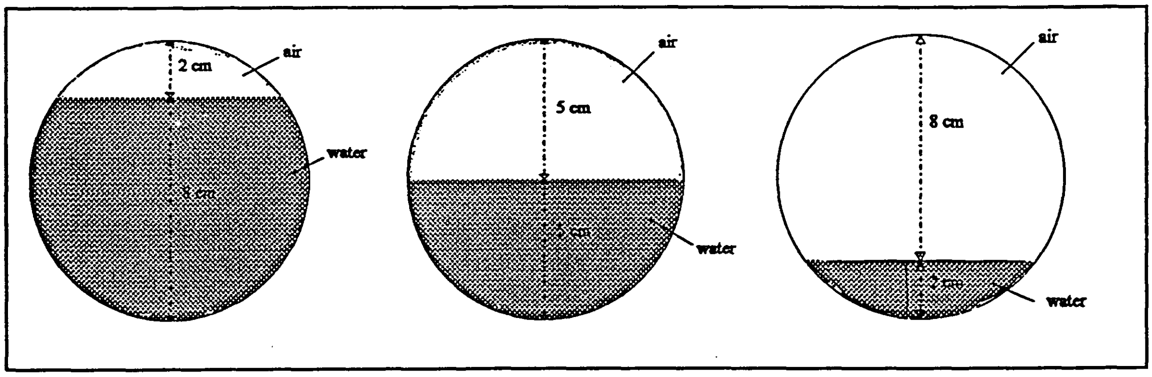

Figure 4.3 The changing depth of flow

It can also be seen from Figure 4.2 that the size of elements used in the mesh are relatively large. As a result, an accurate approximation (*i.e.* less than 1% error) of the field distribution inside the domain is difficult to attain. For example, as mentioned in the above paragraph, there is a steep gradient in the field intensity from the regions near the vessel boundary to its central axis. Thus, a finer mesh structure is desirable in these regions to accommodate the above phenomena. However, this configuration is only practical provided there are a sufficiently large number of independent measurements, *i.e.* $N = 32$ or more. Clearly for a 16-electrode system, the design of the finite element mesh is limited as evidenced in Figure 4.2 which leads to image reconstruction problems. These problems are due to extreme ill-conditioning of the Hessian matrix (Yorkey, 1986) which consequently requires the use of a regularisation technique to force the MNR algorithm to converge towards a solution.

4.1.1.3 Formulation of the forward problem.

Consider the region in which the problem to be solved is divided into triangular elements (one of them is shown in Figure 4.4 below). Also, let the triangle be defined by nodes 1, 2 and 3 and their respective local co-ordinates (x_1, y_1), (x_2, y_2) and (x_3, y_3) respectively.

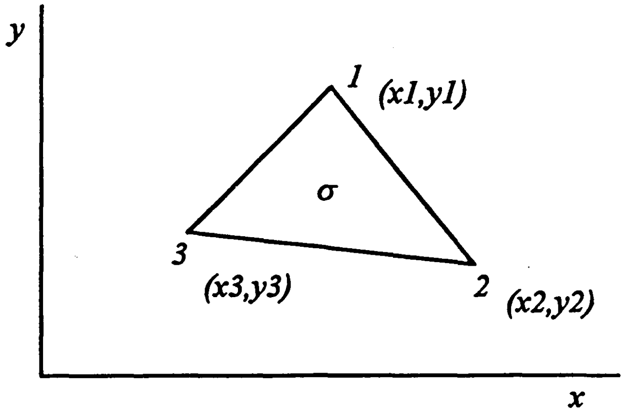

Figure 4.4 Two-dimensional representation of the triangular element

The set of function ϕ, constrained to be a set of first order polynomials for each triangle whose value at any point within the triangle, is a linear interpolation of the vertex values such that:

$$\phi^{(e)} = \alpha_1 + \alpha_2 x + \alpha_3 y \tag{4.23}$$

For all three nodal conditions this leads to a system of equations:

$$\begin{aligned}
\phi_1^{(e)} &= \alpha_1 + \alpha_2 x_1 + \alpha_3 y_1 \\
\phi_2^{(e)} &= \alpha_1 + \alpha_2 x_2 + \alpha_3 y_2 \\
\phi_3^{(e)} &= \alpha_1 + \alpha_2 x_3 + \alpha_3 y_3
\end{aligned} \tag{4.24}$$

Solving for α_1, α_2 and α_3 from equation (4.24) and substituting these values into equation (4.23) gives:

$$\phi^{(e)} = [\Lambda_1, \Lambda_2, \Lambda_3]\{\phi\} \tag{4.25}$$

where,

$$\Lambda_n = \frac{1}{2A^{(e)}}(a_n + b_n x + c_n y) \qquad n = 1, 2, 3 \tag{4.26}$$

also,

$$\begin{aligned}
A^{(e)} &= \text{area of triangle 1, 2, 3} \\
a_1 &= x_2 y_3 - x_3 y_2 \\
b_1 &= y_2 - y_3 \\
c_1 &= x_3 - x_2
\end{aligned} \tag{4.27}$$

the other coefficients $(a_2, a_3, b_2, b_3, c_2, c_3)$ can be obtained through a cyclic permutation of the subscripts 1, 2 and 3. Furthermore, it can also be seen that:

$$\frac{\partial \Lambda_n}{\partial x} = \frac{1}{2\Delta} b_n \qquad n = 1, 2, 3$$
$$\frac{\partial \Lambda_n}{\partial y} = \frac{1}{2\Delta} c_n \qquad n = 1, 2, 3 \tag{4.28}$$

Substituting equation (4.28) into equation (4.16) gives:

$$Y_{ij} = \frac{\sigma}{4A^{(e)2}} \iint_{\Gamma} \left(b_i b_j + c_i c_j\right) dxdy \qquad \text{for } i, j = 1, 2, 3 \tag{4.29}$$

Noting that:

$$\iint_{\Gamma} dxdy = A^{(e)} \tag{4.30}$$

Equation (4.29) becomes:

$$y_{ij} = \frac{\sigma}{4A^{(e)}} \left(b_i b_j + c_i c_j\right) \qquad \text{for } i, j = 1, 2, 3 \tag{4.31}$$

For the whole element, **Y** can be written in matrix form:

$$Y = \begin{bmatrix} b_1^2 + c_1^2 & b_2 b_1 + c_2 c_1 & b_3 b_1 + c_3 c_1 \\ b_2 b_1 + c_2 c_1 & b_2^2 + c_2^2 & b_3 b_2 + c_3 c_2 \\ b_3 b_1 + c_3 c_1 & b_3 b_2 + c_3 c_2 & b_3^2 + c_3^2 \end{bmatrix} \tag{4.32}$$

Since the region has been divided into p triangular elements, the complete representation of the field variable ϕ over the whole domain is given by:

$$\phi(x,y) = \sum_{n=1}^{p} \phi^n(x,y) = \sum_{n=1}^{p} [\Lambda]^n \{\phi\}^n \tag{4.33}$$

Finally, the assembly of element equations to obtain the system equations for all the domain follows the standard method given by (Huebner, 1975) can be written the same as equation (4.15), where *Y* is a $n \times n$ sized matrix having units of conductance (units: Siemen), ϕ is a $n \times 1$ sized vector which represents the voltage vector at n discrete points inside and on the boundary of the mesh, *c* is also is a $n \times 1$ sized vector which has units of amperes and contains the applied currents at n points on the boundary.

In order to solve uniquely equation (4.15), a reference condition is specified by grounding the central node inside the mesh shown in Figure 4.2. This is done by setting all entries in the i^{th} column and row corresponding to the reference node to zero and setting its diagonal element to unity. Matrix *Y*, historically referred to as the stiffness matrix, has several properties. First, it is symmetrical and very sparse. Second, matrix *Y* is a positive definite matrix. Third, *Y* is also double centred, *i.e.* the sum total of the elements in any given column or row is zero. These properties of *Y* resemble those of a classical admittance matrix (Mitra, 1969).

4.1.1.4 Classical method of solving Yϕ = c

Since *Y* is a symmetric positive definite matrix it has a unique Cholesky factorisation given by:

$$Y = LL^T \tag{4.34}$$

where ***L*** is a real non-singular lower triangular matrix with positive diagonal elements. The Cholesky factorisation algorithm used to compute l_{ij} is given by:

$$l_{ii} = \sqrt{\left(y_{ii} - \sum_{k=1}^{k-1} l_{ik}^2\right)} \qquad \text{for } i = 1, 2, \ldots, n \tag{4.35}$$

and,

$$l_{ij} = \frac{1}{l_{jj}}\left(y_{ij} - \sum_{k=1}^{j-1} l_{ik} l_{jk} \right) \text{ for } i = 1, 2, \ldots, n-1, i > j \qquad (4.36)$$

Consequently, the solution of equation (4.15) is obtained by solving two triangular systems:

Forward substitution: $$Z = L^{-1}c \qquad (4.37)$$

Back substitution: $$\phi = \left(L^{-1}\right)^T Z \qquad (4.38)$$

Since there are p current projections, *i.e.* $c_1, c_2, \cdots, c_p$, their corresponding solutions, *i.e.* $\phi_1, \phi_2, \cdots, \phi_p$, are obtained by repeatedly multiplying Y^{-1} with each current projection. The final solution is re-arranged to give a $np \times 1$ sized dimensional vector:

$$\phi = \left(\phi_1^T, \phi_2^T, \cdots, \phi_p^T\right)^T \qquad (4.39)$$

Since the potential difference measured at each receiving electrode is required a transformation matrix T is introduced into equation (4.39) to give:

$$v = T\phi \qquad (4.40)$$

From equation (4.40), T is a $m \times np$ matrix and each of its columns have only two non-zero entries. One contains +1 and the other -1. In this way the potential difference on each receiving electrode is extracted. All calculations are performed using double precision arithmetic to reduce the effects of numerical round-off errors. The flow chart shown in Figure 4.5 summarises the procedures developed for the forward solver.

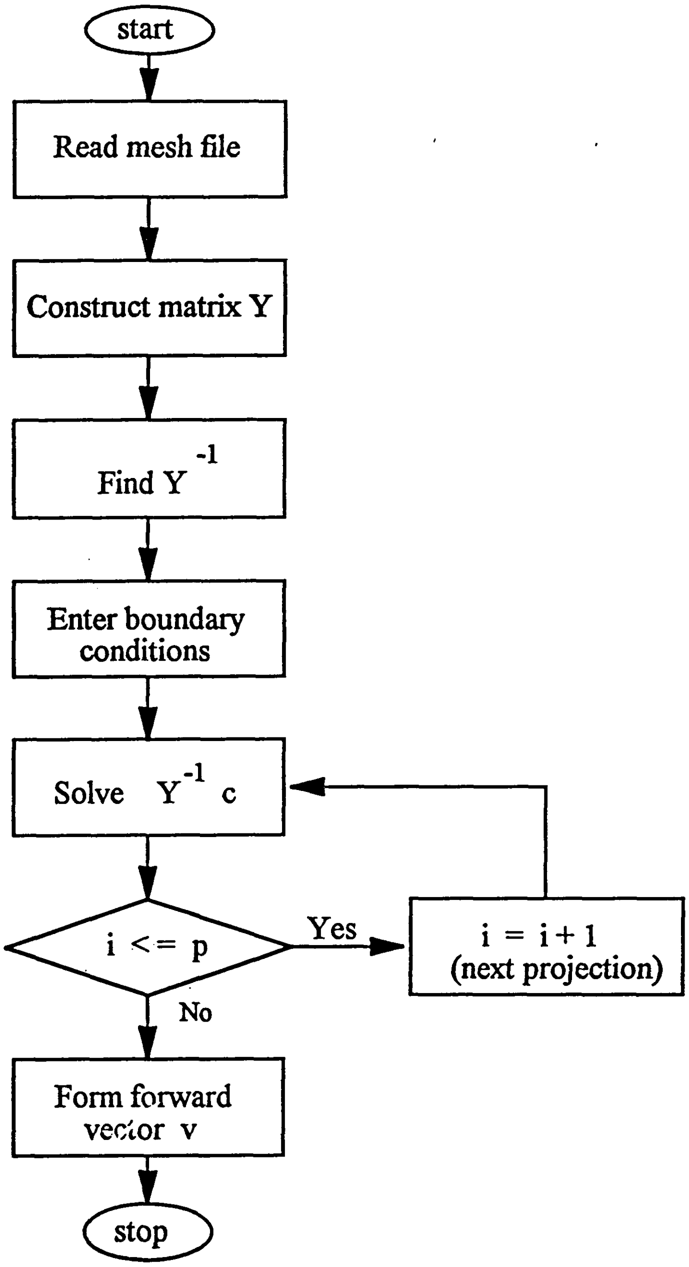

Figure 4.5 Flow chart for the forward solver

4.1.2 Inverse Problem

The ultimate goal of the electrical impedance tomography technique is to produce a cross-sectional image depicting the resistivity distribution of electrically conducting objects inside the process vessel from a set of measured boundary voltages. This procedure is referred to as the inverse problem in EIT. The conductivity/resistivity imaging problem is the inverse of the forward problem and involves the determination of the distribution of conductivity/resistivity within the region from voltage measurements at the surface of the object. For the forward problem specification of the surface current distribution and the conductivity/resistivity distribution it is sufficient to determine the distribution of the voltage within the object. However, a set of surface voltage measurements derived from a single applied current distribution does not carry enough information to uniquely solve for the conductivity/resistivity distribution except under highly constrained conditions. In order to calculate the conductivity/resistivity distribution several independent sets of measurements are needed. Given a set of applied current patterns and their associated surface voltage measurements the inverse problem becomes one of finding a conductivity/resistivity distribution which is consistent with the measurements and any particular constraints that can be applied to the problem. The relationship between the conductivity/resistivity distribution and the surface voltage distribution is a non-linear one and this is bound to present some extra difficulties with the inversion.

The solution of the inverse problem in EIT is not straightforward since the relationship between v and $\rho(x,y)$, where ρ the resistivity is 1/conductivity, is highly non-linear. As such the solution of the inverse problem to produce quantified results, highly desirable for validating process models, generally requires an iterative (multi-step) solver. In an iterative solver, such as the regularised Newton method (Breckon and Pidcock, 1988), the reconstruction process commences with an initial 'predicted' resistivity distribution and uses this to solve the forward problem thereby producing calculated boundary voltages. These calculated voltages are compared to their measured counterparts to produce an 'error' or difference factor which is subsequently used to compute a more accurate resistivity distribution 'map'. This procedure is repeated until the error between the calculated and measured voltages converges to a pre-defined tolerance. In this work the iterative reconstruction algorithm is used. The iterative algorithm is based on the modified Newton-Raphson method.

4.1.2.1 Modified Newton-Raphson (MNR) method

One of the most theoretically orientated iterative reconstruction algorithms developed for image reconstruction in electrical impedance tomography is that based on Yorkey's resistor network (Yorkey, 1986). Using computer simulated data, Yorkey demonstrates the superiority of the MNR algorithm compared to other reconstruction techniques such as the backprojection method (Barber et al, 1983), the perturbation method (Kim *et al,* 1983) and the double-constraint method (Wexler *et al,* 1985). Biomedical EIT investigators such as the RPI group in the USA and the Sheffield University group have not adopted the MNR algorithm for reconstruction because of its convergence problems (Yorkey, 1987). In contrast, Yorkey's colleagues at Wisconsin University reported limited success in applying this algorithm to medical applications, in particular visualisation of the human lung (Woo *et al,* 1992).

The FEM is introduced as a standard tool to solve, what is in effect, a boundary value problem. In essence, the FEM replaces the distributed Laplace equation with a set of linear algebraic equations which are solved to form an *n* dimensional vector *v*. This vector contains *n* independent data sets from a mesh containing *N* boundary electrodes and *p* projection angles. The vector *v* can be written as follows:

$$v_{i,i+1}^{k,k+1} = f(\rho_1, \rho_2, \cdots, \rho_m, I_i, I_{i+1}) \tag{4.41}$$

$$\text{for} \quad \begin{aligned} &1 \le i \le p \\ &i+2 \le k \le N-1,\ i=1 \\ &i+2 \le k \le N,\ i \ne 1 \end{aligned} \qquad (4.42)$$

In equation (4.41) $v_{i,i+1}^{k,k+1}$ denotes the differential voltage measured between the k and $k+1^{th}$ electrodes resulting from a current applied between i and $i+1^{th}$ pair. In order to obtain a complete set of independent measurements, p current patterns are applied and their corresponding boundary voltages calculated. These voltages are 'stacked' to form an n dimensional column vector denoted by v_{cal} while its equivalent sized measured counterparts are denoted by v_{mea}. Following a standard least-squares technique the sum squared difference between v_{cal} and v_{mea} is found which is referred to as the objective function φ (Abdullah *et al.*, 1992). Thus:

$$\varphi = \frac{1}{2}\left[v_{cal} - v_{mea}\right]^T \left[v_{cal} - v_{mea}\right] \qquad (4.43)$$

Hence, an optimal solution to the non-linear inverse problem corresponds to the minimum value of φ. To obtain the minimum φ equation (4.43) is differentiated with respect to each variable in $v_{i,i+1}^{k,k+1}$ and the final result equated to zero. Thus:

$$\varphi' = \left[v'_{cal}\right]^T \left[v_{cal} - v_{mea}\right] \ = \ 0 \qquad (4.44)$$

where the matrix v'_{cal} is given by:

$$\left[v'_{cal}\right]_{ij} = \frac{\partial v_{cal}}{\partial \rho_j} \qquad (4.45)$$

for $i = 1, 2, \dots, n$ and $j = 1, 2, \dots, m$.

The Taylor series expansion of equation (4.44) yields:

$$\varphi'\left(\rho^k\right) \cong \varphi'\left(\rho^k\right) + \varphi''\left(\rho^k\right)\left(\rho-\rho^k\right) \tag{4.46}$$

The second order derivative φ'' appearing in the RHS of equation (4.46) is known as the Hessian matrix H and evaluation of all its entries is one of the most computationally intensive procedures encountered in the MNR-based inverse solver. Moreover, the contribution of the last term in the RHS of equation (4.46) is small and hence, to make considerable economies in computation, the Hessian matrix is approximated to:

$$H = \varphi''(\rho^k) = \left[v'_{cal}\right]^T\left[v'_{cal}\right] \tag{4.47}$$

By substituting equations (4.47) and (4.44) into equation (4.46) and setting the latter to zero gives:

$$\left[v'_{cal}\right]^T\left[v_{cal}-v_{mea}\right]+\left[v'_{cal}\right]^T\left[v'_{cal}\right]\Delta\rho^k \;=\; 0 \tag{4.48}$$

where $\left(\rho-\rho^k\right)$ is denoted as $\Delta\rho^k$. Equation (4.48) can be re-arranged to produce the desired updating equation shown below:

$$\Delta\rho^k = -\left\{\left[v'_{cal}\right]^T\left[v'_{cal}\right]\right\}^{-1}\left[v'_{cal}\right]^T\left[v_{cal}-v_{mea}\right] \tag{4.49}$$

The first derivative v'_{cal}, is also referred to as Jacobian matrix J and it is given by:

$$J \;=\; \left[v'_{cal}\right] \;=\; T\phi' \;=\; T\left(Y^{-1}c\right)' \tag{4.50}$$

where,

$$\frac{\partial Y^{-1}}{\partial p_j} c_i = -Y^{-1} \frac{\partial Y}{\partial p_j} Y^{-1} c_i = -Y^{-1} \frac{\partial Y}{\partial p_j} \phi_i \qquad (4.51)$$

Equation (4.51) is the 'standard' method of forming J despite the availability of alternative methods such as those based on the compensation theorem (Yorkey, 1990). As mentioned by Yorkey, even though the compensation method is more efficient in computing J it is only suitable when the measuring technique is that of the adjacent pairs. In contrast, the standard method offers more flexibility because it can be applied to any measurement technique. Therefore, the standard method was used in this work to form the Jacobian matrix.

The MNR algorithm eventually iterates into a minimum (representing the final solution) using the update equation given in equation (4.49). At the k^{th} iterative step the element vector is updated by:

$$\rho^{k+1} = \rho^{k} + \Delta\rho^{k} \qquad (4.52)$$

As mentioned by Yorkey and subsequently by others (Moesner and Anderson, 1989; Lin *et al*, 1991), the MNR algorithm is capable of quadratic convergence provided that $\Delta\rho$ is small. Consequently, the use of equation (4.49) is only valid in the vicinity of the solution and, if this condition is violated, the progress of the iterative process is frequently erratic and potentially divergent. For large errors in the objective function φ, *i. e.* when the distance between the initial predicted and true resistivity distribution is large the MNR fails to converge to a minimum. Such difficulties are further exacerbated by additional problems such as errors resulting from numerical modelling, limited hardware precision and electrode geometry errors. In this work, initial predicted resistivity distribution which is nearly the same as the true value of the conveying liquid inside the pipe was used to overcome the problems.

In the next section the image reconstruction method for the optical system is outlined.

4.2 Image reconstruction method for optical imaging system

In this work visible light is used to replace X-rays for the scanning of multi-phase flow as suggested by (Dugdale, 1994, Hartley *et. al.*, 1991 and Dugdale *et. al*, 1991). In infra-red transmission systems radiation follows a similar attenuation law to X-rays when the beams cross an air-water system. The laws governing light are complex, but if certain approximations are made, they can be simplified. For the purpose of a simple reconstruction algorithm it is assumed that the beams of light travel in straight lines. In the next sub-section the theory of the method used, which is based on the principle of optical attenuation, is described

4.2.1 Mathematical preliminaries

The rectangular co-ordinate system (x,y) is used to describe any point in the layer under examination (Fig. 4.6). The linear attenuation coefficient μ, is used to describe a property of an object as a whole. The optical density function $f(x,y)$, denotes the contribution of each point towards the final detected image.

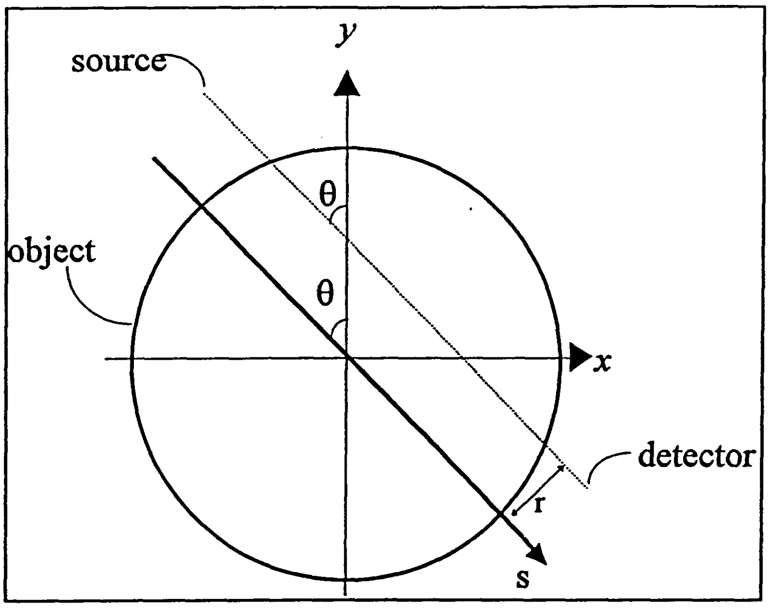

Figure 4.6 Co-ordinate systems. Points within the object are described by a fixed (*x*,*y*) co-ordinate system. Rays (dashed line) are specified by their angle with respect to the *y*-axis, θ and their distance from the origin, *r*. The *s* co-ordinate denotes distance along the ray.

A straight line from the source to the detector, which the path of the radiation follows, is termed the ray-path and is described by an (*r*,*s*) co-ordinate system which is rotated by the same angle as the ray. Each ray is thus represented by a polar coordinate system (*r*,θ), where *r* is the distance from the origin and θ is the angle of the ray with respect to the y-axis. Thus, the line integral of the attenuation coefficient, *f*(*x*,*y*) is given by

$$p(r,\theta) = \int_{r,\theta} f(x,y)\, ds \qquad (4.53)$$

where *p*(*r*,θ) is the linear attenuation coefficient along the ray path, at distance *r* from the origin, and angle θ to the y-axis. Now for optical radiation

$$I = I_0 \exp(-\mu x) \qquad (4.54)$$

where I_0 = original intensity of source

I = measured intensity

μ = linear attenuation coefficient

x = thickness of object

In the following analysis the effects of reflection and refraction are neglected. Only optical attenuation is considered. Then

$$I = I_0 \exp(\alpha_m d_m) \qquad (4.55)$$

where I is the light intensity after a distance d_m, I_0 is the initial light intensity and α_m is the attenuation constant of the medium through which the light is travelling. Therefore, for a constant distance across a circular pipe and a constant light intensity the received light strength is a function of the average attenuation coefficient over the path length.

4.2.2 Image reconstruction for optical tomography

The main purpose of this section of the investigation is to devise a computer algorithm to extract information from a set of limited optical data. Because of physical limitations in real-time industrial applications it is not possible to obtain a large number of projections in optical tomography. Therefore the work presented in this thesis looks for an approximate answer which will contain the principal features of a more exact solution. This work attempts to use techniques from medical tomography (*i.e.* the back-projection method) to extract information from a reduced amount of data.

Measurements of light intensity passing through an object at a certain cross-section make it possible to calculate its internal distribution of optical density. The reconstruction problem is stated as follows: estimate from a finite number of projections the density distribution in the section of the original object. The principle of measurement acquisition is shown in Figure 4.7.

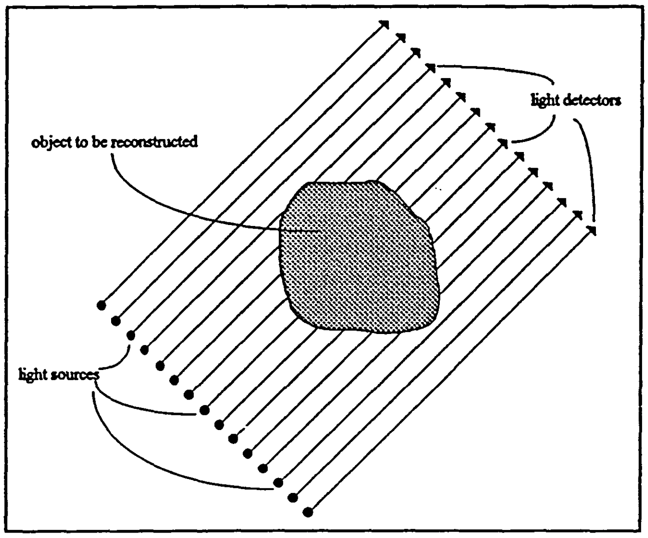

Figure 4.7 Acquisition of the projections

The ray intensity decreases with the density and the length of material passed through. The ray attenuation, called the ray sum P_k, (from equation (4.55)) is proportional to the natural logarithm of the ratio of the incident ray intensity to the passed ray intensity. P_k is the line integral along the ray path of the object density. To solve the integral equation that characterises the image reconstruction problem, the continuous function corresponding to the object density must be determined. The problem also can be stated in a discrete way, by dividing the cross-section in to n small finite squares (*i.e.* pixels) as shown in Figure 4.8.

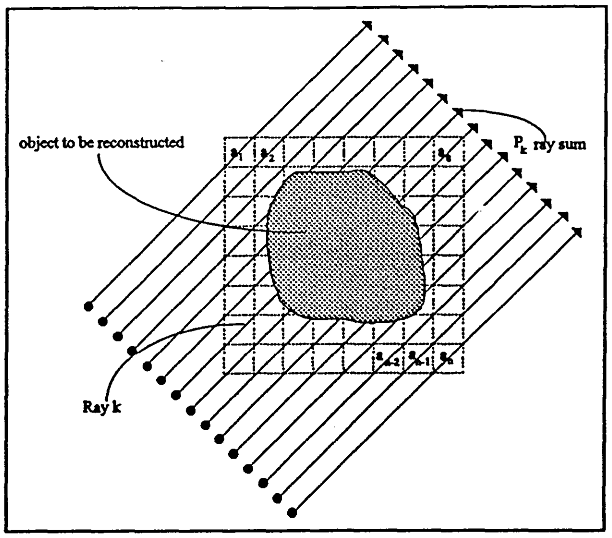

Figure 4.8 The square pixels model for transmission tomography image reconstruction.

Thus

$$P_k = \sum_{j=1}^{n} a_i w_{ik} \qquad (4.56)$$

$i = 1, 2, ..., n$ for each ray,

where P_k is the ray sum of the kth ray (*i. e.* ray attenuation), a_i is the value of the ith pixel, and w_{ik} is a geometric factor corresponding to the effect of the kth ray on the ith pixel; it is zero if the ray does not pass through the pixel. The image reconstruction problem is to determine the pixel values $a_1, a_2, \ldots, a_n$ from the set of ray sums P_k. This work attempts to use the back-projection method because it is straight forward and the optical data is limited to two projections in this system.

4.2.2.1 Back Projection Method

The technique used in this algorithm is referred to as back projection between view lines. The view line consists of pixels along the line between the transmitter and the receiver position. The ray-sum values at the receivers are back projected to light intensity values in the area between the two overlapping lines as shown in Figure 4.9.

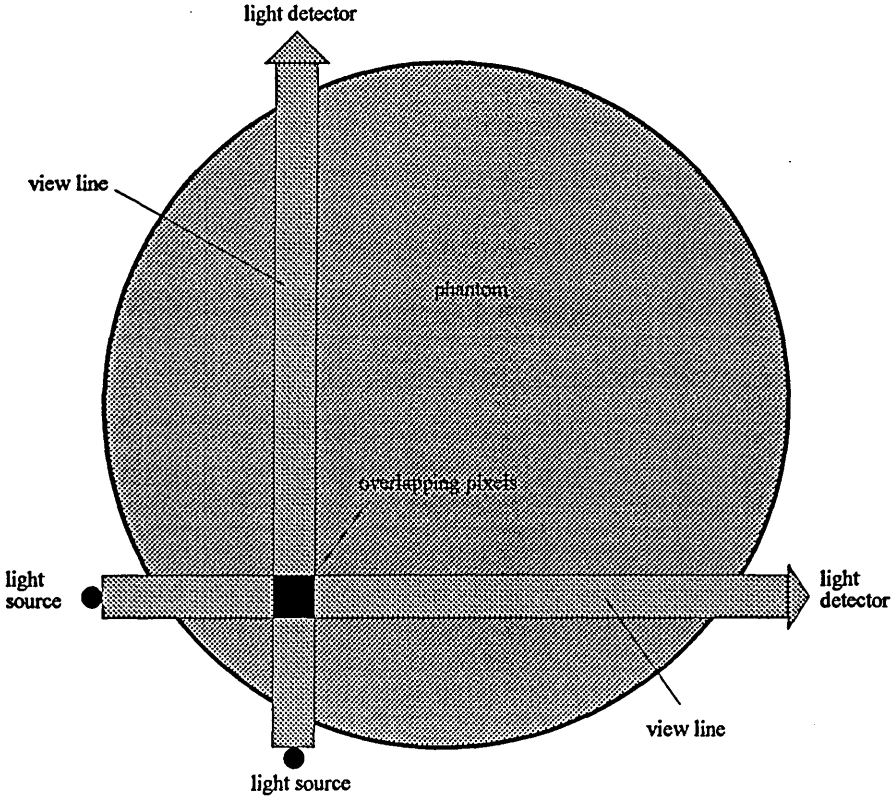

Figure 4.9 Overlapping pixels for two view lines

The density for each point in the reconstructed image is obtained by summing up the densities of all the rays which pass through that point. Reconstruction is performed by back-projecting each profile across the plane *i.e.* the magnitude of each ray-sum is applied to all points that make up the ray. The process may be described by the equation

$$\hat{f}(x,y) = \sum_{j=1}^{m} p(x\cos\theta + y\sin\theta)\Delta\theta \qquad (4.57)$$

which is the general case for *m* projections where θ = is the *j*th projection angle

$\Delta\theta$ = is the angular distance between projections and the summation extends over all the *m* projections

$\hat{f}(x,y)$ is only used to emphasise that the density values are not equivalent to the true densities *f*.

Therefore for a constant distance across a circular pipe and a constant initial light intensity, the final light intensity measured at the receivers can be obtained by summing up all the pixel values of all the rays which pass through the sensing path as shown in Figure 4.10. Hence, for the limited data provided by the two projections, the whole of the pipe cross section, which is represented by 16×16 squares, can be obtained by superimposing the sensitivity paths produced by each projection.

This reconstruction algorithm is designed to reconstruct images where two orthogonal projections are used (Figure 4.10). This arrangement of a square with all views of equal length relates to the experimental set up (Daniels *et. al.*, 1993b). There are 16 parallel beams for each projection. Each beam is regarded as having one source and one detector. The output signals from the detectors are preprocessed so that a zero value is obtained if the beam traverses an opaque object and a maximum value (256) is obtained if the beam traverses through an empty pipe. This is achieved by mapping 5 volts to value 256 and 0 volt to value 0. Between these limits the processed detector signal corresponds to the medium through which the light is travelling as in equation (4.55).

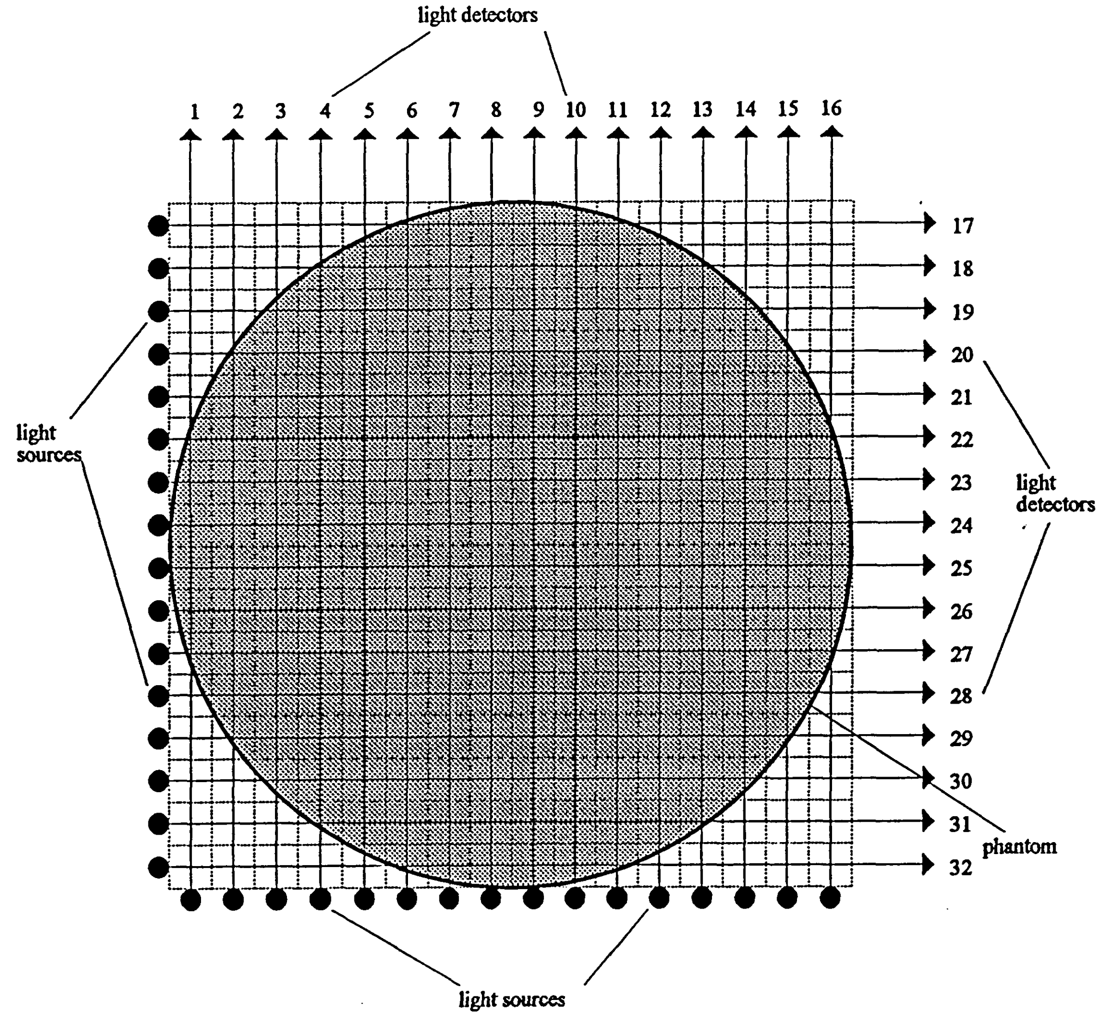

Figure 4.10 The square model that was used for optical measurements

The overall function of the reconstruction algorithm can be summarised by the following segment of pseudo-code and flowchart (Figure 4.11).

```
BEGIN
    Read input values for all views
    REPEAT
        Check if ray sum for this view represents water
        IF represent water, indicate all pixels for this view as water pixels
    UNTIL end of view (i.e 32 views)
    REPEAT
        REPEAT
            Check if pixel $_j$ in this view is water pixel
            IF water pixel THEN accumulate temporary ray sum
            ELSE  increment counter for pixel not water
                  store the position of j
        UNTIL (j > 16)
        Assign all pixels that are not water =
            (measured ray sum - temporary ray sum) / total pixels not water
    UNTIL end of projection (i.e 2 projections)
END
```

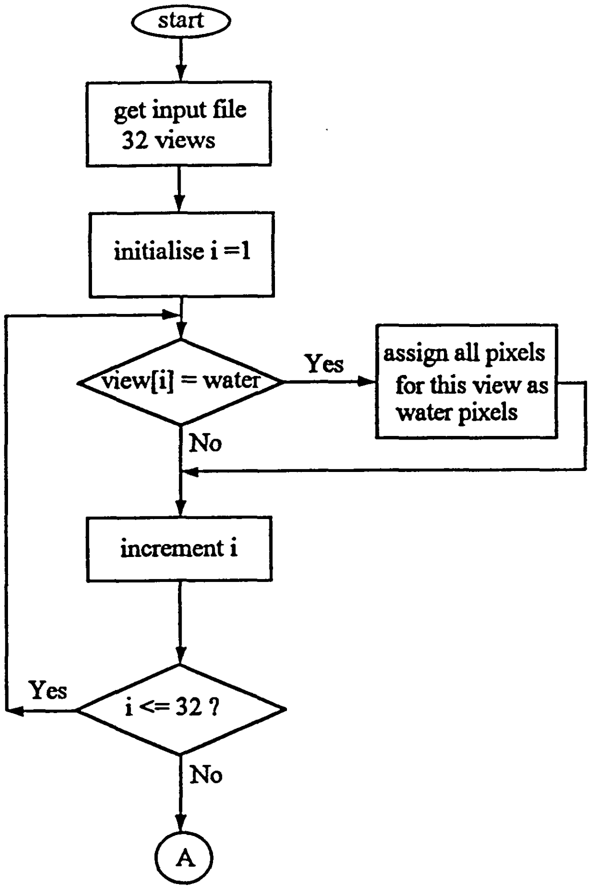

Figure 4.11 Flowchart for the image reconstruction of optical system

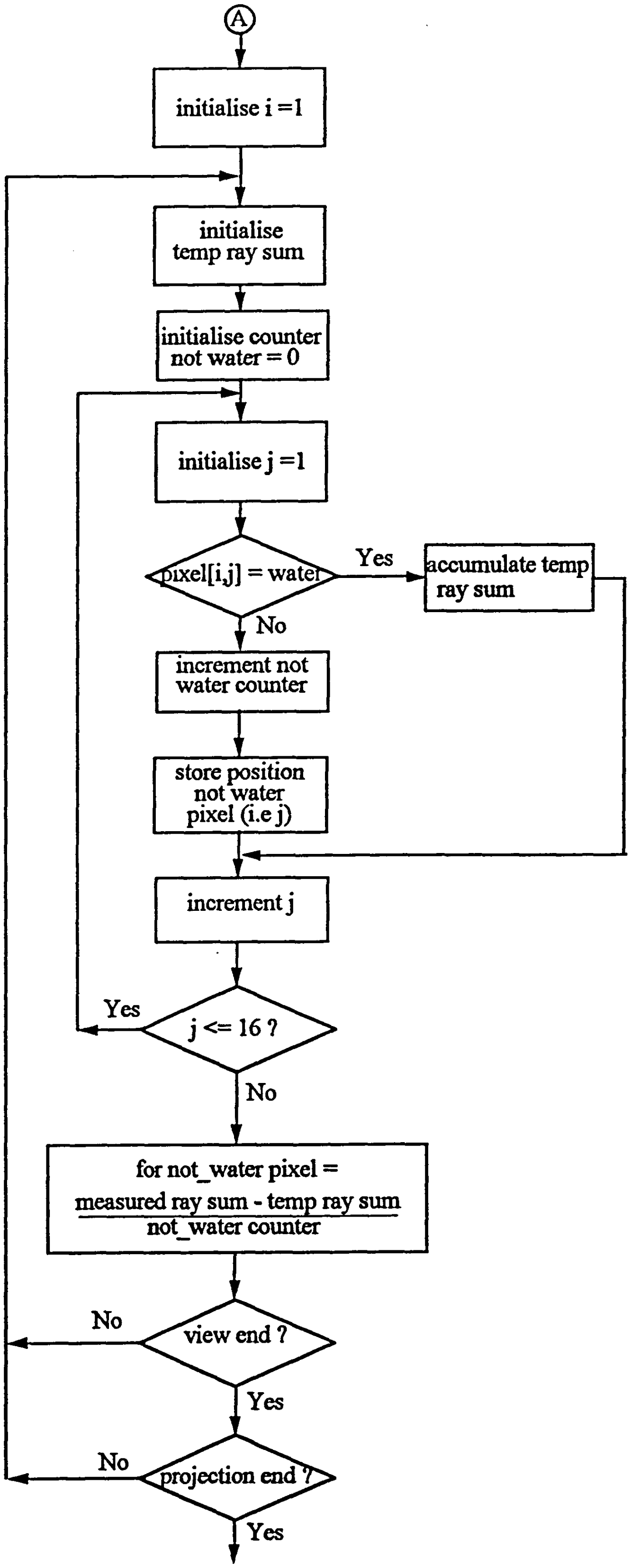

Figure 4.11 (cont.) Flowchart for the image reconstruction of optical system

4.3 Dual modality tomography image reconstruction

Dual modality tomography images are produced by superimposing images obtained by both EIT and optical measurements (Figure 4.12). Tomographic images from EIT use a range of colours to represent pixel resistivity and tomographic images from optical measurements use a range of patterns to represent optical transmissivity. When both tomographic images are superimposed the final image is a combination of colours and patterns. Both techniques display an image based on a 16×16 array. From these colours and patterns various properties with respect to conductivity/resistivity and translucence to light can be obtained. A set of results produced by superimposing these two techniques are discussed more detail in Chapter 7.

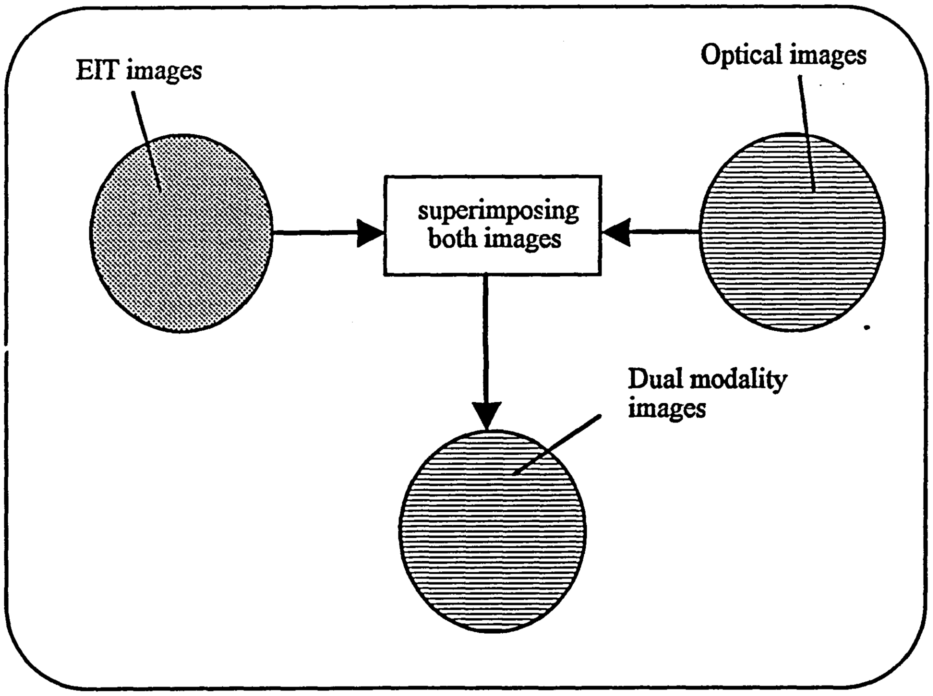

Figure 4.12 Superimposed both EIT and optical images to produce dual modality image

For the optical part of the dual modality reconstruction algorithm, the pixel values representing the light intensity, which are displayed by patterns on the screen, are stored in an array OPT(32, 32). The information concerning the resistivity values, which are represented by colours, are stored in another array EIT(32, 32). The OPT data has better resolution but the reconstructions suffer from aliasing. The EIT data is less accurate, but does not suffer from aliasing.

Reconstruction is based on OPT and wherever a "non-water" pixel is detected, this is overwritten for cases where the corresponding EIT data says "water". In order to restore the correct pattern for this particular pixel, a corresponding pattern which is equivalent to the mean of the OPT data is assigned. This procedure is repeated until all the pixels in the optical array are investigated. This procedure is summarised in the flowchart shown in Figure 4.13. See Section 8.3 parts (j), (k) and (l) for suggestions on improvements to dual modality displays.

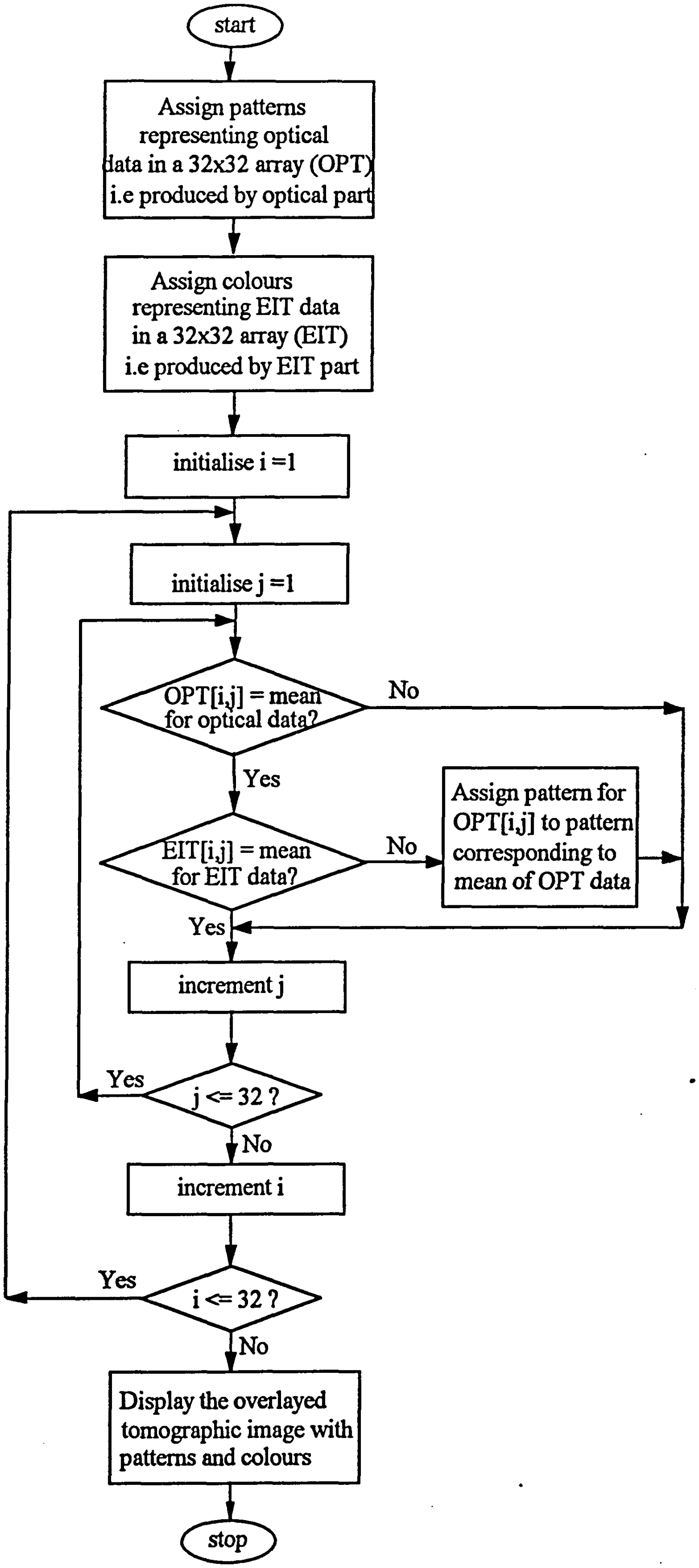

Figure 4.13 Flowchart to superimpose optical and EIT data to produce a dual modality image.

5. Results from numerical simulated data for EIT

5.1 Introduction

In this chapter some numerical test results connected with phantom studies, which are usual in computerised tomography reconstruction techniques (Yorkey, 1986; Griffiths and Ahmed, 1987), are presented. The structure of the object is a circular phantom into which circular rods of specified resistivity are inserted. Experimental data was not available, so simulated data was generated by applying appropriate approximate solutions of the forward problem and this data used for analysis. For simulation purposes approximate solutions of the boundary potential (voltages) measurements are required. In this chapter the simulated measurements are obtained by using the finite element method in the forward solver to determine the boundary voltages used. As mentioned in Chapter 4, the reconstruction is based on the modified Newton Raphson technique.

5.2 Test data

To analyse the performance of the image reconstruction algorithm used in the EIT investigation, a sequence of reconstructions using various phantoms is performed on a simulated vessel of 10 cm diameter.

In order to quantify the areas represented by pixels of different resistivities and relate them to the object areas, the number of pixels for each resistivity are summed and their percentage area of the total image area determined from

$$\frac{\sum \text{pixels of specified resistivity}}{824} \times 100\%$$

The results provide quantifiable information relating to measurement accuracy and resolution (Section 5.3).

The results of the simulations are as follows:

a) Phantom study 1

In this case a 10 cm diameter vessel full of air is used and the reconstructed image is shown in Figure 5.1(b).

b) Phantom study 2

In this case a 2.5 cm diameter air bubble, represented by a resistivity in excess of 1000 Ω cm, is placed at the centre of the 10 cm diameter 500 Ω cm representing the vessel background resistivity, as shown in Figure 5.2(a). The reconstructed image is shown in Figure 5.2(b).

c) Phantom study 3

In this case a 2.5 cm diameter perspex rod, represented by a resistivity of 960 Ω cm, is placed at the centre of a 10 cm diameter 500 Ω cm, representing the vessel background resistivity as shown in Figure 5.3(a). The reconstructed image is shown in Figure 5.3(b).

d) Phantom study 4

In this example the resolution of the reconstruction is illustrated. This phantom consists of two 2.5 cm diameter perspex rods with the same resistivity. The position of the phantom is shown in Figures 5.4(a) and 5.5(a). The aim of the investigation is to see if it is possible to distinguish the two rods. The results are shown in Figures 5.4(b) and 5.5(b).

e) Phantom study 5

In this example the result of using different resistivity objects is illustrated. The phantom consists of a 2.5 cm diameter aluminium rod, represented by a resistivity of 360 Ω cm, and a 2.5 cm diameter air bubble, represented by a resistivity of 1000 Ω cm. The position of the phantom is shown in Figures 5.6(a) and 5.7(a). The aim of the investigation is to see if it is possible to distinguish the two rods with different resistivities. The reconstructed image is shown in Figures 5.6(b) and 5.7(b).

f) Phantom study 6

In this example the effects on the reconstruction when the water level of a horizontal pipe varies from nearly full to nearly empty are investigated. The reconstructed images are shown in Figures 5.8(b), 5.9(b) and 5.10(b).

g) Phantom study 7

The final example illustrates the results obtained when the aluminium rods, represented by a resistivity of 360 Ω cm, are placed inside a horizontal pipe for varying depths of water level. The aim of the investigation is to see if it is possible to distinguish the air, water and aluminium rod (solid) in a horizontal pipe. The results are shown in Figures 5.11(b), 5.12(b) and 5.13(b).

Percentage area of air = 100%

Area Resistivity
<0hm cm)

1000
and above

(b)

Figure 5.1 Reconstruction for the EIT system for a 10 cm diameter vessel full of air.
a) actual position b) reconstructed

Percentage area of water = 93.75%
Percentage area of air = 6.25%

Resistivity
<Ohm cm)

1000
and above

71

(b)

Figure 5.2 Reconstruction for the EIT system for a 2.5 cm diameter of air bubble (1000 D cm) placed at the centre of a 10 cm diameter 500 ***Q*** cm saline filled vessel.
a) actual position b) reconstructed

Percentage area of water = 93.75%
Percentage area of perspex = 6.25%

(a)

Resistivity
<0hm cm)

(b)

Figure 5.3 Reconstruction for the EIT system for a 2.5 cm diameter of perspex rod (960 Q cm) placed at the centre of a 10 cm diameter 500 Q cm saline filled vessel.
a) actual position b) reconstructed

Percentage area of water = 87.5%
Percentage area of perspex = 12.5%

perspex perspex

(a)

(b)

Figure 5.4 Reconstruction for the EIT system for two 2.5 cm diameter of perspex rods (960 Q cm) placed in a 10 cm diameter 500 ***Q*** cm saline filled vessel, a) actual position b) reconstructed

Percentage area of water = 87.5%

Percentage area of perspex = 12.5%

(a)

Area <*>

Resistivity (Ohm cm)

(b)

Figure 5.5 Reconstruction for the EIT system for two 2.5 cm diameter of perspex rods (960 Q cm) placed in a 10 cm diameter 500 ***Q*** cm saline filled vessel, a) actual position b) reconstructed

Percentage area of water =87.5%
Percentage area of air = 6.25%
Percentage area of aluminium = 6.25%

(a)

fVea Resistivity
C-O <Qhm cm>

(b)

Figure 5.6 Reconstruction for the EIT system for a 2.5 cm diameter of aluminium rod (360 ***fl*** cm) and a 2.5 cm diameter air bubble (1000 ***Q*** cm) placed in a 10 cm diameter 500 Q cm saline filled vessel,
a) actual position b) reconstructed

Percentage area of water = 87.5%
Percentage area of air = 6.25%
Percentage area of aluminium = 6.25%

water

(a)

Area
Resistivity (Ohm cm)

(b)

Figure 5.7 Reconstruction for the EIT system for a 2.5 cm diameter of aluminium rod (360 Q cm) and a 2.5 cm diameter air bubble (1000 Q cm) placed in a 10 cm diameter 500 Q cm saline filled vessel,
a) actual position b) reconstructed

Percentage area of water = 85.93%

Percentage area of air = 14.07%

air

2 cm

water

8 cm

Area <>;>

Resistivity <Qh» c»>

(b)

Figure 5.8 Reconstruction for the EIT system for a 10 cm diameter horizontal pipe when the depth of the water is 8 cm.
a) actual position b) reconstructed

Percentage area of water = 50%
Percentage area of air = 50%

water

(a)

Resistivity
<0h» cm)

5.34

1030
end above

(b)

Figure 5.9 Reconstruction for the EIT system for a 10 cm diameter horizontal pipe when the depth of the water is 5 cm.
a) actual position b) reconstructed

Percentage area of water = 14.07%

Percentage area of air = 85.93%

8 cm

water

Area <V.)

Resistivity <0h» cm)

(b)

Figure 5.10 Reconstruction for the EIT system for a 10 cm diameter horizontal pipe when the depth of the water is 2 cm.
a) actual position b) reconstructed

Percentage area of water = 73.43%
Percentage area of aluminium = 12.5%
Percentage area of air = 14.07%

water

aluminium

aluminium

(b)

Figure 5.11 Reconstruction for the EIT system for a 10 cm diameter horizontal pipe when the depth of water is 8 cm and two 2.5cm diameter of aluminium rods (360 Q cm) are placed inside the pipe,
a) actual position b) reconstructed

Percentage area of water = 37.5%
Percentage area of aluminium = 12.5%
Percentage area of air = 50%

water

aluminium

aluminium

(a)

0.971

(b)

Figure 5.12 Reconstruction for the EIT system for a 10 cm diameter horizontal pipe when the depth of water is 5 cm and two 2.5cm diameter of aluminium rods (360 Q cm) are placed inside the pipe,
a) actual position b) reconstructed

air

Percentage area of water = 12.51%
Percentage area of air = 85.93%
Percentage area of aluminium = 1.56%

8 cm

aluminium

water

Area (%) Resistivity (Ohm cm)

(b)

Fig 5.13 Reconstruction for the EIT system for a 10 cm diameter horizontal pipe when the depth of water is only 2 cm and 1.25cm diameter of aluminium rod (360 Ω cm) is placed inside the pipe,
a) actual position b) reconstructed

5.3 Results and discussion

The results of the simulations shown in Figures 5.1 - 5.13 are now discussed.

5.3.1 With the vessel full of air (Figure 5.1) the reconstruction indicates 100% air, which is the only fully correct reconstruction. This would also be true if the simulation were for the system filled with water.

5.3.2 The introduction of simulated bubbles shows the resistivity gradient profile across the boundary between bubble and water. This is typical of EIT reconstruction. The measured percentage of water is 86.4% (actual 93.75%) and that of air is 3.95% (actual 6.25%). The ambiguity in the measurement is 10.7%.

5.3.3 When an object of perspex which has a slightly lower conductivity than water is used, the measured water percentage is 86.4% (actual 93.75%) but for the perspex is 5.3% (actual 6.25%). This improvement is due to the closer proximity of the two resistivities than in Section 5.3.2.

5.3.4 However, the modelling of two perspex rods, each having the same area as the single rod in Section 5.3.3, does not show the expected doubling of measured perspex - 8.3% (actual 12.5%). The increased error may be due to the relative increase in boundary between perspex and water (doubled) compared with the decrease in area of the water (93.75 down to 87.5%).

5.3.5 This result is very similar to Section 5.3.4. It has been chosen because it causes aliasing with optical reconstructions (Sections 6.3.5).

5.3.6 This result shows the effects of two objects, one with increased resistivity (air), the other with decreased resistivity (aluminium) compared with that for water. The results show the area of water to be 83.1% (actual 87.5%), the area of aluminium is approximately 7% (actual 6.25%) and gas 4.6% (actual 6.25%). The results of 2.9% and 4.1% have been summed for the aluminium because the resistivity of 360 Ω cm is very near the scale boundary of 370 Ω cm.

5.3.7 This is similar to Section 5.3.6, and has very similar results. These two simulations are included because Section 5.3.6 shows aliasing with optical tomography (Section 6.3.6).

5.3.8 This investigation is very relevant to liquid flow in a sewer, with a layer of air above the drain liquid. The major volume of the liquid has an area in the cross-section of 83.7% (actual 85.93%), however the air is shown as only 6.8% (actual 14.07%). Again there is a large resistivity gradient which is shown in the results as an area of ambiguity.

5.3.9 When the liquid flow in a sewer is half full, the measured percentage of water is 46.1% (actual 50%) and gas 41.4% (actual 50%). The ambiguity in the measurement is 12.86%.

5.3.10 This result shows when the quantity of the conveying liquid in a sewer is much smaller than air. The major volume of the air has an area in the cross-section of 76.7% (actual 85.93%), however the conveying liquid is shown as only 10.0% (actual 14.07%). Again there is a large resistivity gradient which is shown in the results as an area of ambiguity.

5.3.11 This and the next two simulations investigates the effect of conducting solid and varying water depth. With mainly water the reconstruction gives water 69.2% (actual 73.43%), aluminium 13.6% (actual 12.5%) and air 6.8% (actual 14.07%). Again the largest resistivity gradient produces the greatest error.

5.3.12 There is 50% air in this simulation, but the result for air is 40.8%. The results for water 23.5% (actual 37.5%) and aluminium 13.3% (actual 12.5%). This simulation is based on a restricted data set – half the sensors are in air – and this is the reason for artefact in the centre between the two rods.

5.3.13 This simulation investigates the presence of solids when the sewer has a very low level of liquid. The water presence is reconstructed to 8.7% (actual 12.51%), aluminium rod to 1.2% (actual 1.56%) and air to 76.9% (actual 85.93%).

5.3.14 Summary

The test results obtained using the phantoms show that the images produced by this reconstruction method agree quantitatively with the physical models; thus they encourage further research. From the observations, the results also show some limitations in reconstructed picture quality which may be improved by increasing the number of sensors.

a) *Resolution.* The image resolution of the system is not high. The image resolution is mainly limited by the number of independent measurements obtained from the measurement system. Increasing the number of electrodes will improve the image quality and accuracy, but at the cost of reconstruction speed.

b) *Accuracy.*

Figures	Water		Air		Aluminium		Perspex	
	Modelled	Actual	Modelled	Actual	Modelled	Actual	Modelled	Actual
5.1			100.0	100.0				
5.2	86.4	93.75	3.95	6.25				
5.3	86.4	93.75					5.3	6.25
5.4	80.6	87.5					8.3	12.5
5.5	80.6	87.5					8.3	12.5
5.6	83.1	87.5	4.6	6.25	7.0	6.25		
5.7	83.1	87.5	4.6	6.25	7.0	6.25		
5.8	83.7	85.93	6.8	14.07				
5.9	46.1	50.0	41.4	50.0				
5.10	10.0	14.07	76.7	85.93				
5.11	69.2	73.43	6.8	14.07	13.6	12.5		
5.12	23.5	37.5	40.8	50.0	13.3	12.5		
5.13	8.7	12.51	76.9	85.93	1.2	1.56		

Table 5.1 Analysis of accuracy for EIT reconstruction

From the above table it can be seen that the aluminium rods are the most accurately reconstructed with an accuracy varying between 6.4% to 23%. For perspex the accuracy varies between 9.3% and 33.6%. For water the accuracy varies between 2.6% and 53.0%. For air the accuracy varies between 10.7% and 51.7%.

c) *Speed.* The MNR algorithm is highly CPU intensive and spends over 90% of its time performing matrix multiplication functions (Abdullah *et al.*, 1992). One of the ways to increase the speed of computation is by using parallel processor arrays such as the INMOS Transputer Series, to boost the reconstruction speed as discussed by (Cook and Dickin, 1993; Artola and Dell, 1993).

The results shown in Sections 5.3.11 to 5.3.13 are significant, because they indicate that useful reconstruction may be obtained with widely differing levels of liquid.

5.4 Conclusion

Despite the limitations in accuracy expressed in the results, this technique demonstrates the potential for imaging volume flow for sewers if combined with another modality such as optical tomography. This technique is inexpensive and is likely to be suitable for long-term monitoring and screening procedures.

6. Results for the numerical simulated data for optical tomography

6.1 Introduction

This chapter concentrates on numerical test results connected with phantom studies using optical measurements to produce tomographic images. Simulated data is generated based on the optical tomographic data capture system proposed by Dugdale (1994) for mathematical modelling. The image reconstruction algorithm is adapted from X-ray tomography as used in medical imaging systems.

6.2 Test data

In order to analyse the performance of the optical image reconstruction algorithm used in this investigation, a sequence of reconstructions using the same phantoms as used in Chapter 5 is performed. Different components in a fluid flow may have different optical absorption coefficients. The attenuated radiation is modelled by equation (6.1) and enables the identification of particular components in a fluid flow.

The intensity at the receiver, I, due to the physical path lengths in water (d_w) and air (d_a) where absorption occurs is related to the initial intensity, I_0, by,

$$I = I_0 \, e^{-(\alpha_w d_w + \alpha_a d_a)} \qquad (6.1)$$

where α_a and α_w are absorption coefficients of air and water. For the following simulations these are 0.142 cm^{-1} and 0.287 cm^{-1} respectively (Dugdale, 1994).

With the pipe full of air, the outputs of simulated sensors 7 to 10, 23 to 26 have been scaled to 5.0 volts and converted to a digital representation of 256, where no light is 0.0 volt and a digital representation of 0. The path length for receiver R1 must always contain a path length in water of 2 × 3.28 cm (Figure 6.1(a)). Paths 1 to 6 contain permanent paths in water, but of decreasing length. Paths 16 to 11, 17 to 22 and 32 to 27 are the same for the phantom filled with air as paths 1 to 6.

The studies on the phantoms are as follows:

a) Phantom study 1

The study starts with the case of a 10 cm diameter vessel full of air as shown in Figure 6.1(a). The detected intensity when the beam passes through a 10 cm diameter pipe full of air at various sensors position around the pipe (the forward problem) is shown in Table 6.1. The reconstructed image obtained for this case is shown in Figure 6.1(b).

b) Phantom study 2

In this case a 2.5 cm diameter air bubble is modelled. The bubble is placed at the centre of the 10 cm diameter pipe as shown in Figure 6.2(a). The numerical results modelled for this case (the forward problem) are shown in Table A1. The reconstructed image obtained with this data is shown in Figure 6.2(b).

c) Phantom study 3

This study was conducted to investigate whether material slightly less translucent than an air bubble can be differentiated by this algorithm. A 2.5 cm diameter of perspex rod (α_p = 0.34 cm^{-1}) is placed at the centre of the 10 cm diameter pipe and surrounded by water as shown in Figure 6.3(a). The results modelled for this case are shown in Table A2. The resulting reconstructed image is shown in Figure 6.3(b).

d) Phantom study 4

The next question to be investigated is whether or not it is possible to distinguish two separate objects with respect to their position in the pipe. The phantom now consists of two 2.5 cm diameter perspex rods positioned in the 10 cm diameter pipe containing water as shown in Figures 6.4(a) and 6.5(a) respectively. Results for the forward problem are shown in Tables A3 and A4. The results are shown in Figures 6.4(b) and 6.5(b) respectively.

In this study, the two objects can be identified if placed as shown in Figure 6.4(a). If the two objects are placed at opposite sides of the pipe, as shown in Figure 6.5(a), the reconstructed image produces a non-unique solution. This is due to the limited number of projections (in this case only two) used to identify the objects. To overcome this problem, more projections are needed as discussed in further work, Section 8.3.

e) Phantom study 5

In this example, different materials (one is opaque and the other is translucent) are placed as shown in Figures 6.6(a) and 6.7(a). Results for the forward problem are shown in Tables A5 and A6. The method used can identify the two materials as shown by the reconstructions in Figures 6.6(b) and 6.7(b), but may not determine uniquely the position of the objects as shown in Figure 6.6(a). Again this is because of the limited number of projections used in this investigation.

f) Phantom study 6

In this example the effects of varying water level of a horizontal pipe from nearly full to nearly empty are investigated. The physical models for three different liquid levels are shown in Figures 6.8(a), 6.9(a) and 6.10(a). Results for the forward problem are shown in Tables A7, A8 and A9. The reconstructed images are shown in Figures 6.8(b), 6.9(b) and 6.10(b).

g) Phantom study 7

The final example illustrates the results obtained when the aluminium rods (opaque) are placed inside a horizontal pipe for varying depths of water level (Figures 6.11(a), 6.12(a) and 6.13(a)). Results for the forward problem are shown in Tables A10, A11 and A12. The aim of this investigation is to see if it is possible to distinguish the air, water and aluminium rod in a horizontal pipe. The results are shown in Figures 6.11(b), 6.12(b) and 6.13(b).

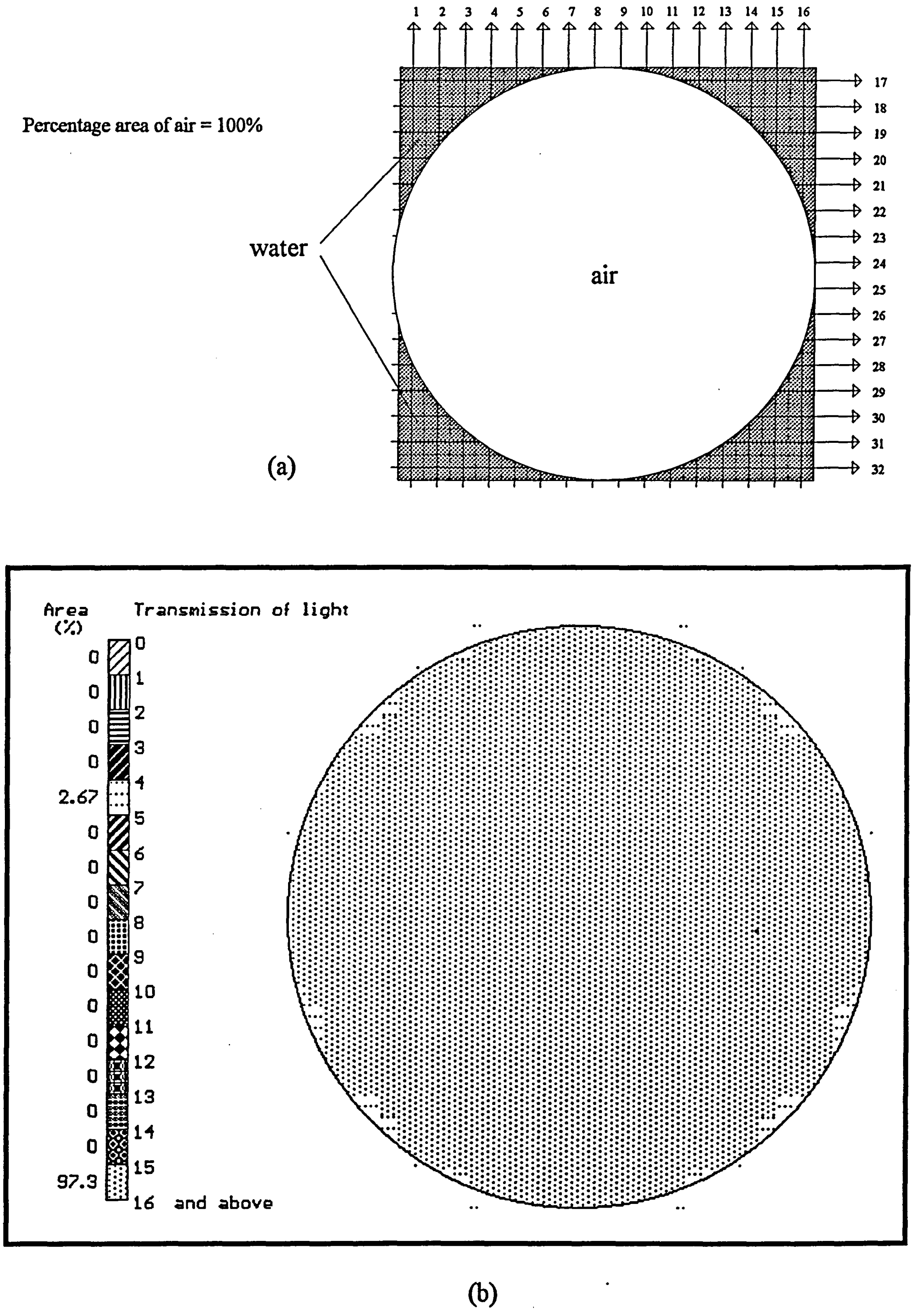

Figure 6.1 Reconstruction for the optical system for a 10 cm diameter vessel full of air.
a) actual position b) reconstructed

Receiver	d_w (path length in water)	d_a (path length in air)	d_w (path length in water)	voltage (V)	bit representation
R1	3.28	3.44	3.28	1.9314	96
R2	2.19	5.62	2.19	2.6495	128
R3	1.41	7.18	1.41	3.3219	176
R4	0.94	8.12	0.94	3.8071	192
R5	0.47	9.06	0.47	4.3629	224
R6	0.31	9.38	0.31	4.5702	240
R7		10.0		5.0	256
R8		10.0		5.0	256
R9		10.0		5.0	256
R10		10.0		5.0	256
R11	0.31	9.38	0.31	4.5702	240
R12	0.47	9.06	0.47	4.3629	224
R13	0.94	8.12	0.94	3.8071	192
R14	1.41	7.18	1.41	3.3219	176
R15	2.19	5.62	2.19	2.6495	128
R16	3.28	3.44	3.28	1.9314	96
R17	3.28	3.44	3.28	1.9314	96
R18	2.19	5.62	2.19	2.6495	128
R19	1.41	7.18	1.41	3.3219	176
R20	0.94	8.12	0.94	3.8071	192
R21	0.47	9.06	0.47	4.3629	224
R22	0.31	9.38	0.31	4.5702	240
R23		10.0		5.0	256
R24		10.0		5.0	256
R25		10.0		5.0	256
R26		10.0		5.0	256
R27	0.31	9.38	0.31	4.5702	240
R28	0.47	9.06	0.47	4.3629	224
R29	0.94	8.12	0.94	3.8071	192
R30	1.41	7.18	1.41	3.3219	176
R31	2.19	5.62	2.19	2.6495	128
R32	3.28	3.44	3.28	1.9314	96

Table 6.1 Light intensity modelling for input to optical system for a 10 cm diameter vessel full of air.

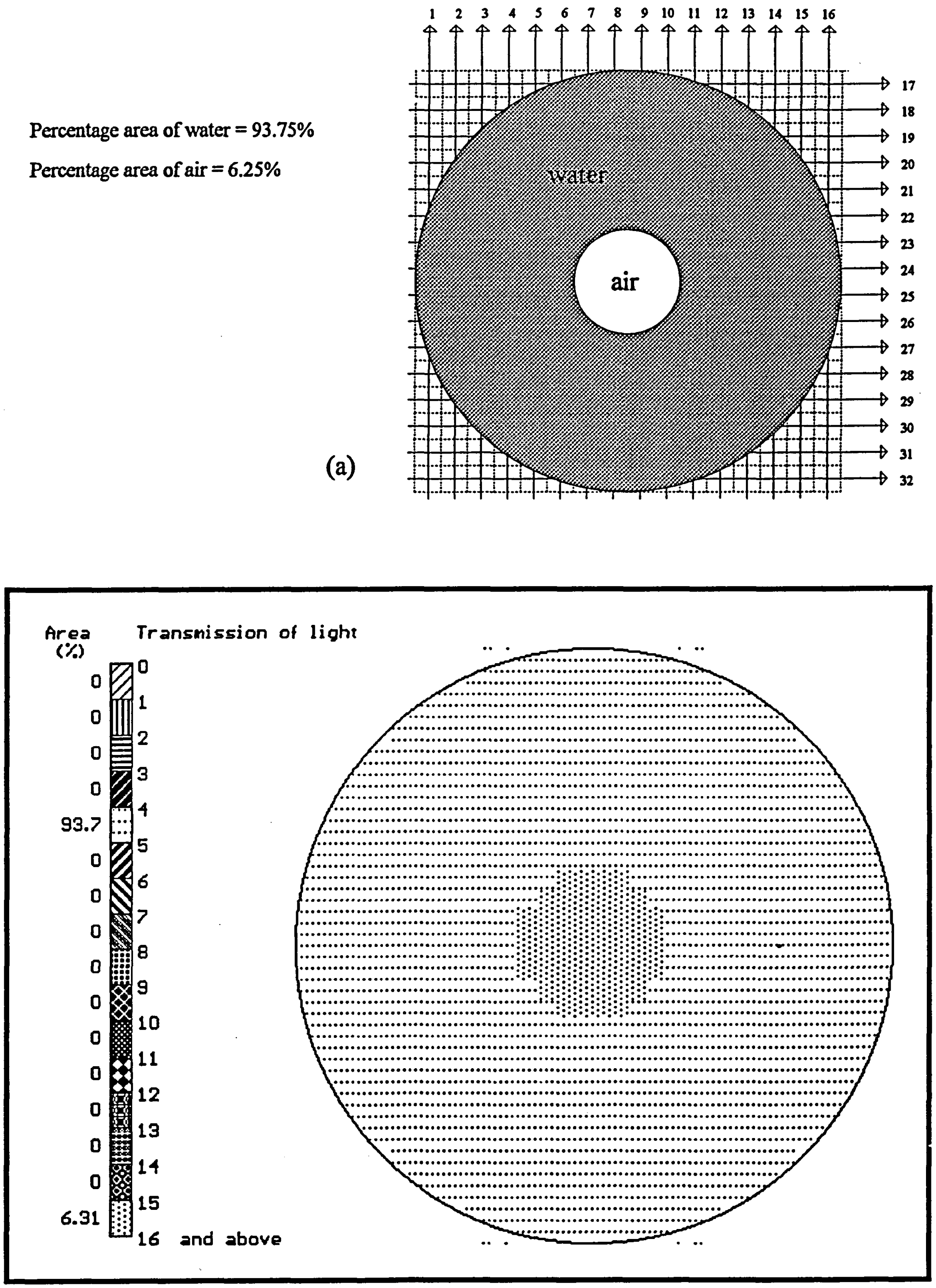

(b)

Figure 6.2 Reconstruction for the optical system for a 2.5 cm diameter of air bubble placed at the centre of a 10 cm diameter saline filled vessel.
a) actual position b) reconstructed

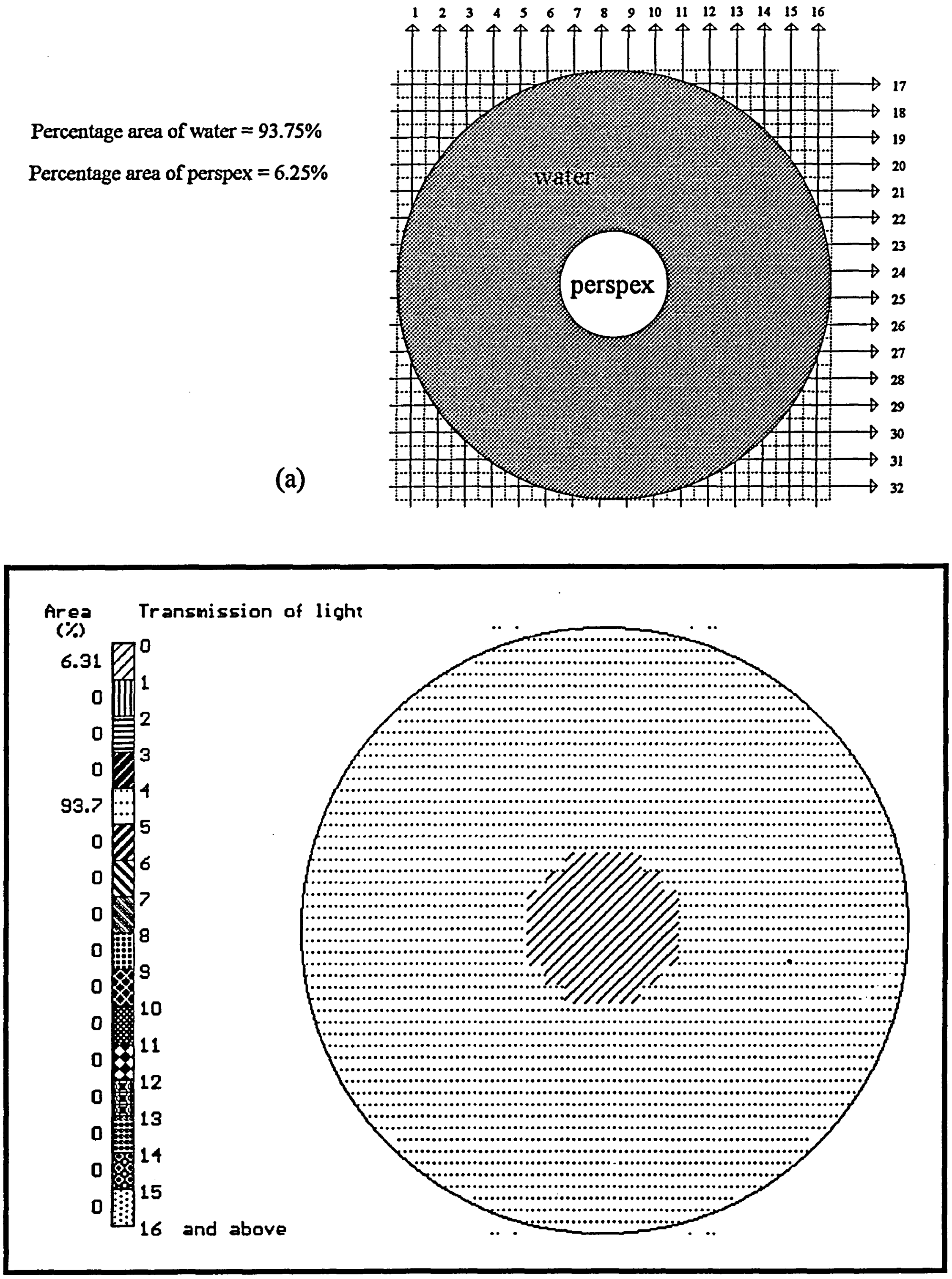

Figure 6.3 Reconstruction for the optical system for a 2.5 cm diameter of perspex rod placed at the centre of a 10 cm diameter cm saline filled vessel.
a) actual position b) reconstructed

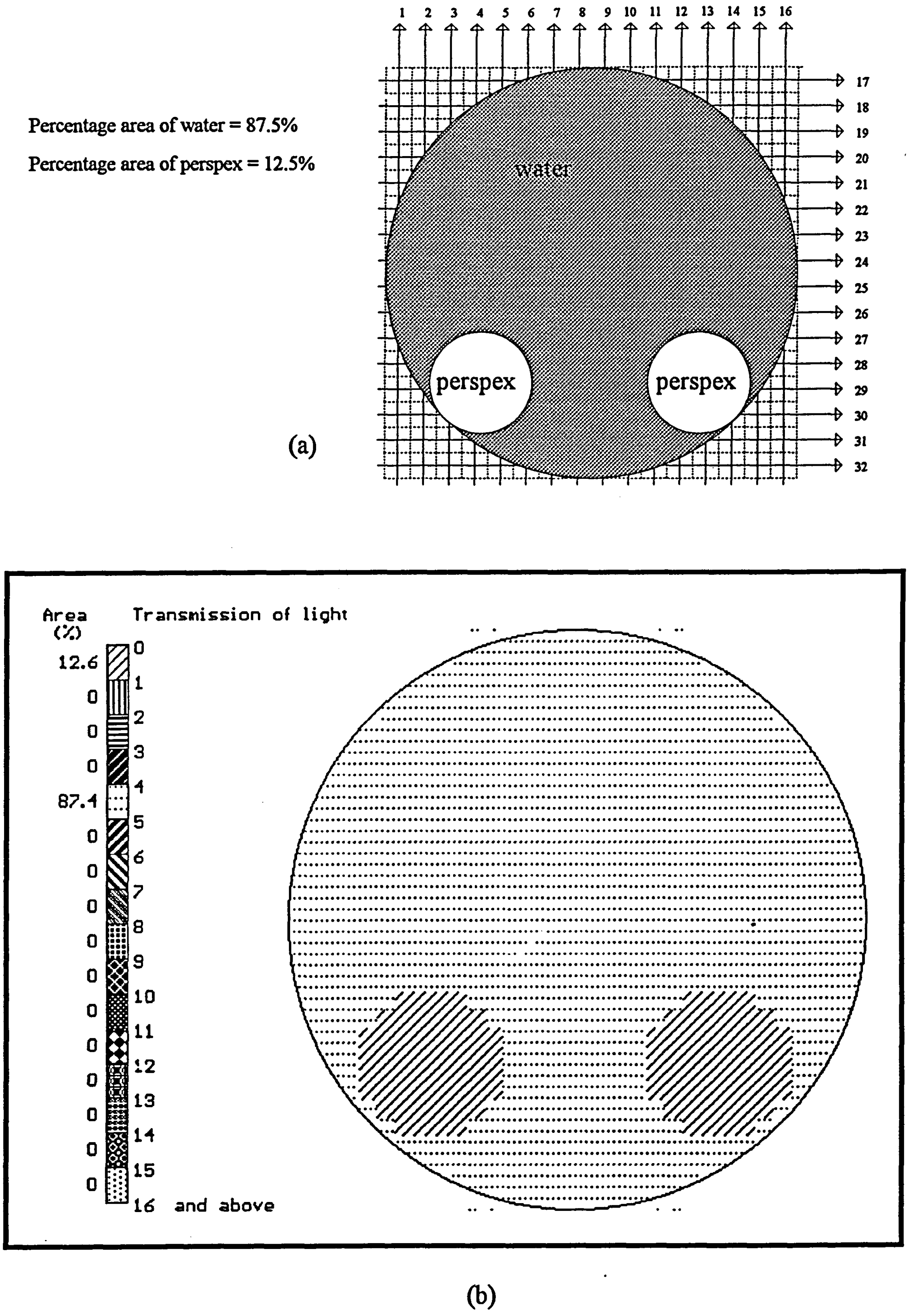

Percentage area of water = 87.5%

Percentage area of perspex = 12.5%

Figure 6.4 Reconstruction for the optical system for two 2.5 cm diameter of perspex rods placed in a 10 cm diameter cm saline filled vessel.
a) actual position b) reconstructed

Percentage area of water = 87.5%

Percentage area of perspex = 12.5%

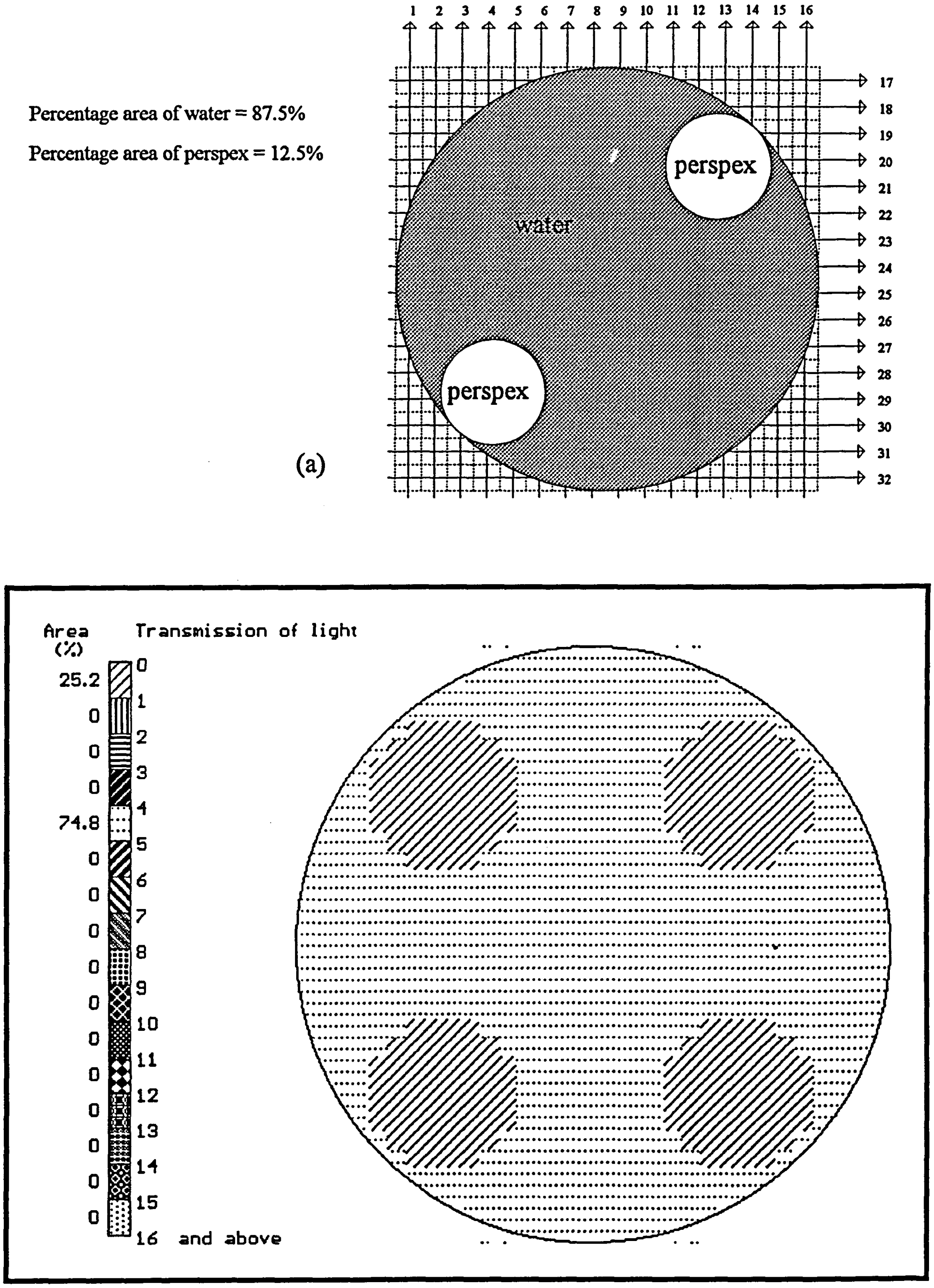

(a)

(b)

Figure 6.5 Reconstruction for the optical system for two 2.5 cm diameter of perspex rods placed in a 10 cm diameter saline filled vessel.
a) actual position b) reconstructed

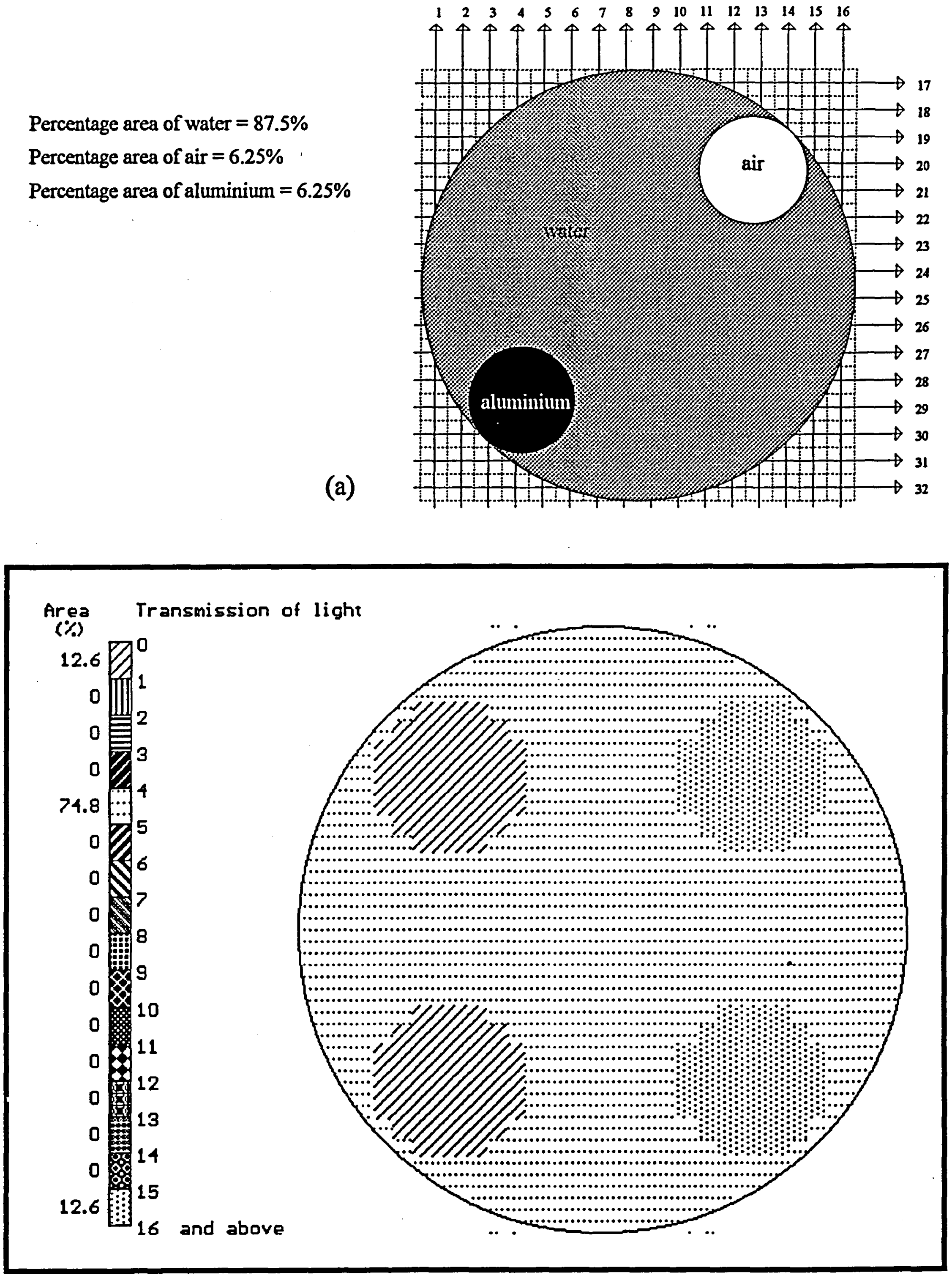

(b)

Figure 6.6 Reconstruction for the optical system for a 2.5 cm diameter of aluminium rod and a 2.5 cm diameter air bubble placed in a 10 cm diameter cm saline filled vessel.
a) actual position b) reconstructed

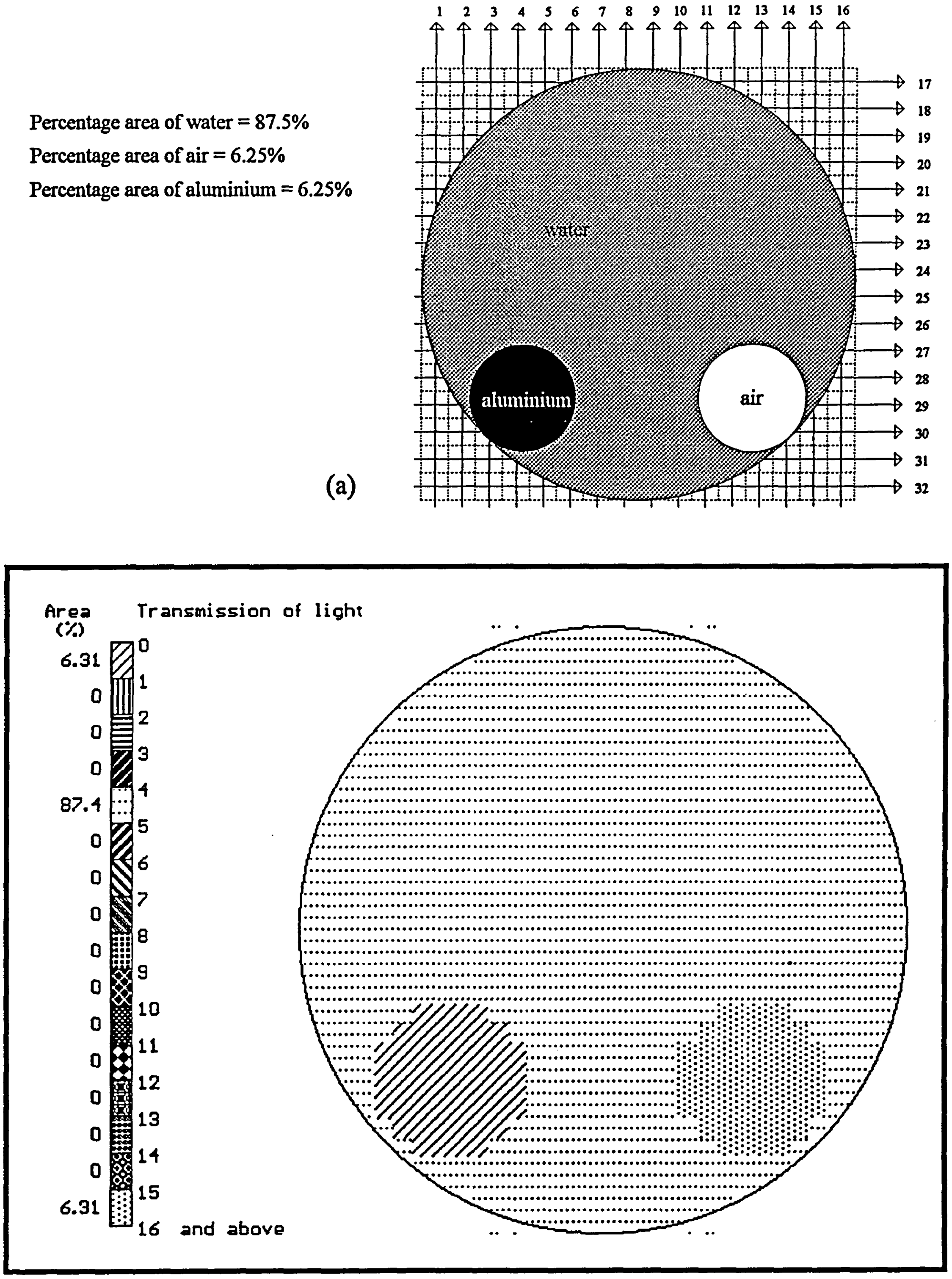
Percentage area of water = 87.5%
Percentage area of air = 6.25%
Percentage area of aluminium = 6.25%

(b)

Figure 6.7 Reconstruction for the optical system for a 2.5 cm diameter of aluminium rod and a 2.5 cm diameter air bubble placed in a 10 cm diameter cm saline filled vessel.
a) actual position b) reconstructed

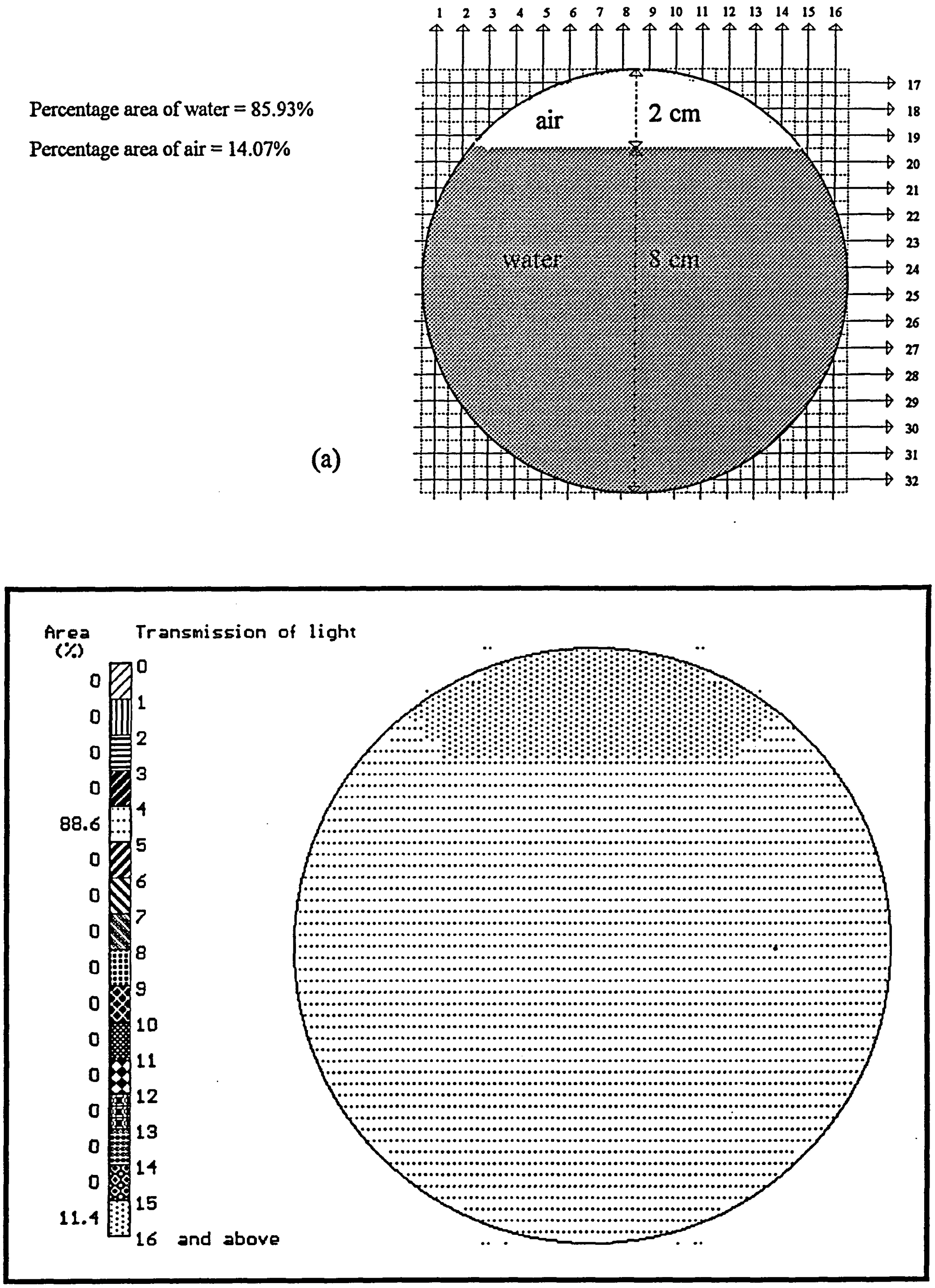

Percentage area of water = 85.93%

Percentage area of air = 14.07%

(a)

(b)

Figure 6.8 Reconstruction for the optical system for a 10 cm diameter horizontal pipe when the depth of the water is 8 cm.
a) actual position b) reconstructed

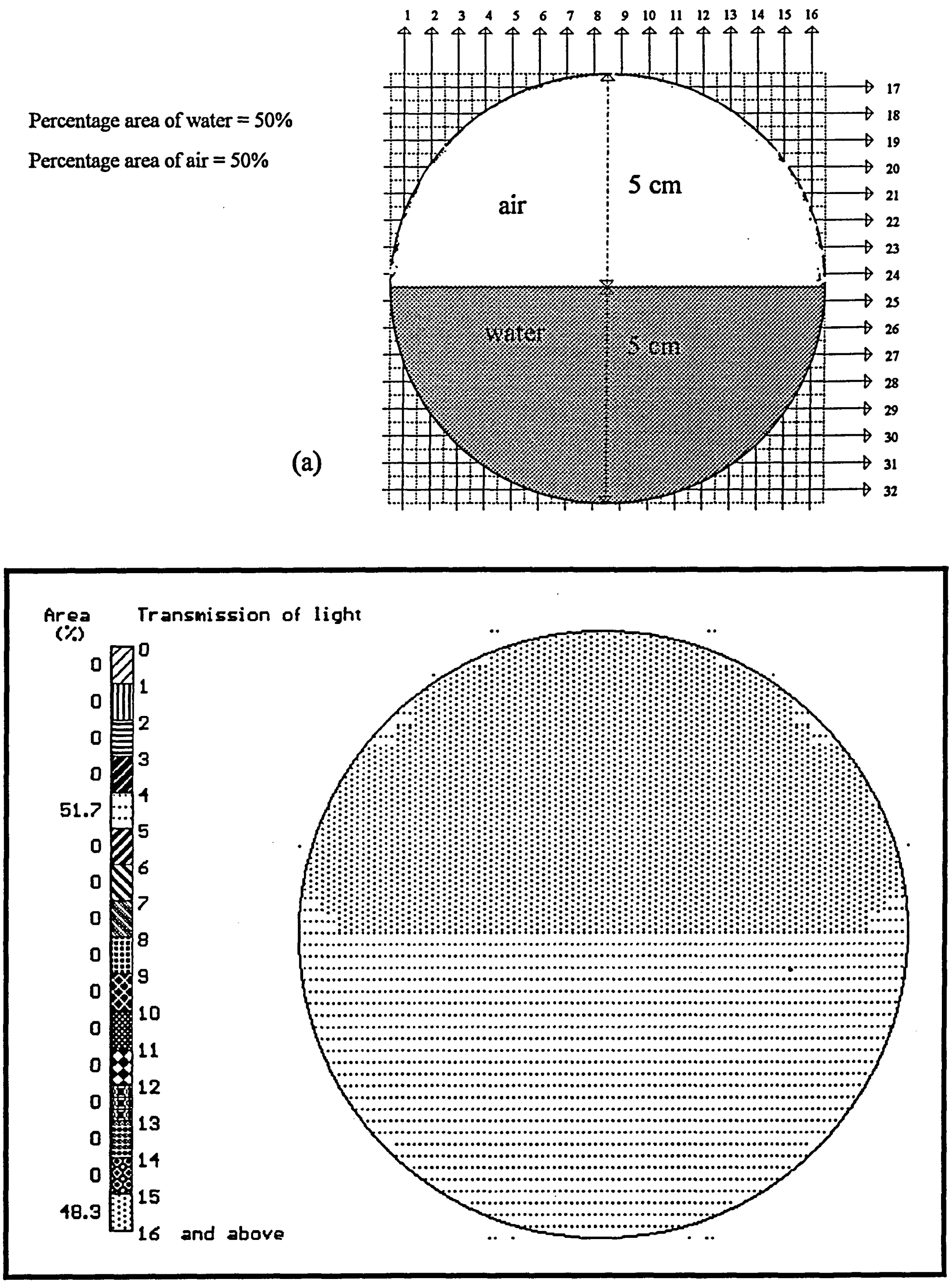

(b)

Figure 6.9 Reconstruction for the optical system for a 10 cm diameter horizontal pipe when the depth of the water is 5 cm.
a) actual position b) reconstructed

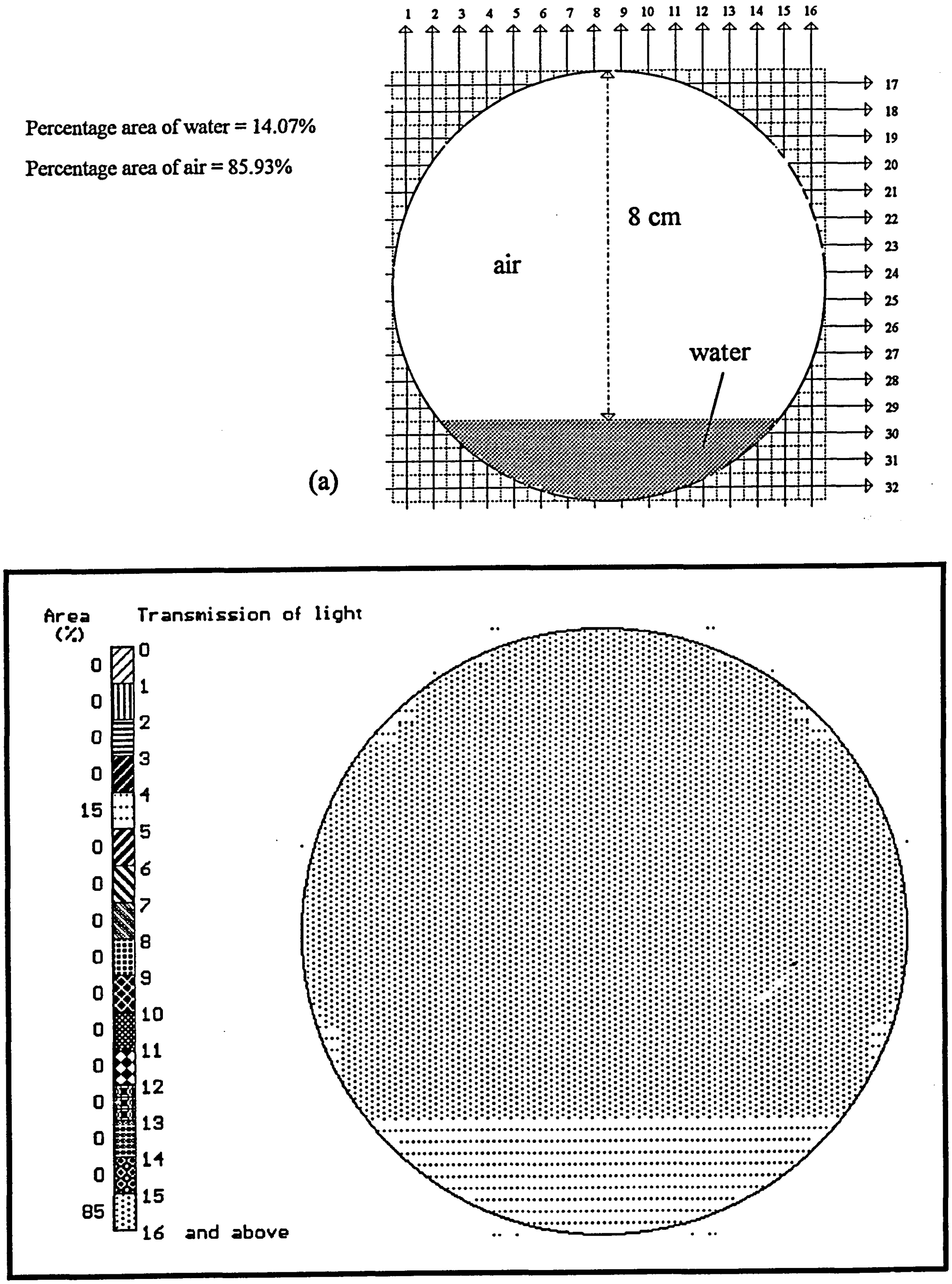

(b)

Figure 6.10 Reconstruction for the optical system for a 10 cm diameter horizontal pipe when the depth of the water is 2 cm.
a) actual position b) reconstructed

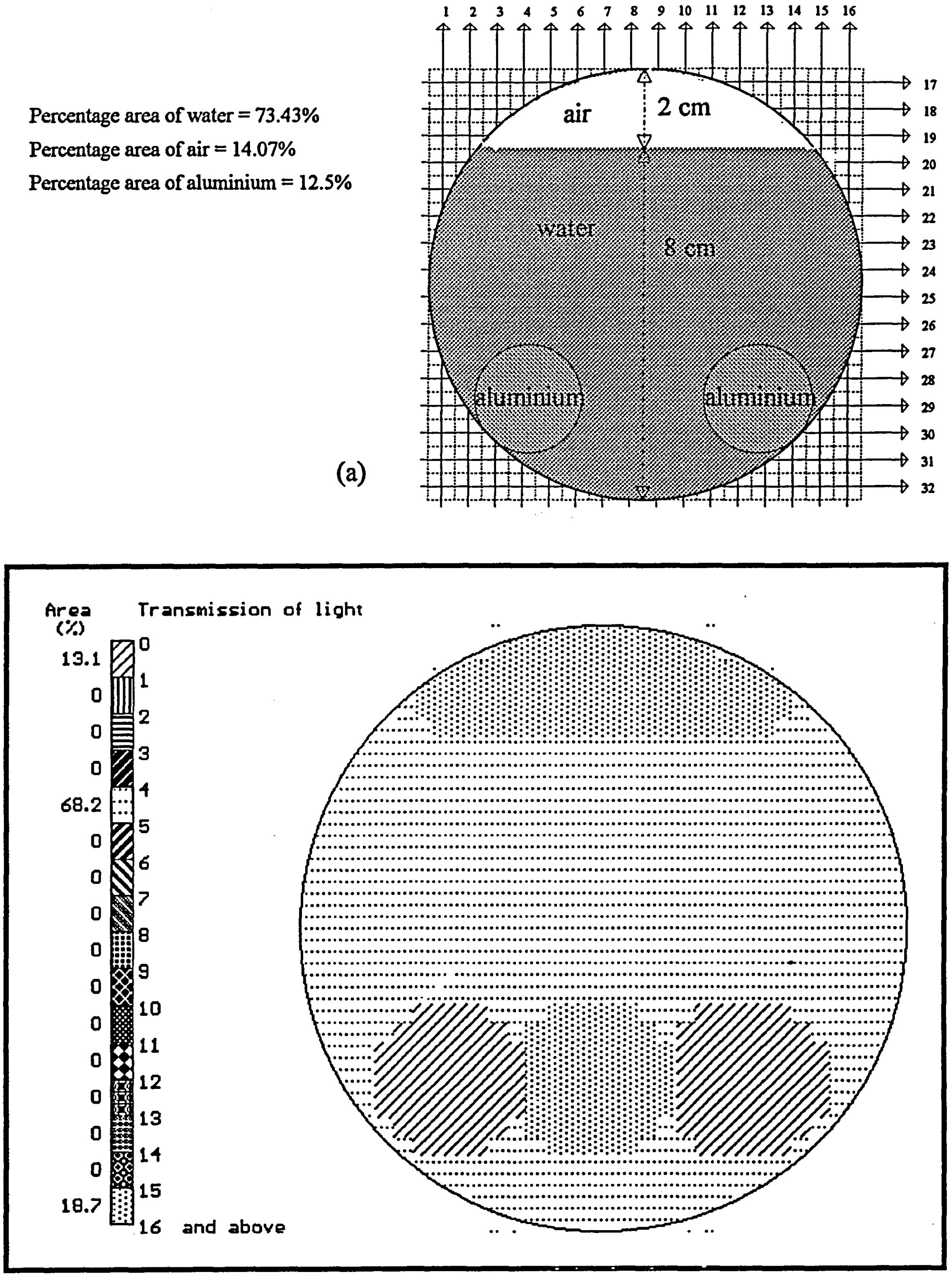

Percentage area of water = 73.43%
Percentage area of air = 14.07%
Percentage area of aluminium = 12.5%

(b)

Figure 6.11 Reconstruction for the optical system for a 10 cm diameter horizontal pipe when the depth of the water is 8 cm and two 2.5 cm diameter of aluminium rods are placed inside the pipe.
a) actual position b) reconstructed

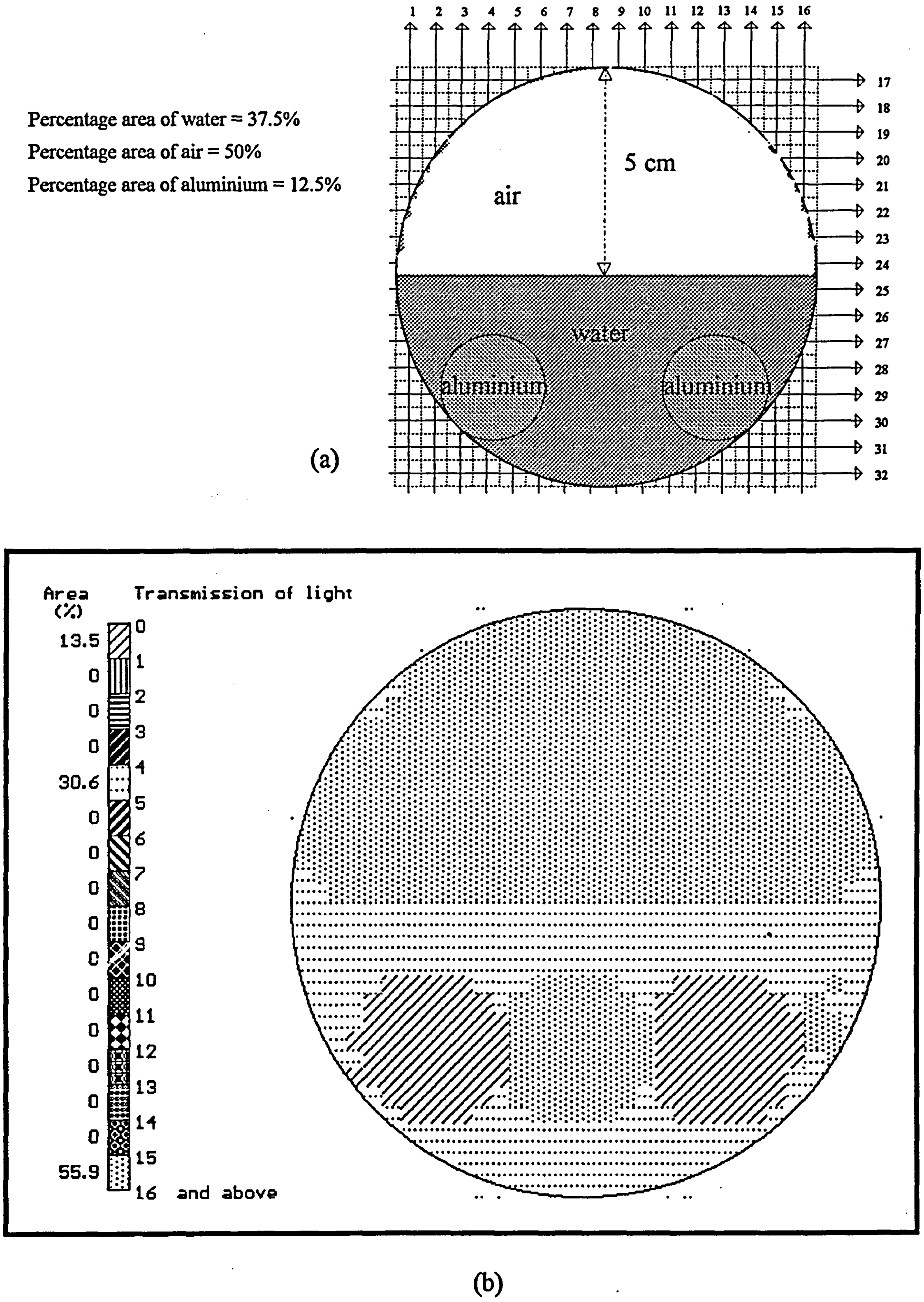

Figure 6.12 Reconstruction for the optical system for a 10 cm diameter horizontal pipe when the depth of the water is 5 cm and two 2.5 cm diameter of aluminium rods are placed inside the pipe.
a) actual position b) reconstructed

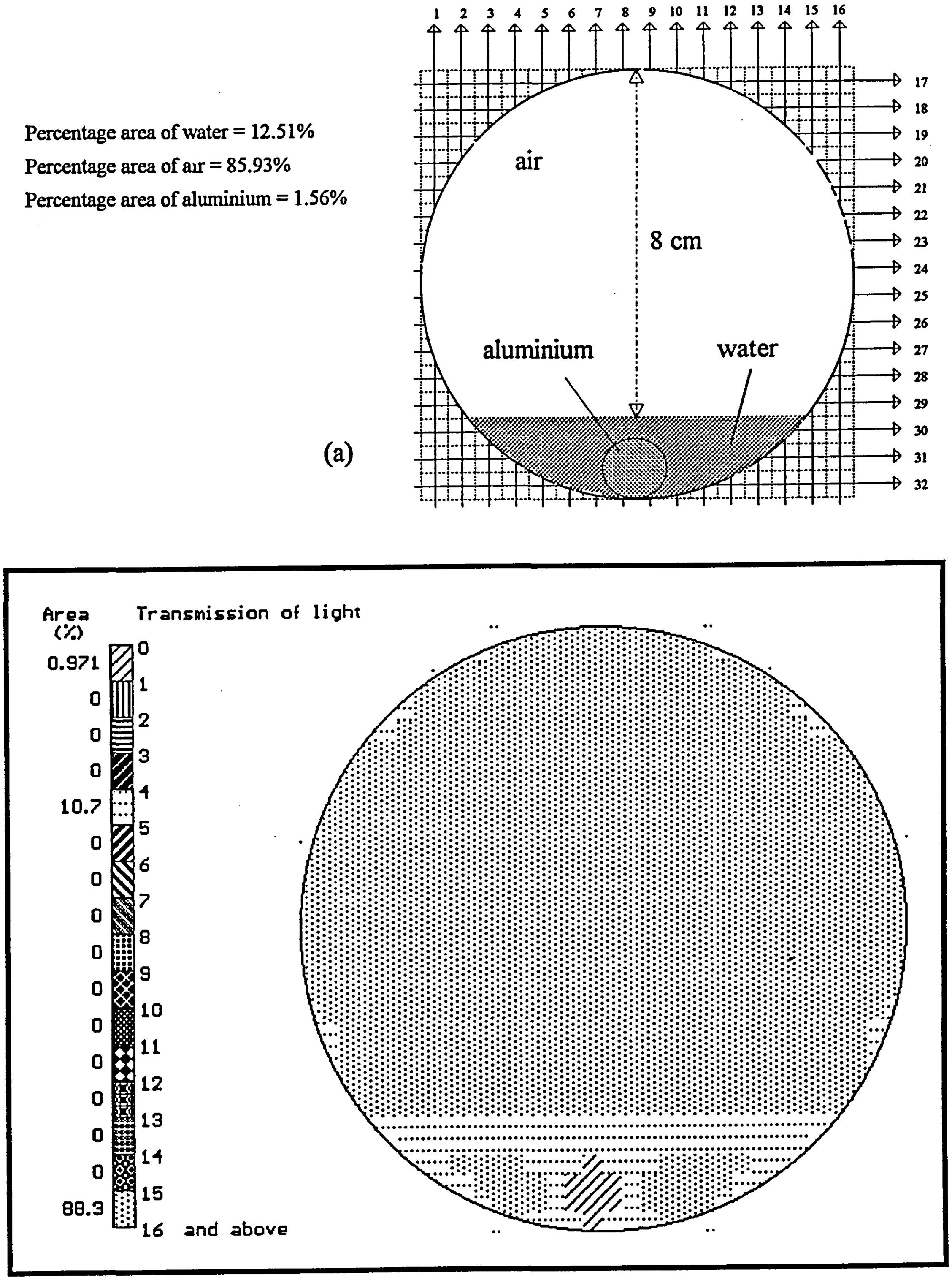

Percentage area of water = 12.51%

Percentage area of air = 85.93%

Percentage area of aluminium = 1.56%

Figure 6.13 Reconstruction for the optical system for a 10 cm diameter horizontal pipe when the depth of the water is 2 cm and 1.25 cm diameter of aluminium rod is placed inside the pipe.
a) actual position b) reconstructed

6.3 Results and discussion

The results of the simulations shown in Figures 6.1 - 6.13 are now listed and discussed.

6.3.1 With the vessel full of air (Figure 6.1) the reconstruction indicates the percentage of air 97.3% (actual 100%) and water 2.7%. The existence of water may be either because the phantom is surrounded by water or because of the post-processing of the image for display.

6.3.2 This simulation investigates the presence of an air bubble in the pipe. The measured percentage of water is 93.7% (actual 93.75%) and that of air is 6.3% (actual 6.25%).

6.3.3 This simulation investigates the presence of perspex in the pipe. The measured percentage of water is 93.7% (actual 93.75%) and for the perspex is 6.3% (actual 6.25%).

6.3.4 The modelling of two perspex rods, each having the same area as the single rod in Section 6.3.3, shows the expected doubling in area of the perspex - 12.6% (actual 12.5%). The measured percentage of water is 87.4% (actual 87.5%).

6.3.5 For this simulation, the perspex rods are placed diagonally with respect to each other in the pipe. However, this modelling of two perspex rods, each having the same area as the single rod in Section 6.3.4, does not show the expected doubling in area of the perspex - 25.2% (actual 12.5%). The large increase in percentage area of perspex is due to the aliasing mentioned in Section 5.3.5.

6.3.6 This result shows the effects of two objects, one opaque (aluminium) and the other translucent (air). The results show the area of aluminium is 12.6% (actual 6.25%), gas 12.6% (actual 6.25%) and water 74.8% (actual 87.5%). Again the doubling in percentage area of aluminium and gas which are shown in the results is due to aliasing.

6.3.7 This is similar to Section 6.3.6, except the position of the aluminium and air bubble are placed horizontally with respect to each other. This investigation shows no aliasing and accurate reconstructions aluminium 6.3% (actual 6.25%) and air 6.3% (actual 6.25%).

6.3.8 This and the following section investigations are very relevant to liquid flow in the sewer, with a layer of air above the drain liquid. The reconstructed major volume of the liquid has an area in the cross-section of 88.6% (actual 85.93%) and the air 11.4% (actual 14.07%).

6.3.9 When the liquid flow in the sewer is half full, the measured percentage of water is 51.7% (actual 50%) and gas 48.3% (actual 50%).

6.3.10 This example investigates when the quantity of the conveying liquid in the sewer is smaller than air. The reconstructed image shows the major volume of the air has an area in the cross-section of 85% (actual 85.93%) and water 15% (actual 14.07%).

6.3.11 This and the next two simulations (Sections 6.3.12 and 6.3.13) investigate the effect of conducting solid and varying water depth. With mainly water the reconstruction for Section 6.3.11 gives water 68.2% (actual 73.43%), aluminium 13.1% (actual 12.5%) and air 18.7% (actual 14.07%). The increase in percentage area of air is due to the limited number of projections for this study giving rise to aliasing of the air because the sewer is not filled with liquid. This study only used two projections.

6.3.12 There is 50% air in this simulation, but the result of the reconstruction for air is 55.9%. The results for water 30.6% (actual 37.5%) and aluminium 13.5% (actual 12.5%). Again the increase for air is due to the limited number of projections as in Section 6.3.11.

6.3.13 This simulation investigates the presence of solids when the sewer has a very low level of liquid. The water presence is reconstructed to 10.7% (actual 12.51%), aluminium rod to 1% (actual 1.56%) and air to 88.3% (actual 85.93%). Again some aliasing is present for the same reasons mentioned in Section 6.3.11.

6.3.14 Summary

The test results obtained using the phantoms with optical tomography show that the images produced by this image reconstruction method agree closely on a quantitative basis with the physical model; thus they encourage further research.

The accuracy of the optical reconstructions, neglecting the effects of aliasing due to only two projections, is much higher than for EIT reconstruction. The results of the simulations are tabulated in Table 6.2. Neglecting aliasing, the measured accuracies range from 0.1% to 0.8% for the pipe filled with water. For the sewer conditions *i.e.* a pipe not filled with water, the major phase is measured with an accuracy of 1% to 3.4%. The minor components are measured with less accuracy, where accuracy is defined as $\frac{|\text{modelled - actual}|}{\text{actual}} \times 100\%$. However, the results as a percentage of the total pipe area are only 2% to 3%. From these simulations, the results also show limitations (Figures 6.5(b), 6.6(b), 6.11(b), 6.12(b) and 6.13(b)). These limitations may be removed as improved upon by the following:

a) *Aliasing.* For two objects the resulting tomographic images may have a non-unique solution as shown in Figures 6.5(b), 6.6(b), 6.11(b), 6.12(b) and 6.13(b). This problem can be overcome if more than two projections are used. Another solution is to combine this technique with the other modality (e.g. EIT) as discussed in Chapter 7, in order to eliminate 'shadow' objects.

b) *Resolution.* The image resolution of the system is not high (1 in 824 or approximately 0.12%). The image resolution is mainly limited by the number of views (16) for each projection. Increasing the number of views (e.g. 32) for each projection will improve the image quality and accuracy.

6.4 Conclusion

The results of the optical tomography simulations show that accuracies better than 5% of full pipe may be achieved. This demonstrates the potential for imaging volume flow for sewers if combine with other modality such as EIT.

Figures	Water		Air		Aluminium		Perspex	
	Modelled	Actual	Modelled	Actual	Modelled	Actual	Modelled	Actual
6.1	2.7	0	97.3	100.0				
6.2	93.7	93.75	6.3	6.25				
6.3	93.7	93.75					6.3	6.25
6.4	87.4	87.5					12.6	12.5
6.5	74.8	87.5					25.2	12.5
6.6	74.8	87.5	12.6	6.25	12.6	6.25		
6.7	87.4	87.5	6.3	6.25	6.3	6.25		
6.8	88.6	85.93	11.4	14.07				
6.9	51.7	50.0	48.3	50.0				
6.10	15.0	14.07	85.0	85.93				
6.11	68.2	73.43	18.7	14.07	13.1	12.5		
6.12	30.6	37.5	55.9	50.0	13.5	12.5		
6.13	10.7	12.51	88.3	85.93	1.0	1.56		

Table 6.2 Analysis of accuracy for optical tomography reconstruction

7. Results from numerical simulated data for dual modality

7.1 Introduction

In this chapter the original EIT results (Chapter 5), shown in colour, and the improved optical results (Chapter 6), shown hatched, are shown superimposed. The improved optical results now agree with the physical model. The simulated test data is used by the reconstruction algorithms to produce images of the cross-section. The advantages of using dual modality compared with single modality is investigated and discussed.

7.2 Test data

To analyse the performance of the dual modality image reconstruction used in this investigation, the sequence of simulations performed on EIT (Chapter 5) and optical tomography (Chapter 6) measurements are repeated. The resulting tomographic images are shown in Figures 7.1(b) - 7.13(b). Estimates of the component concentrations determined by each modality are included and discussed in Section 7.3.

Percentage area of air = 100%

(a)

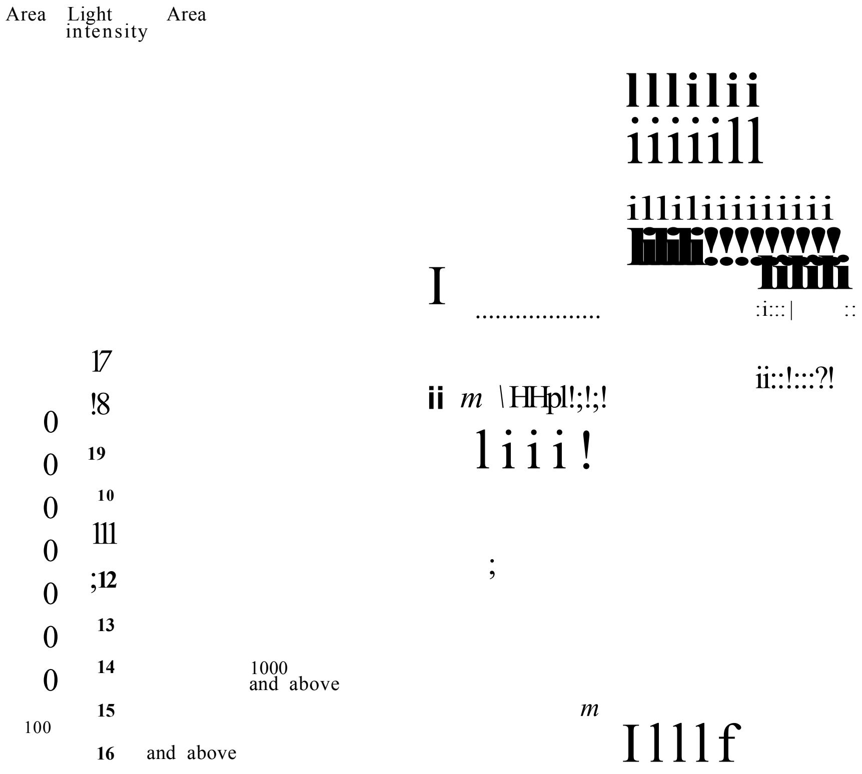

(b)

Figure 7.1 Reconstruction for the dual modality system for a 10 cm diameter vessel full of air.
a) actual position b) reconstructed

Percentage area of water = 93.75%
Percentage area of air = 6.25%

(a)

Area Light Area Resistivity
<K> intensity ***CO*** (Ohm cm)

(b)

Figure 7.2 Reconstruction for the dual modality system for a 2.5 cm diameter of air bubble (1000 Q cm) placed at the centre of a 10 cm diameter 500 Q cm saline filled vessel.
a) actual position b) reconstructed

water

Percentage area of water = 93.75%
Percentage area of perspex = 6.25%

(perspex)

(a)

Area Light intensity Area CO Resistivity (Ohm CKO

(b)

Figure 7.3 Reconstruction for the dual modality system for a 2.5 cm diameter of perspex rod (960 Q cm) placed at the centre of a 10 cm diameter 500 Q cm saline filled vessel,
a) actual position b) reconstructed

water

Percentage area of water = 87.5%
Percentage area of perspex = 12.5%

perspex perspex

Area Light intensity Area *CO* Resistivity (Ohm cm)

(b)

Figure 7.4 Reconstruction for the dual modality system for two 2.5 cm diameter of perspex rods (960 Q cm) placed in a 10 cm diameter 500 Q cm saline filled vessel.
a) actual position b) reconstructed

Percentage area of water = 87.5%
Percentage area of perspex = 12.5%

water

perspex

(a)

Area <50	Light intensity	Area <50	Resistivity <Ohm cm)
		0	
		0	
		0	
		0	
		0	
		0	
		80.6	
		0	
		1.82	
		4.37	
		3.03	
		1.82	
		1.94	
		6.43	
		and above	

(b)

Figure 7.5 Reconstruction for the dual modality system for two 2.5 cm diameter of perspex rods (960 Q cm) placed in a 10 cm diameter 500 Q cm saline filled vessel.
a) actual position b) reconstructed

Percentage area of water = 87.5%
Percentage area of air = 6.25%
Percentage area of aluminium = 6.25%

water

(a)

Area (/.> Light intensity Area <)© Resistivity (Ohm cm)

0.971

(b)

Figure 7.6 Reconstruction for the dual modality system for a 2.5 cm diameter of aluminium rod (360 Q cm) and a 2.5 cm diameter air bubble (1000 Q cm) placed in a 10 cm diameter 500 Q cm saline filled vessel,
a) actual position b) reconstructed

Percentage area of water = 87.5%
Percentage area of air = 6.25%
Percentage area of aluminium = 6.25%

water

(a)

Area C4> Light intensity Area <"D Resistivity <Dhm cm)

(b)

Figure 7.7 Reconstruction for the dual modality system for a 2.5 cm diameter of aluminium rod (360 Q cm) and a 2.5 cm diameter air bubble (1000 Q cm) placed in a 10 cm diameter 500 Q cm saline filled vessel,
a) actual position b) reconstructed

of water = 85.93%

of air = 14.07%

2 cm

air

water

8 cm

Area <50

Light intensity

Area <50

(Ohm cm)

and above

(b)

Figure 7.8 Reconstruction for the dual modality system for a 10 cm diameter horizontal pipe when the depth of the water is 8 cm.
a) actual position b) reconstructed

Percentage area of water = 50%

Percentage area of air = 50%

5 cm

5 cm

(a)

Area <5©

Light intensity

Area <5©

Resistivity <0hi» cm)

(b)

Figure 7.9 Reconstruction for the dual modality system for a 10 cm diameter horizontal pipe when the depth of the water is 5 cm.
a) actual position b) reconstructed

air

Percentage area of water = 14.07%

Percentage area of air = 85.93%

8 cm

2 cm

(a)

water

Area <%) Light intensity Area <Q Resistivity <0hm cm)

(b)

Figure 7.10 Reconstruction for the dual modality system for a 10 cm diameter horizontal pipe when the depth of the water is 2 cm.
a) actual position b) reconstructed

Percentage area of water = 73.43%

Percentage area of aluminium = 12.5%

Percentage area of air = 14.07%

air

2 cm

water

cm

aluminium

aluminium

Area CO Light intensity Area CO Resistivity (Ohm cm)

(b)

Figure 7.11 Reconstruction for the dual modality system for a 10 cm diameter horizontal pipe when the depth of the water is 8 cm and two 2.5 cm diameter of aluminium rods (360 Q cm) are placed inside the pipe,

a) actual position b) reconstructed

air

Percentage area of water = 37.5%
Percentage area of aluminium =12.5%
Percentage area of air = 50%

water

aluminium

(a)

aluminium

Area (%) Light intensity Area (%) Resistivi (Ohm cm)

(b)

Figure 7.12 Reconstruction for the dual modality system for a 10 cm diameter horizontal pipe when the depth of the water is 5 cm and two 2.5 cm diameter of aluminium rods (360 Q cm) are placed inside the pipe,
a) actual position b) reconstructed

Percentage area of water = 12.51%
Percentage area of air = 85.93%
Percentage area of aluminium = 1.56%

8 cm

aluminium

water

Area <5i> Light intensity Area CO Resistivity (Ohm cm)

0.971 y j 0.495 20

(b)

Figure 7.13 Reconstruction for the dual modality system for a 10 cm diameter horizontal pipe when the depth of the water is only 2 cm and 1.25 cm diameter of aluminium rod (360 Q cm) is placed inside the pipe,
a) actual position b) reconstructed

7.3 Results and discussion

The results from the simulations of dual modality tomography presented in Section 7.2 produce several interesting observations. The use of EIT and optical measurements together gives more information compared to the use of either EIT or optical measurements only. It is found that the reconstruction algorithm can eliminate the non-unique solutions, Figures 6.5(b), 6.6(b), 6.11(b), 6.12(b) and 6.13(b), as shown by Figures 7.5(b), 7.6(b), 7.11(b), 7.12(b) and 7.13(b). The results of the simulations shown in Figures 7.1 - 7.13 are now listed and discussed.

7.3.1 With the vessel full of air (Figure 7.1) the reconstruction indicates 100% air for both EIT and optical tomography.

7.3.2 This simulation investigates the presence of an air bubble in the pipe. The optical reconstruction gives a more accurate prediction compared to EIT. The optical reconstruction measured percentage of water is 93.7% (actual 93.75%) and that of air is 6.3% (actual 6.25%), whilst the corresponding for EIT are 86.4% and 6%.

7.3.3 This simulation investigates the presence of perspex in the pipe. Again, the optical reconstruction gives a more accurate prediction compared to EIT. The measured percentage of water is 93.7% (actual 93.75%) and for the perspex is 6.3% (actual 6.25%). The corresponding values for EIT are 86.4% and 5.3%.

7.3.4 The modelling of two perspex rods, each having the same area as the single rod in Section 7.3.3, shows the expected doubling in area of the perspex both for EIT and optical measurements. For optical the reconstruction gives 88.1%

(actual 87.5%) for water and 11.9% (actual 12.5%) for perspex compared with 80.6% and 8.3% using the EIT reconstruction.

7.3.5 For this simulation, the perspex rods are placed diagonally with respect to each other in the pipe. This modelling of two perspex rods, each having the same area as the single rod in Section 7.3.4, shows the expected doubling in area of the perspex. The effect of aliasing as mentioned in Section 6.3.5 is eliminated by combining both EIT and optical reconstructions.

7.3.6 This result shows the effects of two objects, one opaque with decreased resistivity (aluminium) and the other translucent with increased resistivity (air). Again, the aliasing (Section 6.3.6) is eliminated when combining both EIT and optical tomography measurements. For the optical reconstruction the percentage of water is 88.6% (actual 87.5%), aluminium 5.46% (actual 6.25%) and air 5.95% (actual 6.25%). The corresponding values obtained with the EIT part of the programme are 83.1%, 7.0% and 4.6%.

7.3.7 This simulation is similar to Section 7.3.6, except the position of the aluminium and air bubble are aligned horizontally with respect to each other. For the optical reconstruction the percentage of water is 88.7% (actual 87.5%), aluminium 5.34% (actual 6.25%) and air 5.95% (actual 6.25%). The corresponding values obtained with the EIT part of the programme are 83.1%, 7.0% and 4.6%. This investigation shows that in combining both EIT and optical tomography, the effect of aliasing as mentioned in Section 6.3.7 can be eliminated.

7.3.8 This investigation is very relevant to liquid flow in a sewer, with a layer of air above the drain liquid. The optical reconstruction gives water 88.6% (actual

85.93%) and air 11.4% (actual 14.07%). However, the corresponding values obtained with the EIT part of the programme are 83.7% and 7.5%. With a clear liquid the optical measurement system provides the correct result with reasonable resolution.

7.3.9 When the liquid level in the sewer is half full, the optical reconstruction gives water 51.7% and air 48.3%, but the corresponding values obtained with the EIT part of the programme are 46.1% and 41%. The ambiguity in the EIT measurement is 12.8%, though the optical is within 2%. The optical system alone is adequate for this flow combination. However, the effects of small gas bubble in a real flow system may cause aliasing and the EIT system would then be useful. See Chapter 8 for further discussion.

7.3.10 This result shows when the level of the conveying liquid in the sewer is smaller than air. The optical reconstruction gives water 27.9% (actual 14.07%) and air 72.1% (actual 85.93%), but the corresponding values obtained with the EIT part of the programme are 9.95% and 76.7%. The comments from Sections 7.3.8 and 7.3.9 apply here.

7.3.11 This and the next two simulations (Sections 7.3.12 and 7.3.13) investigate the effect of conducting solid and varying water depth on the reconstructed images. With mainly water the optical reconstruction gives water 76.6% (actual 73.43%), aluminium 11% (actual 12.5%) and air 12.4% (actual 14.07%). The corresponding values obtained with the EIT part of the programme are 69.2%, 13.6% and 7.5%. This investigation shows the main advantage in combining both EIT and optical tomography is that the effect of aliasing (as mentioned in Section 6.3.11) can be eliminated.

7.3.12 There is 50% air in this simulation, but the result obtained with optical reconstruction gives 40.5%. The corresponding value obtained with the EIT part of the programme is 45.8%. The optical reconstruction gives water 46% (actual 37.5%), aluminium 13.5% (actual 12.5%). The corresponding values obtained with the EIT part of the programme are 23.5% and 13.3%. The ambiguity in the EIT measurement is 17.2%. This result demonstrates a limitation of this combined system. The EIT system introduces an artefact (Section 5.3.12), the optical does not detect the artefact, but this may be due, as far as the optical system is concerned, to an object with the same absorption coefficient as the water. This result is improved by only using the optical system.

7.3.13 This simulation investigates the presence of solids when the sewer has a very low level of liquid. The optical reconstruction gives water 26.7% (actual 12.51%), aluminium 1% (actual 1.56%) and air 72.3% (actual 85.93%). The corresponding values obtained with the EIT part of the programme are 8.74%, 1.2% and 76.9%.

7.3.14 Summary

The test results obtained using the phantoms show that the images produced by combining both EIT and optical tomography method agree quantitatively with the physical model. From this combined simulation, the results show some improvements (Figures 7.5(b), 7.6(b), 7.11(b), 7.12(b) and 7.13(b)) compared with single modality simulations shown in Figures 6.5(b), 6.6(b), 6.11(b), 6.12(b) and 6.13(b) by eliminating aliasing in the optical system.

Figures	Water			Air			Aluminium			Perspex		
	Modelled		Act.	Modelled		Act.	Modelled		Act.	Modelled		Act.
	EIT	OT		EIT	OT		EIT	OT		EIT	OT	
7.1				100.0	100.0	100.0						
7.2	86.4	93.7	93.75	6.0	6.3	6.25						
7.3	86.4	93.7	93.75							5.34	6.3	6.25
7.4	80.6	88.1	87.5							8.3	11.9	12.5
7.5	80.6	88.1	87.5							8.4	11.9	12.5
7.6	83.1	88.6	87.5	4.6	6.0	6.25	7.0	5.5	6.25			
7.7	83.1	88.7	87.5	4.6	5.95	6.25	7.0	5.3	6.25			
7.8	83.7	88.6	85.93	7.5	11.4	14.07						
7.9	46.1	51.7	50.0	41.0	48.3	50.0						
7.10	10.0	27.9	14.07	76.7	72.1	85.93						
7.11	69.2	76.6	73.43	7.5	12.4	14.07	13.6	11.0	12.5			
7.12	23.5	46.0	37.5	45.9	40.5	50.0	13.3	13.5	12.5			
7.13	8.7	26.7	12.51	77.0	72.3	85.93	1.2	1.0	1.56			

Table 7.1 Analysis of accuracy combining both EIT and optical tomography together

From Table 7.1 it may be seen that, with three exceptions, the optical reconstructions for water are accurate to within approximately 3% or better. The three exceptions (Figures 7.10, 7.12 and 7.13) occur where two of the optical beams are close to the wall of the pipe and in air.

7.4 Conclusion

The simulation results of this project suggest that it be further investigated using an experimental system. Further experimental investigations need to be done to verify and calibrate the modelling.

8. Conclusion and suggestions for future works.

8.1 Conclusion

The specific objectives of the thesis have been met. The results show that the optical part of the system provides accuracies in the range 1 to 5% with the EIT eliminating most of the aliasing. This suggests that this dual modality tomographic imaging technique could be suitable for use in a range of process tomography situations after further development. The conclusions which can be drawn from this work are stated as follows with reference to the aims laid out in Section 1.2.

a) The work on EIT image reconstruction has focused on the MNR algorithm in order to yield quantitative information concerning the resistivity distribution across the imaging plane. This method of image reconstruction was originally developed for biomedical applications and is superior to other reconstruction methods (Yorkey et al., 1987). Unfortunately, this method is time consuming (60 - 120 seconds with a 486DX 33MHz PC).

b) The work on optical image reconstruction focused on a back-projection method based on limited data due to two projections. This method works relatively fast, compared with EIT, but unfortunately is prone to aliasing at some position of the objects. This aliasing is a result of using only two projections in this work.

c) Analysis of results from the dual modality image reconstruction have confirmed several of the predictions made in Chapter 1 covering improved accuracy (Chapter 7) and reduced aliasing (Chapter 7). Dual modality tomography has proved effective in mapping individual components in the cross-section compared to employing only a single modality system.

8.2 Contribution to the field of process tomography

This work is a part of an overall project being investigated at Sheffield Hallam University on a dual modality tomographic imaging system. Image reconstruction algorithms formed the main contribution by the author to this work. The instrumentation and data acquisition system have been undertaken by other research student (Daniels, 1995). Two types of algorithm are implemented (*i.e.* modified Newton-Raphson for EIT and back-projection for optical measurements). The combination of both tomographic images produced dual modality images which show potential for real-time reconstruction and visualisation provided that the EIT algorithm can be speeded up. Results obtained from these simulation studies indicate that further experimental investigations should be carried out, and if successful, the resulting system may be used in various process-orientated applications.

8.3 Suggestions for future work

The work described in this thesis is concerned with the combination of data from two modalities to produce tomographic images and to compare the effectiveness of the dual modality system with both single modalities, which make up the system, in detecting the same objects. The following suggestions are made in order to extend the investigation into the dual modality system.

a) The number of electrodes for EIT should be increased from 16 to 32, in order to increase the resolution of the resulting reconstructed image. Therefore, the number of independent measurements would then increase from 104 to 464 ($m = n(n-3)/2$) where n is the number of electrodes and m is the number of measurements.

b) In order to increase the resolution that can be gained from optical measurements, it is necessary to increase the number of sensors in each projection. In addition, increasing the number of projections would reduce aliasing (Sections 6.3).

c) The possibility of using optical fibres should be investigated. Optical fibres could provide high resolution (spaced at approximately 1.5 to 2 mm) and are intrinsically safe which may be very important in a sewer. Work by Abdul Rahim *et al.* (1995) suggests that optical fibres have a range of at least 300 mm.

d) The effect of multiple gas bubble size and concentration must be investigated. These may cause problems with the optical system because of limited views, but may have only a small effect on the EIT part of the system.

e) Increasing the number of transducers would mean a large quantity of information has to be handled by the reconstruction algorithm. The use of high-performance computing, such as transputers, should be investigated for speeding up the reconstruction algorithm.

f) The present work investigates component concentration within the sensing cross-section. In order to extend the system to determine volume flow rates of the solid components it is necessary to measure component velocities, etc. This possibility should be investigated using suitable instrumentation, cross-correlation and a flow rig. Specific solids or gas bubbles should be tracked in order to evaluate the possibility of implementing such a system.

g) The optical reconstruction algorithm is based on equal path length for all views. This assumption is not true for a sewer. Therefore a modified algorithm based on the one presented in Chapter 4 should be developed with path lengths relevant to a circular sewer.

h) Tests should be made with the measurement system and the software developed as this thesis using a flow rig circulating real sewage in order to evaluate the absolute feasibility of this system.

i) The suggestion outlined in (h) may be further developed to investigate the possibility of identifying specific materials from the separate and combined results of the optical and EIT measurements e.g. Aluminium is opaque but more conducting than liquid. Could the existing system be modified to suggest that the detected material is a conducting metal?

j) The present dual modality system consists of two tomograms overlaid with some integration to remove artefacts. Further investigation is required to investigate the level of integration which can be achieved with this system. Cross-correlation of the two modalities may provide useful information.

k) Improved contrast between water and non-water pixels may be obtained from the optical data by using the EIT data to identify water pixels, before doing the optical reconstruction. This information will increase the number of pixels which are known to be water. This will prevent aliasing and will enable the optical data to be used more appropriately.

l) Application of image segmentation algorithms to the reconstructed images may provide opportunities to extract specific features of the flow. Combination of the EIT and optical data, description of the flow and correlation over time may be significantly improved using segment features rather than individual pixels.

References

Abdul Rahim, R., Nordin, M. J., Horbury, N., Dickin, F. J., Green, R. G. and Naylor, B. D., 1995. A protype tomographic imaging system using optical fibres for pneumatic conveyors. *Proceeding International Conference on Advances in Strategic Technologies*, June 95, UKM, Malaysia.

Abdullah, M. Z. *et al.*, 1992. Quantitative algorithm and computer architecture for real-time image reconstruction in process tomography. *Proceeding ECAPT 92, Process Tomography: A Strategy for industrial exploitation, European Concerted Action on Process Tomography*, March 92, Manchester, pp 144-157.

Artola, J. and Dell, J., 1993. The application of digital signal processors (DSP) in electrical tomography. *Proceeding ECAPT 93, Process Tomography: A Strategy for industrial exploitation - 2, European Concerted Action on Process Tomography*, March 93, Germany, pp 139-142.

Barber, D. C., Brown, B. H. and Freeston, I. L., 1983. Imaging spatial distributions of resistivity using applied potential tomography. *Elec. Letters*, Vol. 9, pp 933-935.

Barber, D. C. and Brown, B. H., 1985. Recent developments in applied potential tomography. *Proceeding 9th Conference Information Processing in Medical Imaging*, Washington, D. C., pp 106-121.

Beyer, R. T. and Fletcher, R., 1969. *Physical ultrasonics*, New York, Academic Press.

Bhat, S., 1990. Clinical applications, *Electrical Impedance Tomography* ed. Webster, J. G., (Adam-Hilger, Bristol).

Booton, R. C., 1992. *Computational Methods for Electromagnetics and Microwaves*, John Wiley and Sons.

Breckon, W. R. and Pidcock, M. K., 1988. Data errors and reconstruction algorithms in electrical impedance tomography. *Clin. Phys. Physiol. Meas.*, Vol. 9, Suppl. A, pp 105-109.

Brown, B. H., 1983. Tissue impedance method. *Imaging with non-ionizing radiation*, Ed: Jackson, D. F., Surrey University Press, pp 85-110.

Cady, E. B., 1990. *Clinical magnetic resonance spectroscopy.* Plenum Press, New York.

Carstensen, E. L., *et al.*, 1981. Finite amplitude effects on the thresholds for lesion production in tissues by unfocused ultrasound, *J. Acoust. Soc. Am.*, Vol. 70, No. 2, pp 302-309.

Cheney, M. and Isaacson, D., 1991. An overview of inversion algorithms for impedance imaging. *American Mathematical Society*, Vol. 122, pp 29-39.

Cook, J. and Dickin, F., 1993. Real-time quantitative tomographic image reconstruction. *Proceeding ECAPT 93, Process Tomography: A Strategy for industrial exploitation - 2, European Concerted Action on Process Tomography,* March 93, Germany, pp 131-134.

Crecraft, D. I., 1983. Ultrasonic instrumentation: principles, methods and applications. *J. Phys. E: Sci. Instrum.*, Vol. 16, pp 181-189.

Daniels, A. R., 1995. *An investigation into the use of dual modality tomography for the measurement of constituent volumes in multi component flows.* PhD thesis, Sheffield Hallam University.

Daniels, A. R., Basarab-Horwath, I., Dickin, F. J., and Green, R. G., 1993a. Initial findings on an EIT imaging system for sewers. *Proceeding ECAPT 93, Process Tomography: A Strategy for industrial exploitation - 2, European Concerted Action on Process Tomography,* March 93, Germany, pp 101-104.

Daniels, A. R., Basarab-Horwath, I., Dickin, F. J., and Green, R. G., 1993b. Initial developments of an optical matrix imaging system for sewers. *Proceeding ECAPT 93, Process Tomography: A Strategy for industrial exploitation - 2, European Concerted Action on Process Tomography,* March 93, Germany, pp 105-108.

Dickin, F. J., *et al.*, 1991. Tomographic imaging of industrial process equipment using electrical impedance sensors. *Proceeding V Conference Sensors and their applications*, Edinburgh, Scotland, September 1991, pp 215-220.

Dickin, F. J., *et al.*, 1992a. Tomographic imaging of industrial process equipment: techniques and applications. *IEE Proceedings-G*, Vol. 139, No. 1, pp 72-82.

Dickin, F. J., *et al.*, 1992b. Tomography for improving the design and control of particulate processing systems. *KONA - Powder and Particle,* 10, pp 4-14.

Dines, K. A. and Lytle, R. J., 1981. Analysis of electrical conductivity imaging, *Geophysics*, Vol. 46(7), pp 1025-1036.

Dugdale, W. P., 1994. *An optical instrumentation system for the imaging of two component flow.* PhD thesis, Bolton Institute.

Dugdale, P., Green, R. G., Hartley, A. J., Jackson, R. G., and Landauro, J., 1992. Optical sensors for process tomography, *Proceeding ECAPT 92, Process Tomography: A Strategy for industrial exploitation, European Concerted Action on Process Tomography*, March 92, Manchester.

Eyuboglu, B. M. and Brown, B. H., 1988. Methods of cardiac gating applied potential tomography, *Clin. Phys. Physiol. Meas.*, Vol. 9, Supp A, pp 43-48.

Fasching, G. E. and Smith, N. S., 1991. A capacitive system for three-dimensional imaging of fluidized beds, *Rev. Sci. Instrum.*, Vol. 62, pp 2243-2251.

Gisser, D. G., *et. al.*, 1987. Current topics in impedance imaging, *Clin. Phys. Physiol. Meas.*, Vol. 8, Supp A, pp 33-46.

Griffiths, H. and Ahmed, A., 1987. A dual frequency applied potential tomography technique: computer simulations, *Clin. Phys. Physiol. Meas.*, Vol. 8, Supp A, pp 103-108.

Hartley, A. J., Green, R. G., Dugdale, P. and Laudauro, J., 1991. Tomographic imaging in industrial process equipment using optical sensor arrays, *Proceeding Institute of Physics Fifth Conference*, 22-25 September, Edinburgh.

Herman, G. T., 1980. *Image reconstruction from projections: the fundamentals of computerized tomography*, Academic Press, New York.

Huang, S. M., *et al.*, 1992. Design of sensor electronics for electrical capacitance tomography, *IEE Proc.-G*, Vol. 139, pp 83-88.

Ider, Y. Z., Gencer, N. G., Atalar, E. and Tosun, H., 1990. Electrical impedance tomograph of translationally uniform cylindrical objects with general cross sectional boundaries, *IEEE Transaction Medical Imaging*, Vol. 9, No. 1, pp 49-59.

Isaksen, Ø., 1994. *A novel approach to reconstruction of process tomography data*, DSc Thesis, University of Bergen, Norway.

Isaksen, Ø and Nordtveat, J. E., 1992. A new reconstruction algorithm for use in capacitance based process tomography, *Proceeding International Conference on the Electronic Measurement and Instrumentation*, October 1992, China.

Jaffe, C. C., 1984. *Vascular and Doppler ultrasound*, Churchill Livingstone.

Jossinet, J., *et al.*, 1988. A hardware design for imaging the electrical impedance of the breast, *Clin. Phys. Physiol. Meas.*, Vol. 9, Supp A, pp 25-28.

Kim, Y., Webster, J. G. and Tompkins, W. J., 1983. Electrical impedance imaging of the thorax, *J. Microwave Power*, Vol. 18, pp 245-257.

Kremkau, F. W., 1990. *Doppler ultrasound: principles and instruments*, Saunders.

Lehmann, J. F., *et al.*, 1967. Therapeutic temperature distribution produced by ultrasound as modified by dosage and volume of tissue exposed, *Arch. Phys. Med.*, Vol. 48, No. 12, pp 662-666.

Lin, J. T., Jones, O. C. and Ovacik, L., 1991. Electrical impedance imaging of two-phase flows, *Chem. Engng. Comm.*

McArdle, F. J., *et al.*, 1988. An assessment of dynamic images by applied potential tomography for monitoring pulmonary perfusion, *Clin. Phys. Physiol. Meas.*, Vol. 9, Supp A, pp 87-91.

McKee, S. L., Williams, R. A. and Boxman, A., 1994. Development of solid-liquid mixing models using tomographic techniques, *Proceeding ECAPT 94, Process Tomography: A Strategy for industrial exploitation, European Concerted Action on Process Tomography*, Portugal, pp 342-353.

Moesner, L. N. and Anderson, O. T., 1989. A circular finite-element model reconstruction in electrical impedance tomography, *Proceeding IEEE 11th Ann. Conf. of the Engng. in Med. & Bio. Soc.*, pp 446-447.

Muir, T. G. and Carstensen, E. L., 1980. Prediction of non-linear acoustic effects at biomedical frequencies and intensities, *Ultrasound Med. Biol.*, Vol. 6, pp 345-357.

Murai, T. and Kagawa, Y., 1985. Electrical impedance computed tomography based on a finite element model, *IEEE Trans. Biomed. Eng.*, Vol. BME-32(3), pp 177-184.

Parker, D. J., *et. al.*, 1992. Process engineering studies using positron-based imaging techniques, *Proceeding ECAPT 92, Process Tomography: A Strategy for industrial exploitation, European Concerted Action on Process Tomography*, March 92, Manchester.

Pinkard, D., 1990. An investigation into applying ultrasonic techniques to gross solids monitoring in combined sewer outflows, *Water Research Council Report: UM1171*, Nov., 1990.

Pykett, I. L., 1982. NMR imaging in medicine, *Scientific American*, Vol. 246, No. 5, pp 54-64.

Saeed, N., Browne, M. A., Green, R. G., and Martin, P., 1988. Two component flow regime identification and imaging with optical sensors, *Proceeding IMEKO XI*, Houston, Texas, pp 16-21.

Samakato, K., *et al.*, 1987. Some physical results from impedance camera, *Clin. Phys. Physiol. Meas.*, Vol. 8, Supp A, pp 71-76.

Seagar, A. D., Barber, D. C., and Brown, B. H., 1987. Electrical impedance imaging, *Proceeding Inst Elect Eng.*, Vol. 134, pt A, No. 2, pp 201-210.

Silvester, P. P. and Ferrari, R. L., 1990. *Finite Elements for Electrical Engineers*, Cambridge University Press.

Simon, G., 1975. *X-ray diagnosis for clinical students.* Butterworths, England.

Stasa, F. L., 1985. *Applied finite element analysis for engineers*, CBS Publishing Japan Ltd.

Wang, M., Dickin, F. J., and Beck, M. S., 1992. Improved electrical impedance tomography data collection system and measurement protocols, *Proceeding ECAPT 92, Process Tomography: A Strategy for industrial exploitation, European Concerted Action on Process Tomography*, March 92, Manchester.

Webster, J. G., 1990. *Electrical Impedance Tomography*, Adam Hilger.

Wells, P. N. T., 1977. *Biomedical Ultrasonics*, Academic Press, London.

Wexler, A., Fry, B. and Newman, M. R., 1985. Impedance-computed tomography algorithm and system, *Appl. Optics*, Vol. 24(23), pp 3985-3992.

Woo, E. J., Hua, P., Webster, J. G. and Tompkins, W. J., 1992. Measuring lung resistivity using electrical impedance tomography, *IEEE Trans. Biomed. Engng*, Vol. BME-39(7), pp 756-760.

World Health Organization (WHO), 1982. *Environmental health criteria 22: Ultrasound*, Geneva.

Xie, C. G., *et al.*, 1992. Electrical capacitance tomography for flow imaging: system model for development of image reconstruction algorithms and design of primary sensors, *IEE Proc.-G*, Vol. 139, pp 89-97.

Xie, C. G., *et al.*, 1994. Electrical tomography techniques for process engineering applications, *Proceeding ECAPT 94, Process Tomography: A Strategy for industrial exploitation, European Concerted Action on Process Tomography*, Portugal, pp 25-32.

Xu, L. A., Green, R. G., Plaskowski, A. and Beck, M. S., 1988. The pulsed ultrasonic cross-correlation flowmeter for two-phase flow measurement, *Journal of Physics, E: Sci. Instrum*, Vol. 21, pp 406-414.

Yorkey, T. J., 1986. *A quantitative comparison of the reconstruction algorithms used in electrical impedance tomography*, PhD thesis, Dept. Elec. Comp. Engng, Univ. of Wisconsin, USA.

Yorkey, T. J., *et al.*, 1987. Comparing reconstruction algorithms for electrical impedance tomography, *IEEE Transactions on Biomedical Engineering*, Vol. BME-34, No. 11, pp 843-852.

Yorkey, T. J., 1990. Electrical impedance tomography with piecewise polynomial conductivities, *Journal Comp. Phys*, Vol. 91(2), pp 344-360.

Yorkey, T. J., Webster, J. G., and Tompkins, W. J., 1990. Comparing reconstruction algorithms for electrical impedance tomography, *IEEE Transactions on Biomedical Engineering*, Vol. 9, No. 1, pp 49-59.

Zienkiewicz, O. C. and Cheung, Y. K., 1965. Finite elements in the solution of field problems, *The Engineer*, pp 507-510.

Appendix A Light intensity modelling

Receiver	d_w (path length in water)	d_a (path length in air)	d_w (path length in water)	voltage (V)	bit representation
R1	10.0			1.17287	64
R2	10.0			1.17287	64
R3	10.0			1.17287	64
R4	10.0			1.17287	64
R5	10.0			1.17287	64
R6	10.0			1.17287	64
R7	4.0625	1.875	4.0625	1.53931	80
R8	3.75	2.5	3.75	1.68532	80
R9	3.75	2.5	3.75	1.68532	80
R10	4.0625	1.875	4.0625	1.53931	80
R11	10.0			1.17287	64
R12	10.0			1.17287	64
R13	10.0			1.17287	64
R14	10.0			1.17287	64
R15	10.0			1.17287	64
R16	10.0			1.17287	64
R17	10.0			1.17287	64
R18	10.0			1.17287	64
R19	10.0			1.17287	64
R20	10.0			1.17287	64
R21	10.0			1.17287	64
R22	10.0			1.17287	64
R23	4.0625	1.875	4.0625	1.53931	80
R24	3.75	2.5	3.75	1.68532	80
R25	3.75	2.5	3.75	1.68532	80
R26	4.0625	1.875	4.0625	1.53931	80
R27	10.0			1.17287	64
R28	10.0			1.17287	64
R29	10.0			1.17287	64
R30	10.0			1.17287	64
R31	10.0			1.17287	64
R32	10.0			1.17287	64

Table A1 Light intensity modelling for input to optical system for a 2.5 cm diameter of air bubble placed at the centre of a 10 cm diameter saline filled vessel.

Receiver	d_w (path length in water)	d_p (path length in perspex)	d_w (path length in water)	voltage (V)	bit representation
R1	10.0			1.17287	64
R2	10.0			1.17287	64
R3	10.0			1.17287	64
R4	10.0			1.17287	64
R5	10.0			1.17287	64
R6	10.0			1.17287	64
R7	4.0625	1.875	4.0625	1.0619	48
R8	3.75	2.5	3.75	1.0273	48
R9	3.75	2.5	3.75	1.0273	48
R10	4.0625	1.875	4.0625	1.0619	48
R11	10.0			1.17287	64
R12	10.0			1.17287	64
R13	10.0			1.17287	64
R14	10.0			1.17287	64
R15	10.0			1.17287	64
R16	10.0			1.17287	64
R17	10.0			1.17287	64
R18	10.0			1.17287	64
R19	10.0			1.17287	64
R20	10.0			1.17287	64
R21	10.0			1.17287	64
R22	10.0			1.17287	64
R23	4.0625	1.875	4.0625	1.0619	48
R24	3.75	2.5	3.75	1.0273	48
R25	3.75	2.5	3.75	1.0273	48
R26	4.0625	1.875	4.0625	1.0619	48
R27	10.0			1.17287	64
R28	10.0			1.17287	64
R29	10.0			1.17287	64
R30	10.0			1.17287	64
R31	10.0			1.17287	64
R32	10.0			1.17287	64

Table A2 Light intensity modelling for input to optical system for a 2.5 cm diameter of perspex rod placed at the centre of a 10 cm diameter saline filled vessel.

Receiver	d_w (path length in water)	d_p (path length in perspex)	d_w (path length in water)	voltage (V)	bit representation
R1	10.0			1.17287	64
R2	10.0			1.17287	64
R3	4.0625	1.875	4.0625	1.0619	48
R4	3.75	2.5	3.75	1.0273	48
R5	3.75	2.5	3.75	1.0273	48
R6	4.0625	1.875	4.0625	1.0619	48
R7	10.0			1.17287	64
R8	10.0			1.17287	64
R9	10.0			1.17287	64
R10	10.0			1.17287	64
R11	4.0625	1.875	4.0625	1.0619	48
R12	3.75	2.5	3.75	1.0273	48
R13	3.75	2.5	3.75	1.0273	48
R14	4.0625	1.875	4.0625	1.0619	48
R15	10.0			1.17287	64
R16	10.0			1.17287	64
R17	10.0			1.17287	64
R18	10.0			1.17287	64
R19	10.0			1.17287	64
R20	10.0			1.17287	64
R21	10.0			1.17287	64
R22	10.0			1.17287	64
R23	10.0			1.17287	64
R24	10.0			1.17287	64
R25	10.0			1.17287	64
R26	10.0			1.17287	64
R27	5.0	2.5+2.5		0.8999	48
R28	5.0	2.5+2.5		0.8999	48
R29	5.0	2.5+2.5		0.8999	48
R30	5.0	2.5+2.5		0.8999	48
R31	10.0			1.17287	64
R32	10.0			1.17287	64

Table A3 Light intensity modelling for input to optical system for two 2.5 cm diameter of perspex rods placed in a 10 cm diameter saline filled vessel.

Receiver	d_w (path length in water)	d_p (path length in perspex)	d_w (path length in water)	voltage (V)	bit representation
R1	10.0			1.17287	64
R2	10.0			1.17287	64
R3	4.0625	1.875	4.0625	1.0619	48
R4	3.75	2.5	3.75	1.0273	48
R5	3.75	2.5	3.75	1.0273	48
R6	4.0625	1.875	4.0625	1.0619	48
R7	10.0			1.17287	64
R8	10.0			1.17287	64
R9	10.0			1.17287	64
R10	10.0			1.17287	64
R11	4.0625	1.875	4.0625	1.0619	48
R12	3.75	2.5	3.75	1.0273	48
R13	3.75	2.5	3.75	1.0273	48
R14	4.0625	1.875	4.0625	1.0619	48
R15	10.0			1.17287	64
R16	10.0			1.17287	64
R17	10.0			1.17287	64
R18	10.0			1.17287	64
R19	4.0625	1.875	4.0625	1.0619	48
R20	3.75	2.5	3.75	1.0273	48
R21	3.75	2.5	3.75	1.0273	48
R22	4.0625	1.875	4.0625	1.0619	48
R23	10.0			1.17287	64
R24	10.0			1.17287	64
R25	10.0			1.17287	64
R26	10.0			1.17287	64
R27	4.0625	1.875	4.0625	1.0619	48
R28	3.75	2.5	3.75	1.0273	48
R29	3.75	2.5	3.75	1.0273	48
R30	4.0625	1.875	4.0625	1.0619	48
R31	10.0			1.17287	64
R32	10.0			1.17287	64

Table A4 Light intensity modelling for input to optical system for two 2.5 cm diameter of perspex rods placed in a 10 cm diameter saline filled vessel.

Receiver	d_w (path length in water)	d_{al} (path length in aluminium)	d_a (path length in air)	voltage (V)	bit representation
R1	10.0			1.17287	64
R2	10.0			1.17287	64
R3	8.125	1.875			0
R4	7.5	2.5			0
R5	7.5	2.5			0
R6	8.125	1.875			0
R7	10.0			1.17287	64
R8	10.0			1.17287	64
R9	10.0			1.17287	64
R10	10.0			1.17287	64
R11	8.125		1.875	1.53931	80
R12	7.5		2.5	1.68532	80
R13	7.5		2.5	1.68532	80
R14	8.125		1.875	1.53931	80
R15	10.0			1.17287	64
R16	10.0			1.17287	64
R17	10.0			1.17287	64
R18	10.0			1.17287	64
R19	8.125		1.875	1.53931	80
R20	7.5		2.5	1.68532	80
R21	7.5		2.5	1.68532	80
R22	8.125		1.875	1.53931	80
R23	10.0			1.17287	64
R24	10.0			1.17287	64
R25	10.0			1.17287	64
R26	10.0			1.17287	64
R27	8.125	1.875			0
R28	7.5	2.5			0
R29	7.5	2.5			0
R30	8.125	1.875			0
R31	10.0			1.17287	64
R32	10.0			1.17287	64

Table A5 Light intensity modelling for input to optical system for a 2.5 cm diameter of aluminium rod and a 2.5 cm diameter air bubble placed in a 10 cm diameter saline filled vessel.

Receiver	d_w (path length in water)	d_{al} (path length in aluminium)	d_a (path length in air)	voltage (V)	bit representation
R1	10.0			1.17287	64
R2	10.0			1.17287	64
R3	8.125	1.875			0
R4	7.5	2.5			0
R5	7.5	2.5			0
R6	8.125	1.875			0
R7	10.0			1.17287	64
R8	10.0			1.17287	64
R9	10.0			1.17287	64
R10	10.0			1.17287	64
R11	8.125		1.875	1.53931	80
R12	7.5		2.5	1.68532	80
R13	7.5		2.5	1.68532	80
R14	8.125		1.875	1.53931	80
R15	10.0			1.17287	64
R16	10.0			1.17287	64
R17	10.0			1.17287	64
R18	10.0			1.17287	64
R19	10.0			1.53931	64
R20	10.0			1.68532	64
R21	10.0			1.68532	64
R22	10.0			1.53931	64
R23	10.0			1.17287	64
R24	10.0			1.17287	64
R25	10.0			1.17287	64
R26	10.0			1.17287	64
R27	6.25	1.875	1.875		0
R28	5.0	2.5	2.5		0
R29	5.0	2.5	2.5		0
R30	6.25	1.875	1.875		0
R31	10.0			1.17287	64
R32	10.0			1.17287	64

Table A6 Light intensity modelling for input to optical system for a 2.5 cm diameter of aluminium rod and a 2.5 cm diameter air bubble placed in a 10 cm diameter saline filled vessel.

Receiver	d_w (path length in water)	d_a (path length in air)	d_w (path length in water)	voltage (V)	bit representation
R1	10.0			1.17287	64
R2	10.0			1.17287	64
R3	9.375	0.625		1.28413	64
R4	8.75	1.25		1.40594	80
R5	8.75	1.25		1.40594	80
R6	8.125	1.875		1.53931	80
R7	8.125	1.875		1.53931	80
R8	8.125	1.875		1.53931	80
R9	8.125	1.875		1.53931	80
R10	8.125	1.875		1.53931	80
R11	8.125	1.875		1.53931	80
R12	8.75	1.25		1.40594	80
R13	8.75	1.25		1.40594	80
R14	9.375	0.625		1.28413	64
R15	10.0			1.17287	64
R16	10.0			1.17287	64
R17	6.56	3.44		1.9314	96
R18	4.38	5.62		2.6495	128
R19	2.82	7.18		3.3219	176
R20	10.0			1.17287	64
R21	10.0			1.17287	64
R22	10.0			1.17287	64
R23	10.0			1.17287	64
R24	10.0			1.17287	64
R25	10.0			1.17287	64
R26	10.0			1.17287	64
R27	10.0			1.17287	64
R28	10.0			1.17287	64
R29	10.0			1.17287	64
R30	10.0			1.17287	64
R31	10.0			1.17287	64
R32	10.0			1.17287	64

Table A7 Light intensity modelling for input to the optical system for a 10 cm diameter horizontal pipe when the depth of the water is 8 cm.

Receiver	d_w (path length in water)	d_a (path length in air)	d_w (path length in water)	voltage (V)	bit representation
R1	5.0	1.5625	3.4375	1.4711	80
R2	5.0	2.8125	2.1875	1.76345	96
R3	5.0	3.75	1.25	2.02022	96
R4	5.0	4.0625	0.9375	2.11387	112
R5	5.0	4.375	0.625	2.21186	112
R6	5.0	4.6875	0.3125	2.31439	112
R7	5.0	5.0		2.42167	128
R8	5.0	5.0		2.42167	128
R9	5.0	5.0		2.42167	128
R10	5.0	5.0		2.42167	128
R11	5.0	4.6875	0.3125	2.31439	112
R12	5.0	4.375	0.625	2.21186	112
R13	5.0	4.0625	0.9375	2.11387	112
R14	5.0	3.75	1.25	2.02022	96
R15	5.0	2.8125	2.1875	1.76345	96
R16	5.0	1.5625	3.4375	1.4711	80
R17	3.28	3.44	3.28	1.9314	96
R18	2.19	5.62	2.19	2.6495	128
R19	1.41	7.18	1.41	3.3219	176
R20	0.94	8.12	0.94	3.8071	192
R21	0.47	9.06	0.47	4.3629	224
R22	0.31	9.38	0.31	4.5702	240
R23		10.0		5.0	256
R24		10.0		5.0	256
R25	10.0			1.17287	64
R26	10.0			1.17287	64
R27	10.0			1.17287	64
R28	10.0			1.17287	64
R29	10.0			1.17287	64
R30	10.0			1.17287	64
R31	10.0			1.17287	64
R32	10.0			1.17287	64

Table A8 Light intensity modelling for input to the optical system for a 10 cm diameter horizontal pipe when the depth of the water is 5 cm.

Receiver	d_w (path length in water)	d_a (path length in air)	d_w (path length in water)	voltage (V)	bit representation
R1	3.28	3.44	3.28	1.9314	96
R2	2.19	5.62	2.19	2.6495	128
R3	1.41	7.18	1.41	3.3219	176
R4	1.875	7.185	0.94	3.3243	176
R5	1.875	7.655	0.47	3.55883	176
R6	1.875	7.815	0.31	3.64236	192
R7	2.0	8.0		3.74139	192
R8	2.0	8.0		3.74139	192
R9	2.0	8.0		3.74139	192
R10	2.0	8.0		3.74139	192
R11	1.875	7.815	0.31	3.64236	192
R12	1.875	7.655	0.47	3.55883	176
R13	1.875	7.185	0.94	3.3243	176
R14	1.41	7.18	1.41	3.3219	176
R15	2.19	5.62	2.19	2.6495	128
R16	3.28	3.44	3.28	1.9314	96
R17	3.28	3.44	3.28	1.9314	96
R18	2.19	5.62	2.19	2.6495	128
R19	1.41	7.18	1.41	3.3219	176
R20	0.94	8.12	0.94	3.8071	192
R21	0.47	9.06	0.47	4.3629	224
R22	0.31	9.38	0.31	4.5702	240
R23		10.0		5.0	256
R24		10.0		5.0	256
R25		10.0		5.0	256
R26		10.0		5.0	256
R27	0.31	9.38	0.31	4.5702	240
R28	0.47	9.06	0.47	4.3629	224
R29	0.94	8.12	0.94	3.8071	192
R30	10.0			1.17287	64
R31	10.0			1.17287	64
R32	10.0			1.17287	64

Table A9 Light intensity modelling for input to the optical system for a 10 cm diameter horizontal pipe when the depth of the water is 2 cm.

Receiver	d_w (path length in water)	d_{al} (path length in aluminium)	d_a (path length in air)	voltage (V)	bit representation
R1	10.0			1.17287	64
R2	10.0			1.17287	64
R3	7.5	1.875	0.625		0
R4	6.25	2.5	1.25		0
R5	6.25	2.5	1.25		0
R6	6.25	1.875	1.875		0
R7	8.125		1.875	1.5393	80
R8	8.125		1.875	1.5393	80
R9	8.125		1.875	1.5393	80
R10	8.125		1.875	1.5393	80
R11	6.25	1.875	1.875		0
R12	6.25	2.5	1.25		0
R13	6.25	2.5	1.25		0
R14	7.5	1.875	0.625		0
R15	10.0			1.17287	64
R16	10.0			1.17287	64
R17	6.56		3.44	1.9314	96
R18	4.38		5.62	2.6495	128
R19	2.82		7.18	3.3219	176
R20	10.0			1.17287	64
R21	10.0			1.17287	64
R22	10.0			1.17287	64
R23	10.0			1.17287	64
R24	10.0			1.17287	64
R25	10.0			1.17287	64
R26	10.0			1.17287	64
R27	6.25	2x1.875			0
R28	5.0	2x2.5			0
R29	5.0	2x2.5			0
R30	6.25	2x1.875			0
R31	10.0			1.17287	64
R32	10.0			1.17287	64

Table A10 Light intensity modelling for input to the optical system for a 10 cm diameter horizontal pipe when the depth of the water is 8 cm and two 2.5 cm diameter of aluminium rods are placed inside the pipe.

Receiver	d_w (path length in water)	d_{al} (path length in aluminium)	d_a (path length in air)	voltage (V)	bit representation
R1	8.4375		1.5625	1.4711	80
R2	7.1875		2.8125	1.76345	96
R3	4.375	1.875	3.75		0
R4	3.4375	2.5	4.0625		0
R5	3.125	2.5	4.375		0
R6	3.4375	1.875	4.6875		0
R7	5.0		5.0	2.42167	128
R8	5.0		5.0	2.42167	128
R9	5.0		5.0	2.42167	128
R10	5.0		5.0	2.42167	128
R11	3.4375	1.875	4.6875		0
R12	3.125	2.5	4.375		0
R13	3.4375	2.5	4.0625		0
R14	4.375	1.875	3.75		0
R15	7.1875		2.8125	1.76345	96
R16	8.4375		1.5625	1.4711	80
R17	6.56		3.44	1.9314	96
R18	4.38		5.62	2.6495	128
R19	2.82		7.18	3.3219	176
R20	1.88		8.12	3.8071	192
R21	0.94		9.06	4.3629	224
R22	0.62		9.38	4.5702	240
R23			10.0	5.0	256
R24			10.0	5.0	256
R25	10.0			1.17287	64
R26	10.0			1.17287	64
R27	6.25	2x1.875			0
R28	5.0	2x2.5			0
R29	5.0	2x2.5			0
R30	6.25	2x1.875			0
R31	10.0			1.17287	64
R32	10.0			1.17287	64

Table A11 Light intensity modelling for input to the optical system for a 10 cm diameter horizontal pipe when the depth of the water is 5 cm and two 2.5 cm diameter of aluminium rods are placed inside the pipe.

Receiver	d_w (path length in water)	d_{al} (path length in aluminium)	d_a (path length in air)	voltage (V)	bit representation
R1	6.56		3.44	1.9314	96
R2	4.38		5.62	2.6495	128
R3	2.82		7.18	3.3219	176
R4	2.815		7.185	3.3244	176
R5	2.345		7.655	3.5588	176
R6	2.185		7.815	3.64236	192
R7	2.0		8.0	3.74139	192
R8	0.75	1.25	8.0		0
R9	0.75	1.25	8.0		0
R10	2.0		8.0	3.74139	192
R11	2.185		7.815	3.64236	192
R12	2.345		7.655	3.5588	176
R13	2.815		7.185	3.3244	176
R14	2.82		7.18	3.3219	176
R15	4.38		5.62	2.6495	128
R16	6.56		3.44	1.9314	96
R17	6.56		3.44	1.9314	96
R18	4.38		5.62	2.6495	128
R19	2.82		7.18	3.3219	176
R20	1.88		8.12	3.8071	192
R21	0.94		9.06	4.3629	224
R22	0.62		9.38	4.5702	240
R23			10.0	5.0	256
R24			10.0	5.0	256
R25			10.0	5.0	256
R26			10.0	5.0	256
R27	0.62		9.38	4.5702	240
R28	0.94		9.06	4.3629	224
R29	1.88		8.12	3.8071	192
R30	10.0				64
R31	8.75	1.25			0
R32	8.75	1.25			0

Table A12 Light intensity modelling for input to the optical system for a 10 cm diameter horizontal pipe when the depth of the water is 2 cm and a 1.25 cm diameter aluminium rod is placed inside the pipe.